

MODELING OF TOOL WEAR AND TOOL FRACTURE IN MICROMILLING

A Thesis

by

DOMINIC SHIOSAKI

Submitted to the Office of Graduate Studies of
Texas A&M University
in partial fulfillment of the requirements of the degree of

MASTER OF SCIENCE

December 2011

Major Subject: Mechanical Engineering

MODELING OF TOOL WEAR AND TOOL FRACTURE IN MICROMILLING

A Thesis

by

DOMINIC SHIOSAKI

Submitted to the Office of Graduate Studies of
Texas A&M University
In partial fulfillment of the requirements of the degree of

MASTER OF SCIENCE

Approved by:

Co-Chairs of Committee,	Wayne N.P. Hung
	Molly Gentleman
Committee Member,	Theofanis Strouboulis
Head of Department,	Dennis O'Neal

December 2011

Major Subject: Mechanical Engineering

ABSTRACT

Modeling of Tool Wear and Tool Fracture in Micromilling. (December 2011)

Dominic Shiosaki, B.S., University of California-San Diego

Co-Chairs of Advisory Committee, Dr. Wayne N.P. Hung
Dr. Molly Gentleman

Micromachining is the next generation of precision material removal at the micro scale level due to the increase in miniaturization of commercial products. The applications of this technology extend anywhere from electronics to micro scale medical implants. Micromilling has the potential to be the most cost effective and efficient material removal process due to ease of use and accessibility of the tools.

This research analyzes vibration of a high speed spindle and then studies micromilling of aluminum and titanium. Finite element analysis and tool modeling compliment experimental data. Cumulative tool wear based on Taylor model shows decreasing tool life with increasing feed rate and increasing cutting speed on aluminum. Inconsistent results are seen when micromilling titanium due to premature chipping of tool noses. A significant nose wear plastically deforms a micromilled subsurface and is verified with microstructure study and microhardness measurements.

TABLE OF CONTENTS

	Page
ABSTRACT	iii
LIST OF FIGURES	vi
LIST OF TABLES	ix
LIST OF SYMBOLS	x
1. INTRODUCTION	1
1.1. Research Objectives.....	2
1.2. Research Scope	2
2. LITERATURE REVIEW	3
2.1. Micro-milling.....	5
2.2. Titanium.....	6
2.3. Aluminum	9
2.4. Micro vs. Macro.....	9
2.5. Micro-milling Issues	14
2.6. Coolant.....	17
2.7. Micro-tool	20
2.8. Tool Modeling	23
3. EXPERIMENTS	25
3.1. Equipment.....	25
3.1.1. Tool and Materials	25
3.1.2. HAAS Office Milling Machine.....	27
3.1.3. GF AgieCharmilles Wire EDM.....	27
3.1.4. UNIST Micro-mist system	27
3.1.5. Olympus Optical Microscope.....	27
3.1.6. Leco LM-21 Micro-hardness tester	28
3.1.7. Scanning Electron Microscope (SEM).....	28
3.2. Experimental Process Outline.....	28
3.3. Set-up and Positioning.....	29
3.4. Experimental Procedure.....	35
3.4.1. Contact Angle.....	35

	Page
3.4.2. Milling and Tool Wear	36
3.4.3. Microstructure	40
3.4.4. Microhardness	43
3.4.5. Finite Element Analysis	44
4. RESULTS AND DISCUSSION	52
4.1. Contact Angle	52
4.2. Tool Runout	54
4.3. Milling and Tool Wear	59
4.4. Tool Modeling	63
4.5. Microstructure	72
4.6. Microhardness	73
4.7. Finite Element Analysis	75
5. CONCLUSIONS AND RECOMMENDATIONS	81
REFERENCES	82
APPENDIX A: PROPERTIES AND SPECIFICATIONS OF MATERIALS AND EQUIPMENT	85
APPENDIX B: MATLAB PROGRAMS	94
APPENDIX C: REPEATABILITY, TOOL WEAR, CONTACT ANGLE AND HARDNESS DATA	100
APPENDIX D: G-CODE CNC PROGRAM FOR MILLING EXPERIMENT	116
APPENDIX E: FEA VERIFICATION CALCULATIONS	119
APPENDIX F: TOOL MODEL DERIVATIONS	127
VITA	131

LIST OF FIGURES

	Page
Figure 1: Dimensional size for the micro-mechanical machining (Chae et al., 2005).....	1
Figure 2: Development of achievable machining accuracy (McKeown, 1987).....	6
Figure 3: Titanium serrated chip (Machado & Wallbank, 1990).....	7
Figure 4: Micro vs. macro shearing comparisons (Schueler et al., 2010).....	10
Figure 5: Chip formation thickness, 'hm' is minimum chip thickness (a. no chip, b. chip with ploughing, c. chip formed with shear) (Chae et al., 2005)	11
Figure 6: Aluminum alloy AlSi5, microstructure influence on cutting forces (Chae et al., 2005)	12
Figure 7: Percent tool wear at varying feeds (Filiz et al., 2010)	14
Figure 8: Size effect in specific shear energy at different feeds (Lai et al., 2008).....	16
Figure 9: Chip load and force relationship for Pearlite (Chae et al., 2005)	17
Figure 10: Experimental results of tool wear when under different coolant methods (Rahman et al., 2002).....	18
Figure 11: Contact angle measurement technique using micro-pipette (Chittipolu, 2009)	19
Figure 12: Stress- strain plot in flexure test on tungsten carbide(Chittupolu, 2009)	20
Figure 13: SEM image of the tungsten carbide tool from crash test showing ductile failure (Chittipulo, 2009).....	22
Figure 14: Cumulative wear model with transition from high to low speed and low to high speed (Hung & Zhong, 1996).....	24
Figure 15: Micro tool #1640400 dimensions and geometry, and all dimensions are in inches (M.A. Ford 1998)	25

	Page
Figure 16: Cutting process between endmill and workpiece	26
Figure 17: Coordinate frame, designed with respect to workpiece	30
Figure 18: Zeroing yaw or z-axis rotation using an L-square	31
Figure 19: X-Y Positioning method	32
Figure 20: Coolant nozzle angle setup- θ direction (front view)	34
Figure 21: Coolant nozzle angle setup- ϕ direction (top view)	34
Figure 22: Coolube 2300HD, 0.1 microliter droplet on CP titanium.....	36
Figure 23: Initial measurement of a new micro-endmill.....	37
Figure 24: Endmill cutting path (top view):.....	38
Figure 25: Tool setup under microscope.....	40
Figure 26: Wire EDM cut path, section dimensions approximately 2 x 10 x 10mm.....	41
Figure 27: Resin mold of cut sections of CP titanium,	42
Figure 28: Vickers micro-hardness test.....	44
Figure 29: 3D SolidWorks model of micro-endmill and wire-mesh	45
Figure 30: Bending/tangential forces on endmill during cutting	46
Figure 31: Force vectors imposed on the cutting edge, the arrows along the flank are the tangential cutting forces.....	47
Figure 32: Endmill cutting path and chip formation	48
Figure 33: Shear area for chip formation	50
Figure 34: Contact angle results for aluminum 6061-T6 using 0.1 microliter droplets	53
Figure 35: Average contact angle for coolant on CP titanium with 0.1 microliter droplet.....	53
Figure 36: HAAS OM2 micromachining system used for runout measurement	55

	Page
Figure 37: Keyence laser raw data from tool runout/displacement during machining at 6K RPM(19.15 m/min).....	56
Figure 38: Frequency spectrum of tool runout: (a) laser noise; (b) spindle at 6k; (c) machining at 6k.....	58
Figure 39: Flank wear identification and measurement	60
Figure 40: Nose wear identification and measurement	60
Figure 41: Tool life vs. work time in aluminum (CL:chip load, $\mu\text{m}/\text{flute}$).....	62
Figure 42: Nose and flank wear of machining on titanium at 79.80 m/min cutting speed.....	63
Figure 43: Tool wear on aluminum using end mill at 63.8 m/min cutting speed (CL: chip load, $\mu\text{m}/\text{flute}$)	65
Figure 44: Tool life on aluminum using end mill at 95.8 m/min cutting speed (CL: chip load, $\mu\text{m}/\text{flute}$)	65
Figure 45: Feedrate vs tool life on log log plot for both cutting tools	71
Figure 46. View of microstructure of machined sample	72
Figure 47: Grain deformation (twinning) near machined surface. Microstructure images of 0.3 (a), 0.75 (b), and 1.0 (c) micron chip loads on CP titanium. The top of the image is the cutting surface and the cutting was performed in a perpendicular direction to the image.	73
Figure 48: Microhardness below surface of machined titanium (CL: chip load, $\mu\text{m}/\text{flute}$).....	74
Figure 49: FEA von Misses results at failure criterion of 4.7 GPa flexure strength at tool diameter.....	76
Figure 50: FEA-tool tip chipping zone at 25k RPM (79.80 m/min) on titanium.....	77
Figure 51: Tool fracture FEA with fracture zone, tool at 25k RPM (79.8 m/min) on CP titanium.....	78
Figure 52: Tool fracture FEA with fracture zone, tool at 20k RPM (63.84 m/min) on aluminum 6061-T6	79

LIST OF TABLES

	Page
Table 1: Flexural stress, strain values from three-point bend test (Chittipolu, 2009).....	21
Table 2: Test parameters with constant 0.381mm axial depth and 0.558 mm radial depth for 1.016 mm diameter endmill.....	39
Table 3: Krolls reagent (Lutjering et al., 2000).....	43
Table 4: Process parameters for measuring tool runout (Chittipulo 2009).	54
Table 5: Process parameters for measuring tool deflection when machining (Chittipulo 2009).	54
Table 6: Estimated tool life based on linear wear	66
Table 7: Feedrate w.r.t RPM and chip load.....	67

LIST OF SYMBOLS

a_{DOC}	Axial depth of cut (mm)
CL	Chip load ($\mu\text{m}/\text{flute}$)
d	Depth of cut (mm)
d_1	Horizontal diameter of hardness test (mm)
d_2	Vertical diameter of hardness test (mm)
f	Feedrate (mm/min)
F_i	Micro-hardness indenter force (kg)
i,j	Discrete step
K	Constant in contact angle equation
k	Number of passes at different V_c
N	Angular speed (rpm)
p	Number of constant speed steps in facing operation
P	Projected diameter (mm)
Q	Total accumulative damage (microns)
R	Radius of the workpiece (mm)

r_{DOC}	Radial depth of cut (mm)
T_i	Tool life at cutting speed V_i (min)
V	Drop Volume (micro-liter)
V_c	Cutting speed at the circumference (m/min)
x	Fraction of tool life
ε_f	Flexure Strain
Θ	Contact Angle (degree)
σ_f	Flexure Stress (MPa)
δt_i	Machining time at cutting speed V_i (min)
Δt_i	Total turning/milling time at cutting speed V_c (min)

1. INTRODUCTION

As technology quickly continues to reduce in size based on consumer needs and technological advances, manufacturing techniques are focusing more and more on small scale developments. With this new desire to focus on small scale manufacturing, research must be done at the micro/nano-scale. Micromachining, which includes micro-scale turning, drilling, and milling, are material removal processes that remove chips of material, specifically with dimensions of 0.1 to 100 μm . Very precise equipment and instruments are needed to maintain the increased accuracy of miniaturized products. Figure 1 shows where micro-machining's size and accuracy lay with respect to other types of material removal techniques. Also, although copious amounts of research have been done for years on macro-machining, materials, and conditions, a lot of these known properties do not scale down to the micro scale, so new research must be performed.

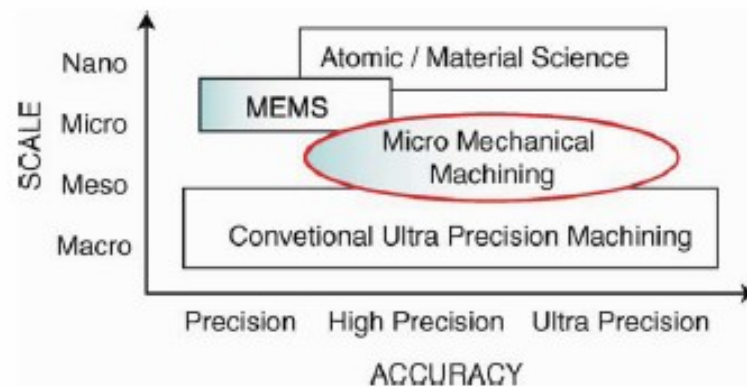


Figure 1: Dimensional size for the micro-mechanical machining (Chae et al., 2005)

This thesis follows the style of Machining Science and Technology

As the need for micro-machining increases, the need for its efficiency increases as well, this is a major driving force in increasing research. In 1996, Womack and Daniels published *Lean Thinking* which was a major influence on the manufacturing industry. The premise and major principle of this book is centered on the idea of preserving value with less work. By knowing how to perform micro-machining tasks properly, it will overall reduce time and error, which is due to the fact that fewer resources will go into trial and error of manufacturing (Womack & Jones, 1996). So by performing research in micro-milling, conditions and parameters can be established to predict tool life and failure which will thus give industry the ability to maximize their economic productivity.

1.1. Research Objectives

The main objectives of the research are:

1. Analysis of wear rates on micro tools
2. Predict micro-tool life and failure from observed tool wear rate
3. Apply FEA techniques to predict tool failure for different conditions of tool cutting forces.
4. Run out/tool vibration analysis

1.2. Research Scope

The scope of this research is limited to micro end-milling using a 2-flute tungsten carbide cutter on aluminum 6061-T6 and Commercially Pure (CP) Titanium. Micromist is used as cutting fluid in this study.

2. LITERATURE REVIEW

High-accuracy miniature components are quickly increasing in demand in many different industries such as aerospace, biomedical, electronics, environmental, communications and automotive. One of the driving forces behind the need for machining in all of these industries is the need and desire for more precise MEMS (micro-electro-mechanical systems) devices. Currently there are two types of manufacturing processes for MEMS devices, that is CMOS (Complementary metal-oxide-semiconductor) manufacturing and special processes, such as high-energy beam (HEB), lithography, electroplating, and molding (LIGA), electrical discharge machining (EDM) and micromachining. The most traditional process for larger batch processing is CMOS, it is very efficient but cannot perform at very high precision which is necessary as sizes reduce, and it is only specified for silicon material. The other special processes can deal with high aspect ratios but have their own limitations as well. Focused ion beam cutting which is in the HEB category, can reach high precisions but due to the excessive amounts of energy that the cutting requires, the heated machining surfaces can cause physical and chemical changes to the workpiece. If extremely high aspect ratios are needed, LIGA can make ratios at approximately 100:1 on scales of nanometers. This process involves preparing the material with a mask that will make the basic shape that is to be machining and also the final material has to be chemically treated to remove the mask as well. Although this may be efficient for a very specialized part, it takes many steps which can prove very time consuming to perform (Wang et al., 2007).

The other process for MEMS manufacturing is micro-cutting. This is traditional manufacturing which is being applied to micrometer and sub-micrometer levels for drilling, grinding, turning, and milling. The advantage to this type of technology is that it is suited for many different materials while maintaining high aspect ratios. Also setup of such technology is much less expensive and can be immediately used for batch process with computer numerical control (CNC) technology (Wang et al., 2007).

Micro-machining also poses general advantages in different aspects of manufacturing, such as environmental, economic, and technical (Okazaki et al., 2004).

Environmentally:

1. Saving energy and material resources: require minimum lubrication and no masking materials
2. Reduced vibration and noise for workers
3. Easier control of waste and pollution: removed material is contained in machine

Economically:

1. Reduced need for capital investment such as land space, buildings and power, and doesn't require clean room upkeep.
2. Reduced running costs: low power consumption, no need for high energy laser or x-ray technology
3. Efficient space utilization: small apparatus
4. Portability and reconfigurability: size of machines improve mobility

Technically:

1. Higher speeds and accelerations, reduce inertia due to tool size
2. Precision: micro- and nano-scale
3. Productivity: high allocations of machinery due to space consumption of machines
4. Piece by piece process advantage, likely hood of faults can be monitored and improved quickly without loss of batches since batches don't rely on single mold.

2.1. Micro-milling

Micro-mechanical machining is a fabrication method for creating devices and components with features that range from tens of micrometers to a few millimeters (Chae et al., 2005). Micro-milling is a quickly spreading process of material removal in the manufacturing industry. Micro-end milling has several advantages over other micro material removal processes such as ease of use, process flexibility, and low overall cost. This type of material removal is very desirable in fields for small functional components, such as medical devices (Thepsonthi & Ozel, 2010).

Micro-milling is commonly described by four parameters: axial depth, radial depth, chip load, and cutting speed. The axial depth of cut (*aDOC*) is the depth of the endmill into the workpiece in the vertical direction. The radial depth (*rDOC*) is the depth of the endmill into the workpiece in the direction parallel to the radius (*r*) of the micro-tool. The chip load (*CL*) is the proposed thickness of the chips that will be formed from each pass of a single cutting edge. Finally, the cutting speed (*V_c*) is the linear speed of the cutting tip at the circumference of the tool. Additionally, feedrates and RPM are needed for machine programming but these can be extracted from the four main parameters. The feedrate (*f_r*) is the linear speed of the center of the tool in the cutting direction and the RPM is the rotations per minute of the endmill. Equivalently,

$$V_c = 2 * \pi * r * RPM \quad (1)$$

$$f_r = \#of\ teeth * RPM * CL \quad (2)$$

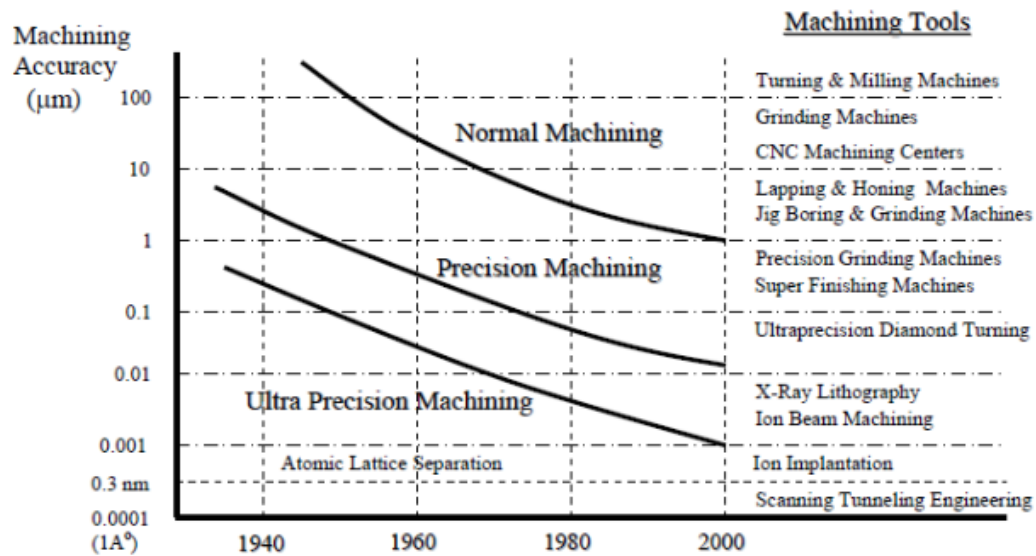


Figure 2: Development of achievable machining accuracy (McKeown, 1987)

As shown in Figure 2, the achievable machining accuracy for normal machining is currently reaching the micron level. With more research being performed and with techniques improving, these curves will continue to progress downwards.

2.2. Titanium

Titanium is a metal showing a high strength to weight ratio which is maintained at elevated temperatures (up to 800°C) and it has excellent corrosion resistance. The major applications of this material are in the aerospace industry due to these qualities and also increasingly in medical devices because of titanium's unique quality of bio-compatibility (Machado & Wallbank, 1990).

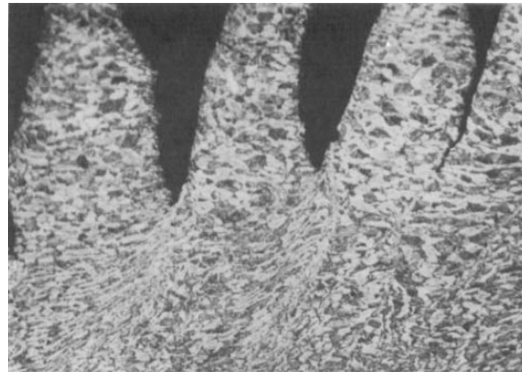


Figure 3: Titanium serrated chip (Machado & Wallbank, 1990)

Although these properties make titanium very desirable to work with, they also complicate the machining process. One trait that makes it difficult to mill is its poor thermal properties. When chips form during titanium machining they usually occur as serrated chips as opposed to continuous. Figure 3 shows an image of a serrated chip of titanium after machining. This serration is explained due to the fact that the rate of decrease in strength resulting from the local increase in temperature equals or exceeds the rate of increase in strength due to strain hardening in the primary shear zone. As the chips are forming, excessive heat is built up and the material is deformed but the heat does not move to a new plane so cooler material is plastically deformed around the cut and sheared, causing a saw-tooth chip. This is known as ‘catastrophic thermoplastic shear’ or adiabatic shear (Machado & Wallbank, 1990).

The low thermal conductivity of titanium also influences the tool wear. At these localized zones of high heat due to the thermoplastic shear, the material is softened. Now with a low Young’s modulus and high shear strength, in addition to thermal properties explained previously, work hardening is achieved if a minimum chip thickness isn’t met

because the tool will plastically deform and harden the titanium when a chip isn't formed. The minimum chip thickness is a requirement based on the size effect which states that the depth of cut and the chip load must be greater than the tool tip radius in order to form a chip. Then when milling, the tool must mill over the hardened metal. This then leads to high flank wear in the tool (Schueler et al., 2010).

Another property important to titanium milling at the micro level is its crystallographic structure, as discussed earlier. Titanium is an allotropic element, which means that it has more than one crystallographic form in different conditions. At room temperature titanium has a hexagonal close-packed crystal structure also known as 'alpha phase'. Then at 883°C the structure transforms to a body centered cubic crystal structure called 'beta phase'. This may be important if cutting parameters cause an excess of heat in the material and if cutting is performed without coolants (Chae et al., 2005).

Titanium was chosen as a material to focus on because of its bio-compatibility and its applicability to the medical industry. It is also very popular in aerospace and other industries where weight is a factor. Titanium, in an unalloyed state, is nearly as strong as some steels but about 45% lighter, so it has a very high strength to weight ratio. Although a very desirable material to use, titanium is classified as a hard to machine material due to its increased hardness (approx. 220 on Vickers scale) and poor thermal properties (Boyer et al., 1994).

2.3. Aluminum

Aluminum has advantageous properties as a metal such as low density (light weight) and corrosion resistance. When the exposed surface of aluminum combines with oxygen it forms an oxide film only a few ten-millions of an inch thick which reduces corrosion and reactions with some substances. It is also the most widely used non-ferrous metal and is used in products in the aerospace industry to the automotive industry because of its high strength density and favorable machinability.

Aluminum 6061-T6 is an alloy and is also known as aircraft grade. Aluminum has a density of about $2700 \frac{kg}{m^3}$ compared to that of steel at $7850 \frac{kg}{m^3}$ (Hatch, 1984). The 6061-T6 alloy contains 0.8-1.2% magnesium and 0.4-0.8% silicon. (Davis, 1993).

Aluminum is also a very desirable material to use conventional machining techniques, such as milling or turning. It is a relatively soft metal with a Vickers hardness number of approximately 100. In addition, low shear strength makes it a very easy material to machine (Holt et al., 1999).

2.4. Micro vs. Macro

Research has already been performed for macro-sized milling and standards for machining various materials have already been created. Research in micro-milling is slowly growing as well, but there are few properties that can transition proportionally from macro- to micro-size milling and machining. Some of these disproportional properties are force predictions, tool/workpiece interaction, and cutting parameters.

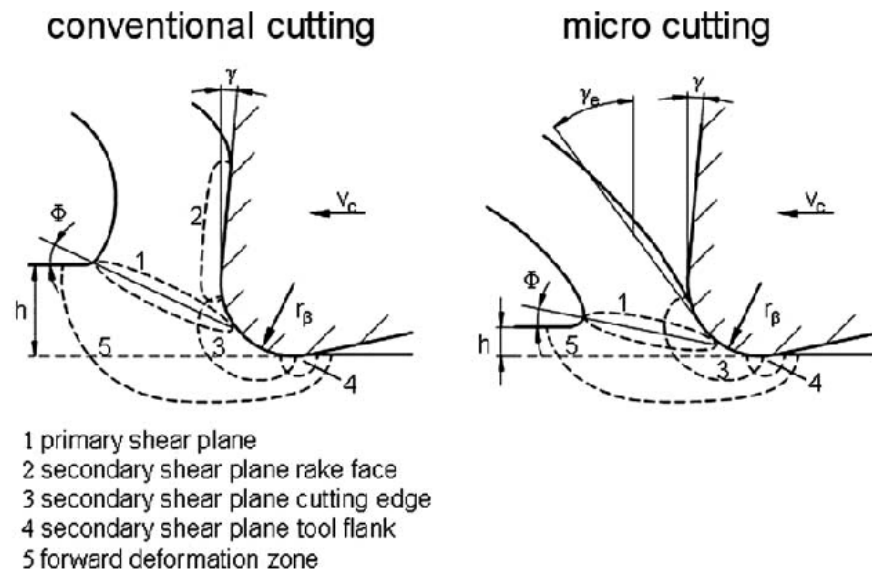


Figure 4: Micro vs. macro shearing comparisons (Schueler et al., 2010)

Macro and micro cutting imply different forces on the cutting edges. Figure 4 shows the two shear zones for macro- and micro- cutting. This results in more of the force being implied on the flank edge of the tool in micro-cutting because (i) the secondary shear plane, as shown in the conventional cutting diagram, is significantly reduced in micro-cutting, and (ii) the reduced shear angle that increases the shear zone (Schueler et al., 2010).

Tool/workpiece interactions have to do with the size of the tool edge relative to the thickness of the chips that are being removed; this is called the *size effect*. In macro milling the tool sizes are multiple times larger than the chip thicknesses, but in micro-milling the chips are on the same scale as the edge radius. The problem that arises with the same size scales is high localized forces on the micro cutting edge and work hardening potential due to not being able to form a chip (Schueler et al., 2010).

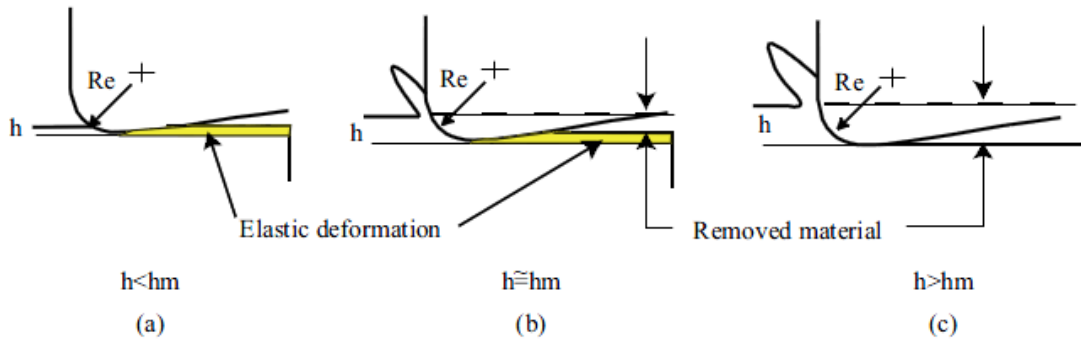


Figure 5: Chip formation thickness, ‘ h_m ’ is minimum chip thickness (a. no chip, b. chip with ploughing, c. chip formed with shear) (Chae et al., 2005)

In micromachining, chips may not form if the tool does not cut deeper than a minimum chip thickness. Figure 5 shows the concept of size effect. In the figure, (a) shows the condition where the depth of cut is much smaller than the minimum chip thickness so all of the material is elastically deformed. Image (b) shows where the minimum chip thickness is the same as the depth of cut where some material is cut and some is elastically deformed and in part (c), a proper chip is formed because the depth of cut is larger than the minimum chip thickness. If this is the case (a or b) then the resulting cutting forces may result in ‘ploughing’ of the material as opposed to shearing. Ploughing may result in plastic deformation of the zone, along with higher friction temperatures, and vibrations in the cutting process (Chae et al., 2005).

Also, in micromachining, due to the size of the chips being created, the crystallographic structure should be considered when dealing with certain alloys. As shown in Figure 6, the aluminum alloy consists of a soft phase and brittle phase. In

macro-milling the structure is assumed homogeneous and involves removing many grains or different crystal orientation from the material. Micromilling involves removing single grains of specific orientation from the material.

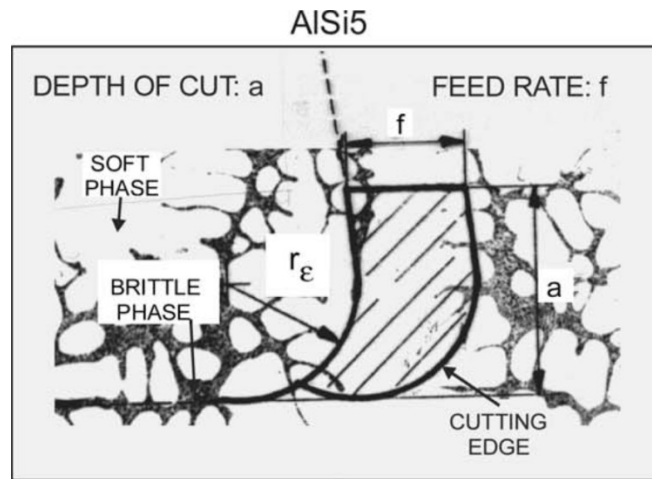


Figure 6: Aluminum alloy AlSi5, microstructure influence on cutting forces (Chae et al., 2005)

Tool run out and unbalance is also another difference in micro and macro machining. Tool run out is caused by misalignment of the axis of symmetry between the tool and the tool holder. In macro-size machining it doesn't actively cause a problem because runout error on a micron scale will be well below design tolerance. When it comes to micromachining, runout of a few tens of micrometers can be on the same order as the diameter of the tool, so it is very crucial to the outcome. Also, if the micro tool is off balance, small vibrations are exaggerated due to the size of the tool and the high RPMs that micro machining usually requires (Chae et al., 2005).

Force sensing methods are an additional difference between micro and macro-size machining. Much higher precision sensing methods must be employed because the forces on the workpiece are much less than in macro scale machining due to the size of the chips being created. Also, detecting errors and damages to the tool are usually very difficult due to its scale. It usually requires some additional instrumentation such as an optical microscope or scanning electron microscope. Then if error is made to the workpiece, the tolerances are usually very precise and it is hard to adjust for such error (Chae et al., 2005).

Another unexpected difference between micro and macro tool properties is the wear rates. In macro-scale machining, tool wear increases with increasing speed and feedrates. This is expected because the cutting tool needs more energy to produce bigger chips. But in contrast, micro tools' tool wear was seen to decrease with increasing feedrates, and slower speeds may lead to higher tool wear. This was proposed to be due to bluntness of the tool and that ploughing dominated material removal. At low feeds the blunt cutting is when tool is rubbing against the material but cannot generate chips at every pass (Filiz et al., 2010).

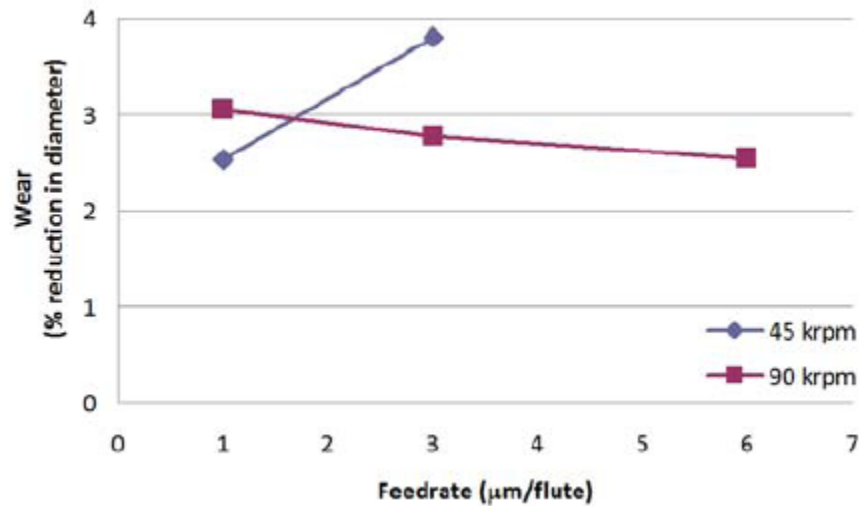


Figure 7: Percent tool wear at varying feeds (Filiz et al., 2010)

Figure 7 shows data results from micro milling experiments on titanium. Filiz performed multiple experiments that resulted in higher speeds decreasing the wear rates in his 0.4 mm diameter tungsten carbide micro tools. The result is, however, statistically indifferent (Filiz et al., 2010).

2.5. Micro-milling Issues

There are still other issues that obtrude the standardization of the micro-milling process. One of these issues is the cost of developing requirements. One of the requirements is a general minimum chip thickness for a wide variety of materials. This requires experimental models and is expensive because the normalized minimum chip thickness is determined by each material's thermo-mechanical properties and the dimensional properties of the cutting tool.

Also, heat also needs to be considered. When attempting to model cutting conditions in micro milling, heat originates from mechanical energy involved in the basic shear of the material, which is standard for milling. In addition to this in micro-milling, heat from the friction of the chip moving over the tool rake face is important. Finally, heat that may arise from ploughing or rubbing in the metal due to material removal is a large factor and can greatly influence the final totals (Liu et al., 2004).

In experimentation from Liu, DeVor and Kapoor, minimum chip thickness was found to vary based on the cutting conditions as well as the materials. The normalized minimum chip thickness was found to increase as the cutting velocity and tool edge radius increased when machining carbon steel. This was explained as thermal softening dominated the strain hardening. But when aluminum was experimented, the minimum chip thickness was found to stay near constant over different cutting speeds and edge radii. This was because the thermal softening and strain hardening were equally influential (Liu et al., 2004).

Another issue in determining and predicting tool reactions in micro tools is the nonlinear relation in cutting force and chip loads due to the size effect. During experimentation it was found that there was a nonlinear increase in the specific energy or cutting forces as the uncut chip thickness was decreased.

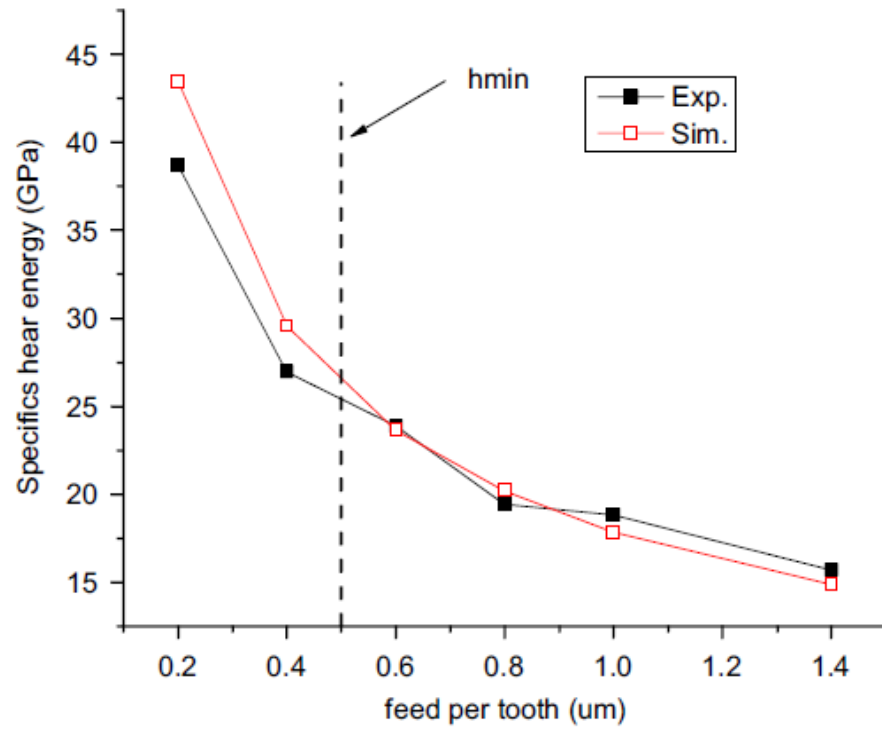


Figure 8: Size effect in specific shear energy at different feeds (Lai et al., 2008)

The cause of this nonlinearity was the decrease in the tool chip interface temperatures. This correlates with the effects of work hardening in hard materials and micro-machining, which due to ploughing of small chips cutting required more force/energy on the hardened material. After a minimum chip thickness and chip loads were met, the forces vs. feed became much more linear, as seen in Figure 8 (Lai et al., 2008).

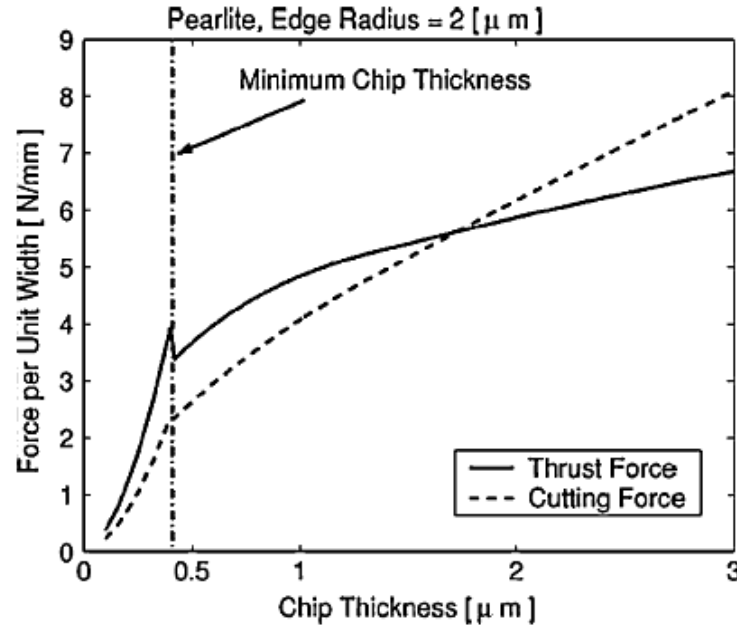


Figure 9: Chip load and force relationship for Pearlite (Chae et al., 2005)

Other anomalies in micro-milling include sudden increases in force while crossing over the minimum chip thickness. During experiment, Liu encountered sudden increase in thrust forces, while machining pearlite, which was explained by the shift from plowing to the dominant shearing forces. Figure 9 shows this data and the minimum chip thickness is seen as the location of the spike in the graph where the increased amount of milling force occurs.

2.6. Coolant

The effects of coolants have been shown to increase the life of the tool and also positively affect the workpiece. Minimum quantity lubrication (MQL) is a newer technique that involves the use of a mist spray where coolant is atomized out of a nozzle

and sprayed onto a cutting tool during machining. The research of this began from economics and environmental aspects. By using MQL as opposed to flood cooling, much less is spent on coolants. Also, the use of large quantities of coolants can pose as a health risk to those that are in contact with the fluids.

The effectiveness of MQL has also been tested to show the validity of these techniques. Figure 10 shows images of two different parameters when under dry, flood, and MQL cutting conditions. The figure shows that the MQL reduces wear efficiently compared to dry cutting and flood cooling (Rahman et al., 2002).

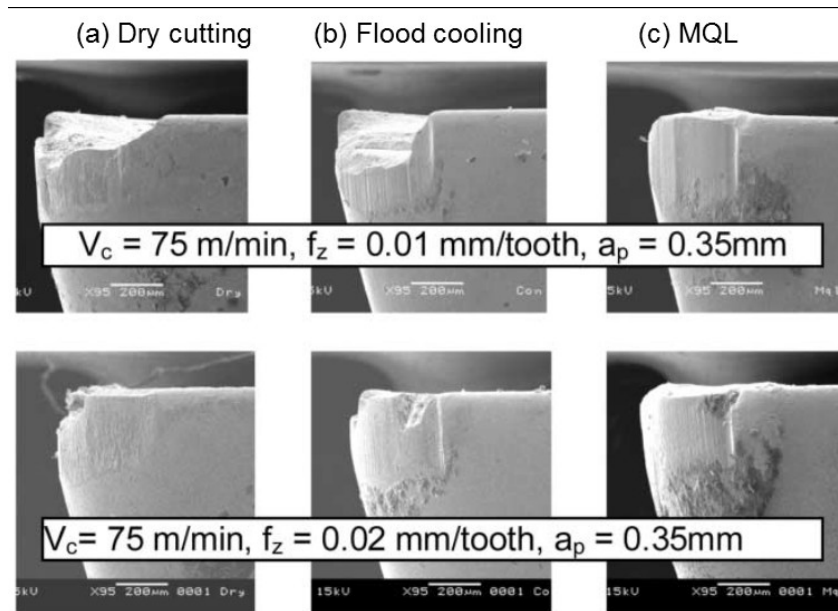


Figure 10: Experimental results of tool wear when under different coolant methods (Rahman et al., 2002)

To optimize MQL, a coolant should be used that most efficiently ‘wets’ the work material being used. The most effective fluid will result in a minimum contact angle with the workpiece material, since this allows maximum area for effective heat transfer. The measurement of contact angle is important in a quantitative comparison between different cutting fluids. If a goniometer is not available to measure contact angle, an alternate technique can be used. Contact angle can be derived from diameter of a drop of the coolant on to the work material when knowing the volume of the liquid drop (Chittipolu, 2009). Figure 11 shows the profile of a drop of coolant and its contact angle.

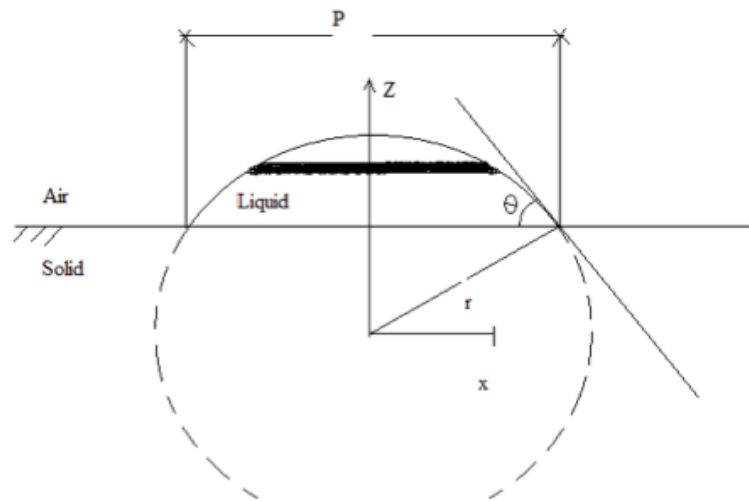


Figure 11: Contact angle measurement technique using micro-pipette (Chittopolu, 2009)

$$\frac{P}{V^{1/3}} = \left[\frac{24}{\pi} \frac{(1-K \cos^2 \theta)^{\frac{1}{2}}}{2-3 \cos \theta + \cos^3 \theta} \right]^{1/3} \quad (3)$$

Equation (3) represents the relations of the droplets diameter P , and volume V , to the contact angle θ . The constant K equals 1 for contact angles greater than 90° and 0 for less than 90° .

2.7. Micro-tool

Tungsten carbide micro-endmills with a 1.016 mm diameter were used in this study. Experimental data has been taken to determine the stress-strain curve of the same micro-tools. Figure 12 and Table 1 shows typical stress strain relationship of this material under 3-point bending test (Chittupolu, 2009).

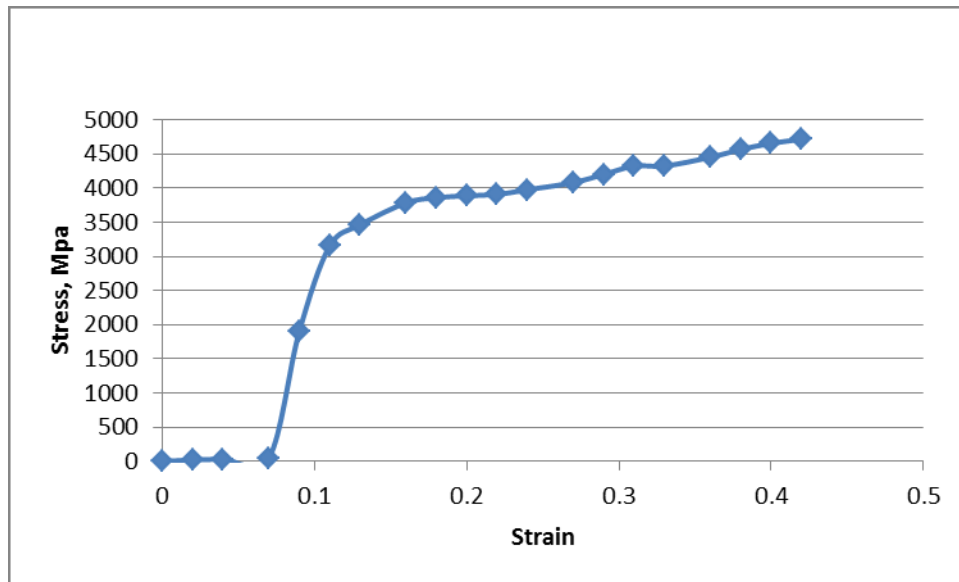


Figure 12: Stress- strain plot in flexure test on tungsten carbide(Chittupolu, 2009)

Table 1: Flexural stress, strain values from three-point bend test (Chittipolu, 2009)

No.	Flexure Stress, σ_f MPa	Flexure Strain, ε_f
1	0	0
2	19.92	0.02
3	30.25	0.04
4	43.11	0.07
5	1896.62	0.09
6	3153.31	0.11
7	3463.31	0.13
8	3783.8	0.16
9	3860.05	0.18
10	3889.06	0.2
11	3908.62	0.22
12	3977.45	0.24
13	4082.7	0.27
14	4202.13	0.29
15	4325.6	0.31
16	4325.6	0.33
17	4453.79	0.36
18	4567.82	0.38
19	4656.88	0.4
20	4716.93	0.42

The data shows that the material obeys Hooke's law for stress between 500 MPa and 3000 MPa, where the strain of the material is linearly proportional to the stress. At increased stress the material will begin to plastically deform and eventually fracture. The collected data shows the flexure strength of the material was found to be 4.7 GPa and have a Young's Modulus of 92.7 GPa. Figure 13 shows an SEM picture of the ductile failure that the micro-tool at flexure strength. (Chittipulo, 2009).

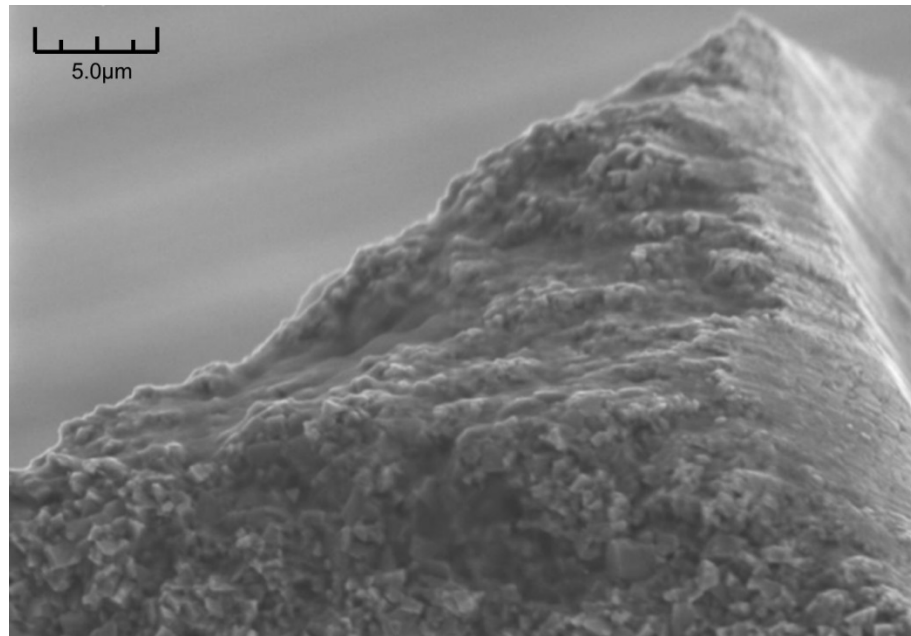


Figure 13: SEM image of the tungsten carbide tool from crash test showing ductile failure (Chittipulo, 2009)

Finite element analysis performed on the tool with comparable inputs from high chip load tests (where fracture was forced) and showed that the tool was at fracture conditions when over flexure strength levels. This would be at approximately 667 N of bending force at the tip of the tool. Other failure criterion for this 1.016 mm diameter micro-end mill include: 1) 50µm of flank wear; 2) 50µm of nose wear; 3) chipping or breaking of cutting edge; whichever happens earlier. Since there is no standard for tool failure these criteria were set based on the tool wear rates rapidly increasing when beyond these values, which would quickly lead to catastrophic failure (Chittipulo, 2009).

2.8. Tool Modeling

Classical Taylor equation relates tool life, cutting speed, feedrate, and depth of cut in the study of machinability. These parameters help to determine the theoretical life of a tool under specific conditions. Research has suggested that it is also possible to use multiple iterations of this equation in summation of different parameters for a single tool. So if a tool is used at an initial setting and then altered, an accurate life can still be predicted by taking the initial settings into account. Starting with Taylor's equation, Hung and Zhong (1996) suggest that cumulative wear models can be created to predict tool life progressively as the tool is used, even if under varying parameters. Equations (4) and (5) represent the cumulative tool wear models.

$$T_c = \sum_{j=1}^k \Delta t_j \quad (4)$$

$$V_c^{1/n} = \frac{\sum_{j=1}^k \Delta t_j V_{cj}^{1/n}}{Q \sum_{j=1}^k \Delta t_j} \quad (5)$$

where T_c and V_c represent the cumulative tool life and the equivalent cutting speeds, respectively. The constant k is the number of machining experiments done using the tool, Δt_j is the time at each experiment, Q is the cumulative wear on the tool, n is the constant based on tool wear rate, and V_{cj} is the cutting speed of the tool at each experiment.

The model also showed that the order in which test were performed was negligible. High speeds could be used first with rapid wear then switched to low speeds or low speeds first with lower wear rates, the models still held consistent and accurate in determining the tool wear (Hung & Zhong, 1996). Figure 14 shows data plots of the cumulative wear model.

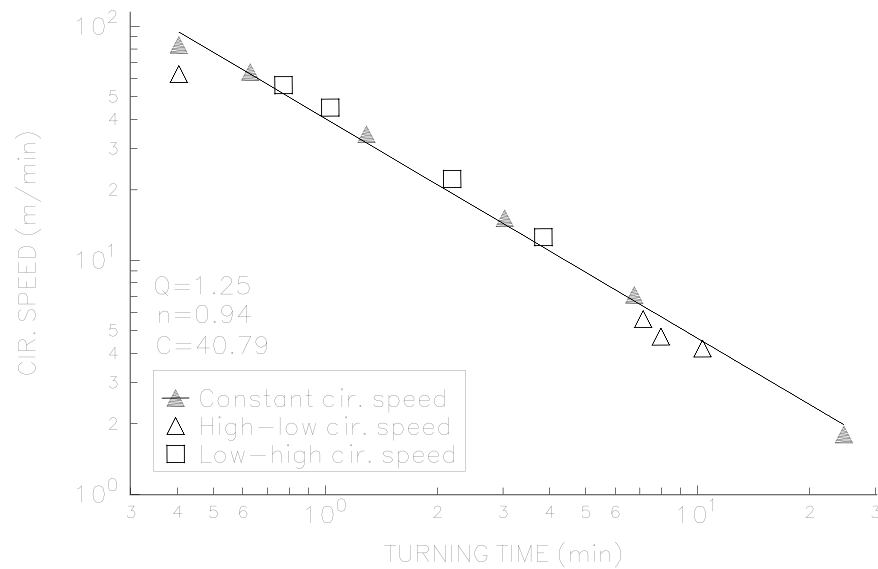


Figure 14: Cumulative wear model with transition from high to low speed and low to high speed (Hung & Zhong, 1996)

3. EXPERIMENTS

The scope of the research, as stated earlier, was to identify tool wear on a tungsten carbide end-mill while milling aluminum and titanium using micro-mist as a cutting fluid.

3.1. Equipment

3.1.1. Tool and Materials

The experiments were all performed with same cutting tools. The micro-end mill used was a 1.016 mm micro endmill provided by M.A. Ford. The tool was a Tuff Cut 2-flute endmill made of uncoated sintered tungsten carbide in cobalt binder. The tool shank diameter was 3.175 mm for the precision micro-milling machine. Figure 15 shows the design of this tool. (See Appendix A.4 for tool specifications)

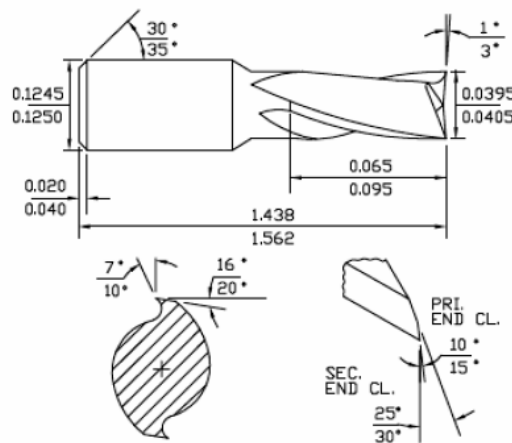


Figure 15: Micro tool #1640400 dimensions and geometry, and all dimensions are in inches (M.A. Ford 1998)

Both aluminum alloy 6061-T6 and commercially pure (CP) titanium were used. In the experiments, aluminum was cut into sections of rectangular cross-sections with dimensions of 20 mm width by 12.7 mm thickness. The CP titanium used in the experiments was 10 mm by 10 mm square cross section and cut into test sections of approximately 100 mm. The material was prepared by hand grinding down the work surface with 600 grit abrasive paper (16 micron particle diameter). This was to have a flat and smooth surface while removing any potential impurities. Figure 16 shows the cutting process between the endmill and the workpiece. (See Appendix A.5 and A.6 for material specifications).

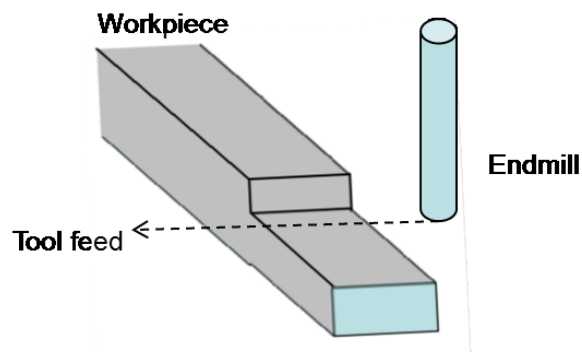


Figure 16: Cutting process between endmill and workpiece

3.1.2. HAAS Office Milling Machine

The HAAS OM2 office milling machine was used in the research to perform the milling test. This machine was chosen due to its high accuracy, both of positioning and its repeatability, and its high spindle speed of up to 50,000 RPM. The OM2 has positioning accuracy of ± 0.005 mm and repeatability of ± 0.003 mm. (HAAS 2010). (See Appendix A.1 for machine specifications)

3.1.3. GF AgieCharmilles Wire EDM

The wire EDM (electrical discharge machining) by GF AgieCharmilles was used to section a milled sample in order to study micro-structure of the subsurface; the EDM is a non-contact machining technique and was used to prevent further microstructure damage. (See Appendix A.7 for machine specifications)

3.1.4. UNIST Micro-mist system

A UNIST Micro Mist system was attached to the OM2 to provide MQL mist to the tool and workpiece. (See Appendix A.3 for system specifications) Different lubricants were tested and Coolube 2210 was chosen for both aluminum and titanium due to its wetting properties.

3.1.5. Olympus Optical Microscope

An Olympus STM6 Optical Microscope was used to measure the tool wear. The microscope also had an attached Olympus DP70 12.5 MP Camera so that all the data could be recorded and post-processed if needed. The microscope had four objective

lenses that ranged from 1.25X to 50X, and an attached digital readout for measurement resolution of 0.0001 mm in the X, Y, and Z directions.

3.1.6. Leco LM-21 Micro-hardness tester

The Leco LM-21 tester was used for hardness testing on the CP titanium samples. The indenter used diamond tipped pyramidal points at 136 degrees. The indenting is used for Vickers hardness testing. The tip used in the micro hardness produced an average diagonal size of 25 micrometers. The amount of force and dwell time was 0.1 N and 13 seconds, respectively.

3.1.7. Scanning Electron Microscope (SEM)

The JEOL6400 scanning electron microscope was used in tool wear investigation in addition to the measurement optical microscope for higher resolution and magnification.

3.2. Experimental Process Outline

The following tasks were outlined to achieve the research objectives of this thesis:

1. Measure coolant contact angles in order to choose the most appropriate cutting fluids that would maximize tool life. The contact angles were measured by choosing various available fluids and examining droplet sizes on a flat sample of intended material. The coolant with the lowest contact angle, which represented the maximum surface area contact, was chosen.

2. Perform vibration analysis to determine potential sources of error in the experiments. Frequency analysis of the vibration data was used to identify possible electronic noise, spindle runout, and machine inaccuracies.
3. Perform micromilling and measure tool wear on micro-tool from milling time on specified metals. The tool's set-up procedure was developed in order to maintain consistency between tests of different parameters and conditions. Programmed G-codes were developed to ensure that consistent paths and machine parameters were used throughout different tests. Since the same 1.016 mm diameter tungsten carbide end-mill was used for all tests, the set up procedures and machine parameter could be held constant in the HAAS OM2. Periodic tool wear was measured using the optical microscope.
4. Mathematical models were made to predict tool lives under various cutting conditions. The models were based upon cumulative tool wear model theory.
5. Finite element models were created using SolidWorks to predict failure and breakage in micro-tools. The model validity was verified using manual calculations and experimental data. Forces were calculated for shearing force imposed on the tool during cutting. Material properties were incorporated into the computer models to ensure accurate representation of tool stress and deflection concentrations.

3.3. Set-up and Positioning

In order to maintain consistent results in the micro-end milling experiments, standard set-up procedures were developed. The set-up procedure was designed

carefully due to the size effects as mentioned above. Since the size of a cutting tool and the machining parameters were similar, tool misalignment could cause a great deal of error. The parameters that were standardized were the orientation of cutting fluid needle and the tool/workpiece origin. In the experiment, the back left corner of the workpiece was set as the programming origin as referenced in Figure 17.

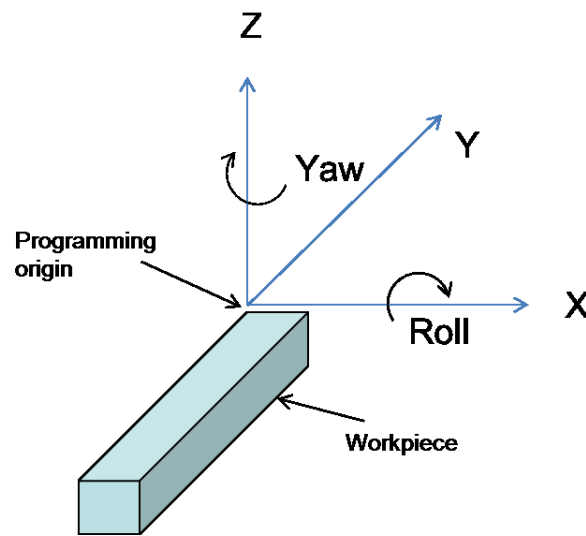


Figure 17: Coordinate frame, designed with respect to workpiece

Initially, rotation about the Z-axis (yaw) needed to be initialized or zeroed. This direction is referenced in Figure 17 and refers to the rotation of the plane that the workpiece was attached to. In order to zero this rotation, two procedures needed to be performed. First, the whole plane in question was rotated 90 degrees (rolling or rotation about the X-axis) so that it sat parallel to the plane of the endmill axis. Then the

workpiece was rotated until it was also 90 degrees from the machine, this was performed by using a square as shown in Figure 18. After this measurement was performed the rotation was set to 0 degrees as an offset and was correctly referenced to the CNC code. Then the rotations of the work plane were reset to 0 (level).

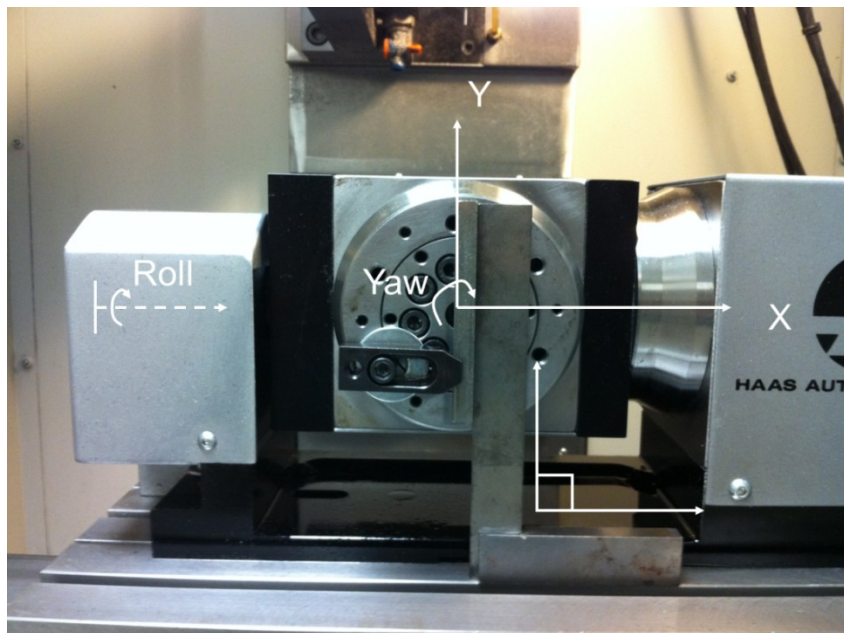


Figure 18: Zeroing yaw or z-axis rotation using an L-square

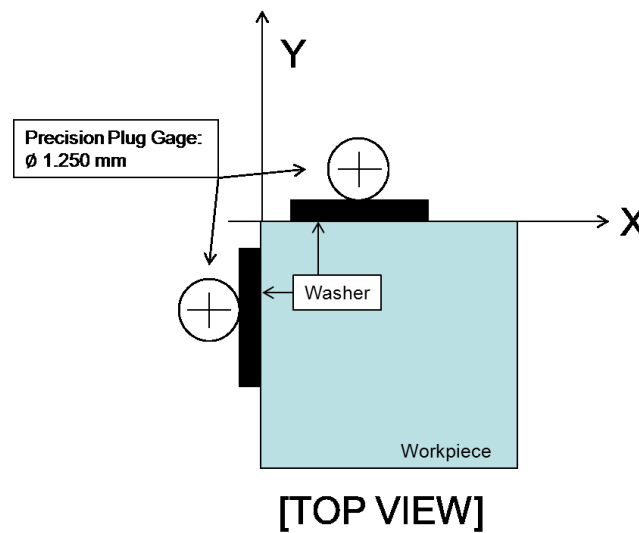


Figure 19: X-Y Positioning method

To zero the piece in the x- and y-direction, a precision plug gage (1.250 mm) was inserted into the machine collet. Use of the plug gage instead of a fragile cutting tool prevented possible damage to the tool during tool setup. The plug gage was translated in the x-direction until it came into contact with a rubber washer (also used for tool safety to prevent physical contact with an inelastic material). This washer's thickness was measured with a precision micrometer. At this point the location of the material in the x-direction was referenced by offsetting for the thickness of the washer and the radius of the rod. The offset was entered into the OM2 CNC. Secondly, the procedure could be repeated in the y-direction to find the y- offset and programming origin. A diagram for this testing method is shown in Figure 19. Repeatability tests were performed to make sure that this was a consistent method of zeroing the tool in the x- and y-direction, which resulted in a 0.0005 mm standard deviation in repeated tests. (See Appendix C)

Finally, the z direction was zeroed. This was the only direction that required the actual cutting tool. The plug gage was replaced with an actual tool with the same shank diameter. Again to ensure precision, it was placed with 19.0 mm protrusion from the collet and was estimated using a digital caliper from the end of the collet to the tip of the endmill. Once the tool was secured, it was then positioned above the workpiece and lowered until touching the rubber washer, similar to the XY axis zeroing. Once contact was made, the location was then offset for the thickness of the washer.

Repeatability of this setup technique was performed. The precision rod was positioned against the rubber washer multiple times and each time the rod touched the washer, the locations was recorded. By recording the location of the rod multiple times, the repeatability of this method would be observed. After 10 iterations of this test, it was concluded that this method could achieve approximately 0.0005 mm repeatability.

Setting the coolant needle completed the setup. Previous research for optimization of coolant spray direction was used to avoid coolant scatter and maximize surface contact/wetting. The coolant needle position was fixed relative to the tool tip. The coordinates were $(r, \theta, \Phi) = (30 \text{ mm}, 60^\circ, 55^\circ)$, where 'r' is the radial distance from the tool tip; ' Φ ' is the angle between the y-axis on the machine coordinate system and the mist nozzle direction, and ' θ ' is the angle between the tool axis and the mist nozzle direction. Figure 20 and Figure 21 shows these angles imposed on the tooling.

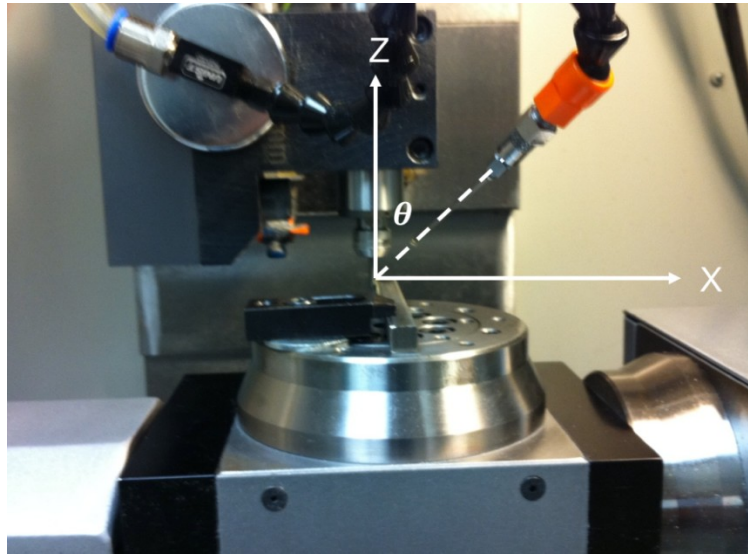


Figure 20: Coolant nozzle angle setup- θ direction (front view)

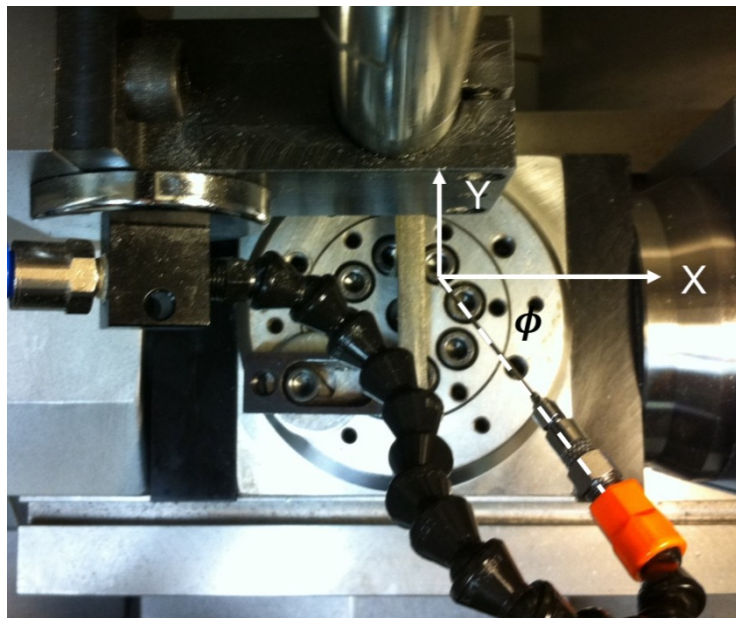


Figure 21: Coolant nozzle angle setup- ϕ direction (top view)

3.4. Experimental Procedure

3.4.1. Contact Angle

The contact angle of the droplet on the work material was calculated by using a micro-pipette and a sample of the material that was worked on. In experimentation, the surface preparation was done by initially grinding the work material surface down with 600 grit abrasive paper and then polishing with 0.5 micron Al_2O_3 powder.

If the surface was not properly prepared, incorrect measurement could result. Before and after polishing the samples must remain clean otherwise impurities may get onto the surface and scratch the sample during polishing. Any bumps, indents, or scratches would create more surface area for the coolant to wet thus alter the measured diameter.

Once the surface was prepared, droplets of coolant were measured on the material surface. This was done by taking samples of a coolant using a micropipette that was accurate to .01 microliters then placing the drops on the work material. The diameters of these droplets were then measured on the measurement microscope. An example of a droplet is shown in Figure 22 shows a tested droplet from experiment.

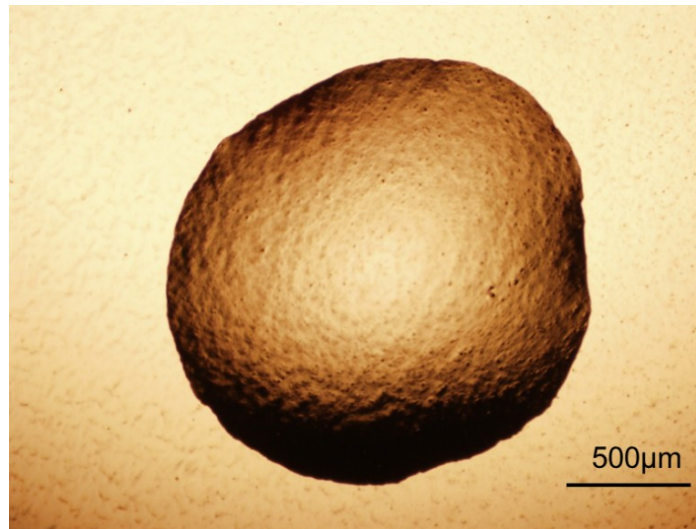


Figure 22: Coolube 2300HD, 0.1 microliter droplet on CP titanium

After a series of droplets were dimensioned and measured, the average diameters of the droplets were taken to reference an accurate contact angle for the chosen cutting fluid.

3.4.2. Milling and Tool Wear

One of the main objectives for this research was to model tool wear. The procedure of this testing was controlled for consistent results:

1. Choose tool and perform initial observation using the Olympus microscope
2. Set up tool and work material in standard procedure (Section 3.3)
3. Perform test procedure by running the CNC program on the HAAS OM2 milling system
4. Remove tool (not workpiece) periodically and measure tool wear and observe any indication of tool fracture

5. Replace tool and continue testing (steps 2-4) until failure condition was met or wear trends were observed.

The first step of the testing required the tool to be chosen and observed. The tool was initially measured, whether it was new or used, because a baseline needed to be established to observe the change that the machining had caused. This was done by placing the micro-end mill under the measurement microscope and measuring initial wear or tool defects. As seen in Figure 23, this new micro-endmill was observed and the initial flank was measured. Once the tool data was logged the second step of tool set-up was performed. (See Section 3.3.)

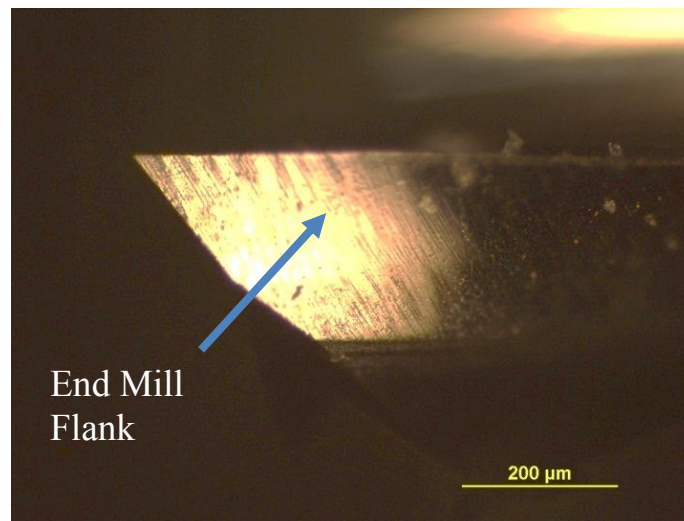


Figure 23: Initial measurement of a new micro-endmill

Micromilling was performed after the tool/workpiece set-up, zeroing was performed, and the spray nozzle was positioned. A tool was cutting in down-milling

mode with spindle speed, chip loads, and feedrates as variables while axial and radial depth of cut were kept constant at 0.381 mm and 0.558 mm, respectively. The program code is documented in Appendix D. Figure 24 shows the tool path. An endmill started at the top left corner (origin) of the work materials. From the starting point (above the material) the endmill reached the desired speed and then slowly lowered in the z (axial)-direction to the desired cutting depth. It then moved in the X direction, as indicated by the solid line, to pass the workpiece width to complete one pass. The tool then lifted up vertically in the Z direction and prepositioned to prepare for the second pass (dotted line). Then the process was repeated at the specific axial and radial cutting depths until the program was completed. The amount of passes varied based on the amount of material desired to be cut. After completion, the tool returned to origin and stopped.

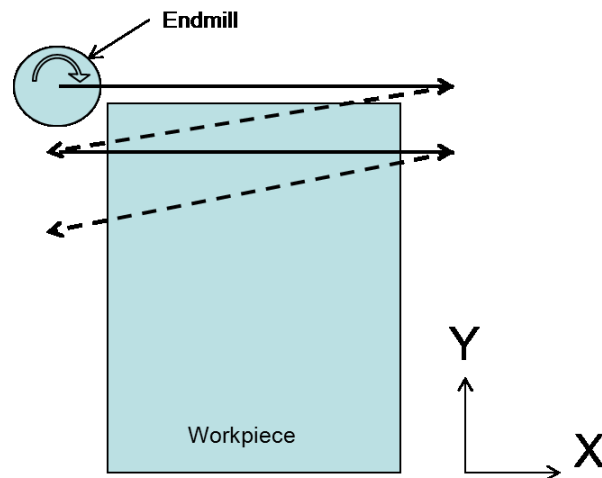


Figure 24: Endmill cutting path (top view):

Solid arrow for cutting, dotted arrow for movement above workpiece.

The test parameters for the experiments are shown in Table 2. As shown, there were two different sets of parameters for each metal, this was chosen due to the increased hardness of titanium and the desire to avoid breaking the tool prematurely.

Table 2: Test parameters with constant 0.381mm axial depth and 0.558 mm radial depth for 1.016 mm diameter endmill

material	RPM	Cutting Speed (m/min)	feedrate (mm/min)	Chip load (μm/flute)
Aluminum 6061-T6	20000	63.8	20.0	0.5
	20000	63.8	40.0	1.0
	30000	95.8	30.0	0.5
	30000	95.8	60.0	1.0
Titanium CP	25000	79.8	15.0	0.3
	25000	79.8	37.5	0.8
	25000	79.8	50.0	1.0
	25000	79.8	62.5	1.3

Once an iteration of an experimental condition was performed, the tool was removed from the collet for wear assessment. The number of passes per iteration was based on the material available to cut; the more important factor was recording the milling time and measuring wear after each iteration. After milling, the wear on the tool was observed and recorded. The tool was positioned under the microscope so that the cutting blade of the micro-endmill was perpendicular to the front of the microscope and the flank was parallel to the microscope's surface.

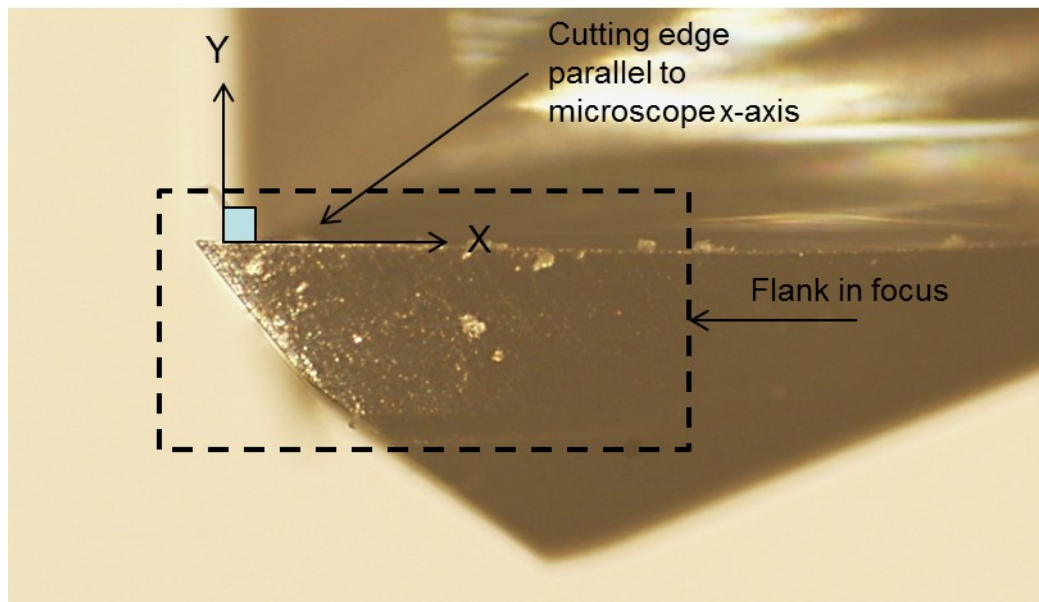


Figure 25: Tool setup under microscope.

Figure 25 shows the tool setup under the optical microscope. This setup was desired because the microscope measures in x, y, and z directions so by isolating the flank wear to be measured in the y axis, measurements were able to be performed by moving only one axis.

3.4.3. Microstructure

After milling and tool wear experiments were performed, an assessment of microstructure damage under machined surface was necessary. The process of preparing the sample and observing the microstructure had multiple steps:

1. Cut out a sample section of the work material
2. Mold into a hard resin mount
3. Grind and polish

4. Chemical etching
5. Observe under microscope
6. Measure microhardness

The first step in examining the microstructure was to cut out a section of the machined sample using wire type electrical discharge machine (wire EDM). The wire EDM was used to cut a path perpendicular to the path of the milling direction as seen in Figure 26.

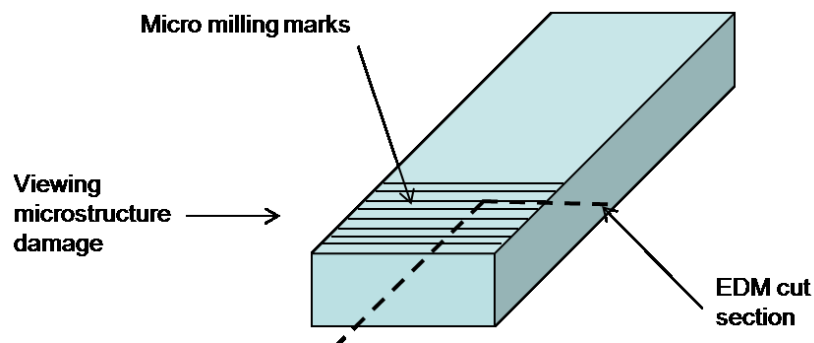
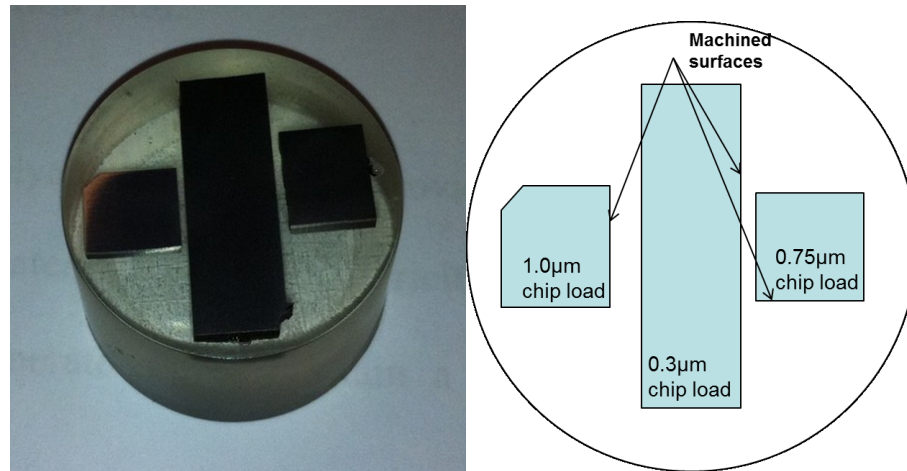


Figure 26: Wire EDM cut path, section dimensions approximately 2 x 10 x 10mm

The second step was to take cut sections and mount in slowly cured epoxy. The sections were placed at the bottom of a mold and the resin/hardener and the mixture was slowly poured into the mold on top of the piece(s). Resin/hardener was composed of 15 parts of Epofix embedding resin and 2 parts Epofix hardener. The rate of the pour remained very slow in order to reduce the occurrences of bubbles in any part of the mold. A void would not only weaken the structure of the mold, but also collect

contaminants that may scratch the polished surface. As shown in Figure 27, three different pieces were molded into the resin for microstructure observation. Three samples of CP titanium were positioned so that they were not touching.



**Figure 27: Resin mold of cut sections of CP titanium,
dimensions for sections from left to right: 9.72 x 10mm, 9.72 x 30 mm, 9.72 x 10mm**

Upon full cure of the epoxy resin, the mold was initially ground for parallelism on top and bottom surfaces. A micrometer was used to measure the mold thickness away from the titanium samples. Parallelism of the mold was necessary for microscope observations later. The mold was ground on varying grits of grinding papers. The sample was first smoothed with 200 grit paper, the 400 and then 600 grit paper. Finally the metal side of the mold was polished down to 0.5 micron with alumina polishing compound.

After polishing, the next step was chemical etching to reveal the microstructure. For Ti, Kroll's reagent was used as the chemical etchant. The chemical composition for Krolls is shown in Table 3.

Table 3: Krolls reagent (Lutjering et al., 2000)

Krolls Reagent	Chemical	Amount
	Distilled Water	92 ml
	HNO ₃	6 ml
	HF	2 ml
Etch time	15-30 sec	

The etchant time was varied based on desired contrast. The recommended range was from 15 seconds to 30 seconds, with longer times resulting in more contrast but potential oversaturation in detail. The etching time was selected to be 20 seconds.

3.4.4. Microhardness

Microhardness testing was performed on polished machined titanium samples. The Leco LM-21 micro-hardness tester was used. In the test, a Vickers micro-indenter with a 136° pyramidal tip was indented into the material with a force of 0.1 N with a dwell time of 13s to form a square impression into the material. Then the diagonals of the square were measured using the optical microscope and averaged. Figure 28 shows how the indentation was made and how the diagonals were measured. Microhardness was calculated by using equation (6).

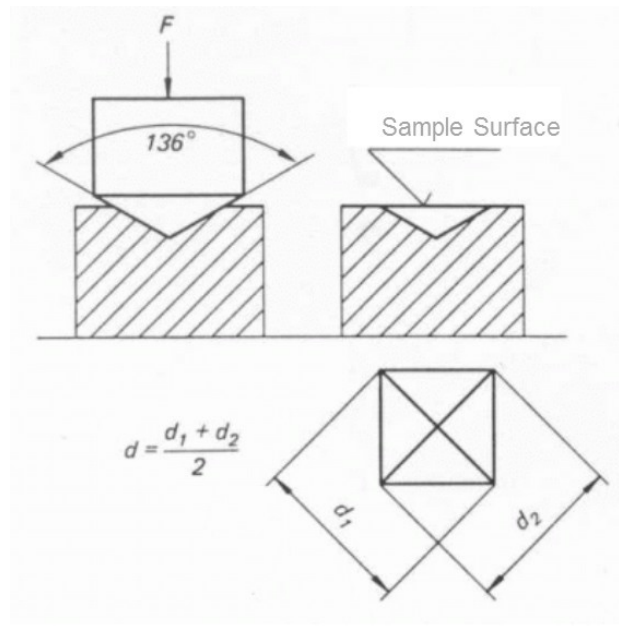


Figure 28: Vickers micro-hardness test

$$\text{Hardness} = \frac{1.8544 * F_i}{d^2} \quad (6)$$

3.4.5. Finite Element Analysis

Finite element analysis (FEA) was used to predict catastrophic tool failure. The general procedure for FEA was as follows:

1. Create 3D model
2. Assign material and properties
3. Create constraints on model
4. Impose forces on model

A 3D model endmill was made in SolidWorks. A rendering of the endmill can be seen in Figure 29.

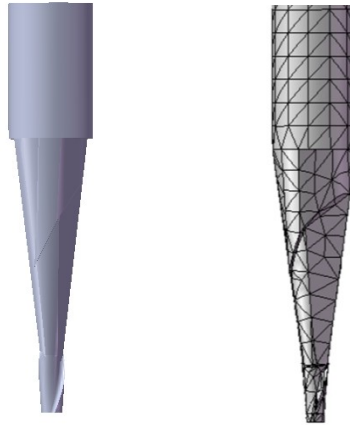


Figure 29: 3D SolidWorks model of micro-endmill and wire-mesh

Once a 3D model was created, the material and some additional properties needed to be assigned. The material used in experimentation was tungsten carbide with Young's modulus of 92.7 GPa and flexure strength of 4.7 GPa. These properties assumed that the model was linear elastic and that it would fracture at the flexure strength (Chittipulo, 2009).

The next step was to set boundary conditions. The tool was constrained in all 6 degrees of freedom at the tool shank, which was at 19.0 mm from the tip of the tool. The forces that were imposed were equivalent to the cutting force so the tool itself was fixed.

Finally, the forces that the tool experienced during cutting were applied. They were applied at the flank and tip of the tool, taking into account the axial and radial depths of cut of the cutting parameters of 0.381 mm and 0.558 mm, respectively. There were two force components that caused bending and torsion of an endmill during cutting. Bending was caused by a force imposed on the tool due to the movement in the feed direction. Torsion was caused by the tangential force due to rotational motion of the cutting tool. (See Figure 30)

Within the FEA, some assumptions were made. The material was assumed to be linear elastic and no plastic deformation would occur on the tool; therefore, failure was due to limitation on flexure strength.

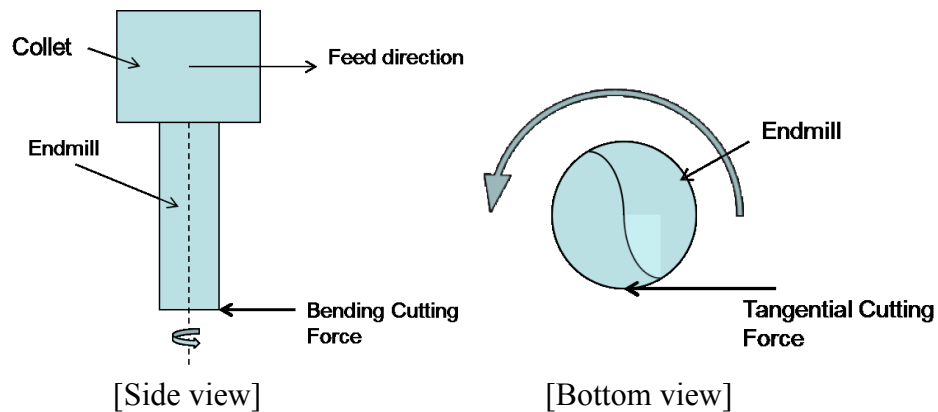


Figure 30: Bending/tangential forces on endmill during cutting

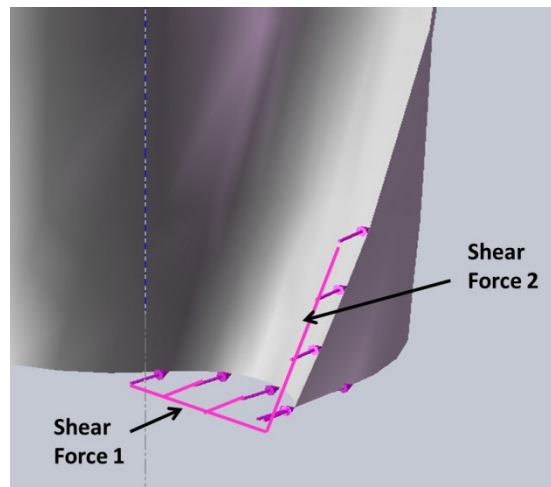


Figure 31: Force vectors imposed on the cutting edge, the arrows along the flank are the tangential cutting forces

Figure 31 shows the force vectors that were modeled on the endmill in the torsion and bending directions. The vectors along the flank were at the axial cutting depth and the vectors along the bottom of the micro-endmill were at the radial depth of cut. The forces that resulted from equations (10) through (14) were imposed at these locations.

Motion equations of the endmill's 2D movement in the cutting direction were created to determine the amount of shear area that was occurring during specific cutting conditions. The equations were based on the parameters of chip load, spindle speed, radial/axial depth of cut, and titanium's material properties.

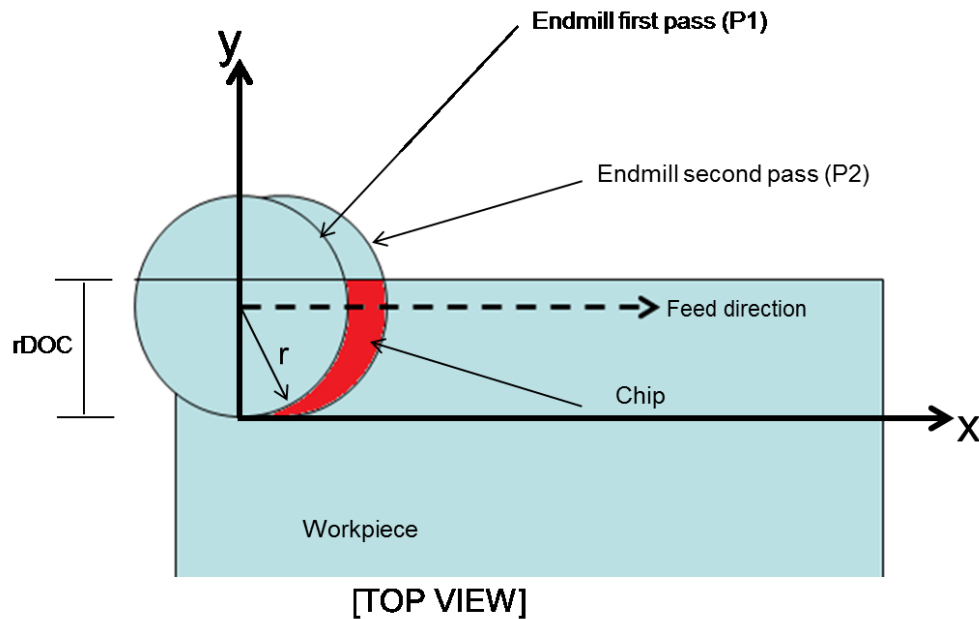


Figure 32: Endmill cutting path and chip formation

To calculate the approximate shear area of the chip, the endmilling tool was simplified as a circle. Figure 32 shows two positions of the tool and geometry of a chip. The coordinate system used in calculations uses the same directions for X and Y as the machine, but the origin is as the bottom of the cutting tool of P1 to simplify calculations. Equations (7) and (8) are circle equations at positions P1 and P2. The second circle (P2) tool has been shifted by the chip load to represent the movement in the cutting direction. Both equations have also been shifted in the positive y direction by the radius so the circles are in the first quadrant. The other variables, r , $rDoc$, CL , and y , respectively represent the tool radius, radial depth of cut, chip load, and the y-axis direction.

$$x_{p1} = \sqrt{r^2 - (y - r)^2} \quad (7)$$

$$x_{p2} = \sqrt{r^2 - (y - r)^2} + CL \quad (8)$$

To find the chip zone or shear area the finite strip area of the chip is identified as the area between the two circles as:

$$Shear\ Area = \int_0^{rDoc} (x_{p2} - x_{p1}) dy \quad (9)$$

Finally, the shear area was multiplied by the shear strength of titanium to determine the amount of force that it would take to shear the chip.

$$Shear\ Force1 = Ti_Shear_Strength * Shear\ Area \quad (10)$$

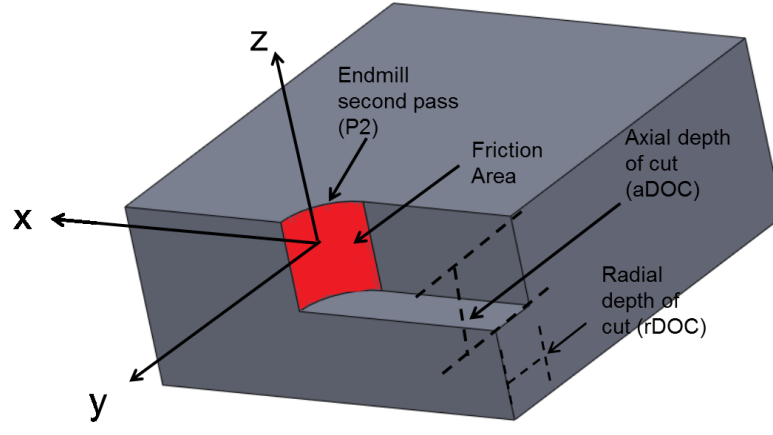


Figure 33: Shear area for chip formation

A similar process was performed to calculate the friction area of the chip, which is depicted in Figure 33. The friction area was calculated by multiplying the length of the curve P2, by the axial depth of cut. The general formula for arc length of a curve, given the equation of the curve is $f(x) = g$, where a and b are the boundaries,

$$\text{Arc length of curve} = \int_a^b \sqrt{1 + \left(\frac{d}{dx} f(x)\right)^2} dx \quad (11)$$

The arc length of P2 was multiplied by the axial depth of cut to get the area.

$$\text{Friction Area} = \left(\int_0^{rDOC} \sqrt{1 + \left(\frac{d}{dy} x_{P2}\right)^2} dy \right) * aDOC \quad (12)$$

$$Friction\ Area = \left(\int_0^{rDoc} \sqrt{1 + \left(\frac{d}{dy} \sqrt{r^2 - (y - r)^2 + CL} \right)^2} dy \right) * aDOC \quad (13)$$

Matlab was used in order to calculate the integral (See Appendix B). Finally, the area was again multiplied by the shear strength of titanium to determine the shear force.

$$Shear\ Force2 = Ti_Shear_Strength * Friction\ Area \quad (14)$$

The result of these forces were applied to the model and the tool then processed through FEA. Also, these equations were applied to the shear force required to mill aluminum. To calculate the forces for aluminum the shear strength for titanium was replaced with that of aluminum. (The Matlab code for these calculations is in Appendix B)

4. RESULTS AND DISCUSSION

4.1. Contact Angle

The contact angle measurement technique used for comparing contact angles between various different types of fluids gave consistent results for the same fluids, hence making it a reliable method of comparison (Figure 34). The cutting fluid contact angle test resulted in the Coolube 2210 being the more appropriate cutting fluid to use on the aluminum and titanium. The Coolube type coolants were more efficient overall but the 2210 consistently resulted in having the minimum contact angle of approximately 2 degrees on the aluminum and titanium. The Koolmist coolants were water based coolants and had much higher contact angles than the other coolants. (Tabulated results and statistical data in Appendix C)

The same experiment was performed with CP titanium. Some of the coolants varied on their contact angle but the Coolube 2210 still showed the minimum contact angle, so it was used as the cutting fluid for both materials. Figure 35 shows the results.

The surface cleanliness and roughness were carefully controlled in the experiment to maintain consistent results. The samples were rinsed with water in between steps of grinding and polishing and at the end, and they were kept in a dry box when not in use. If there were any impurities on the surface such as bumps, indents, or scratches, this would alter the surface area of the material and thus alter the measured diameters of the droplets.

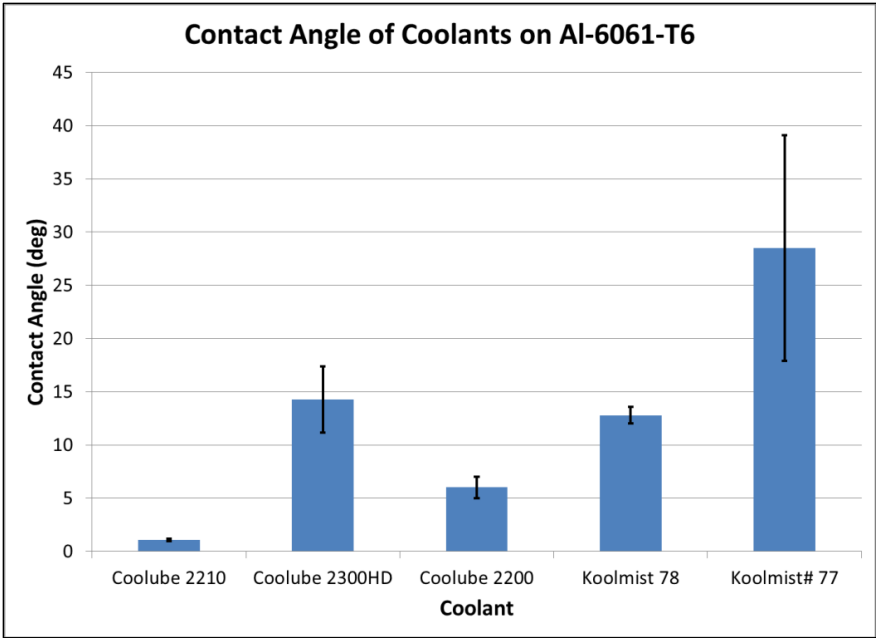


Figure 34: Contact angle results for aluminum 6061-T6 using 0.1 microliter droplets

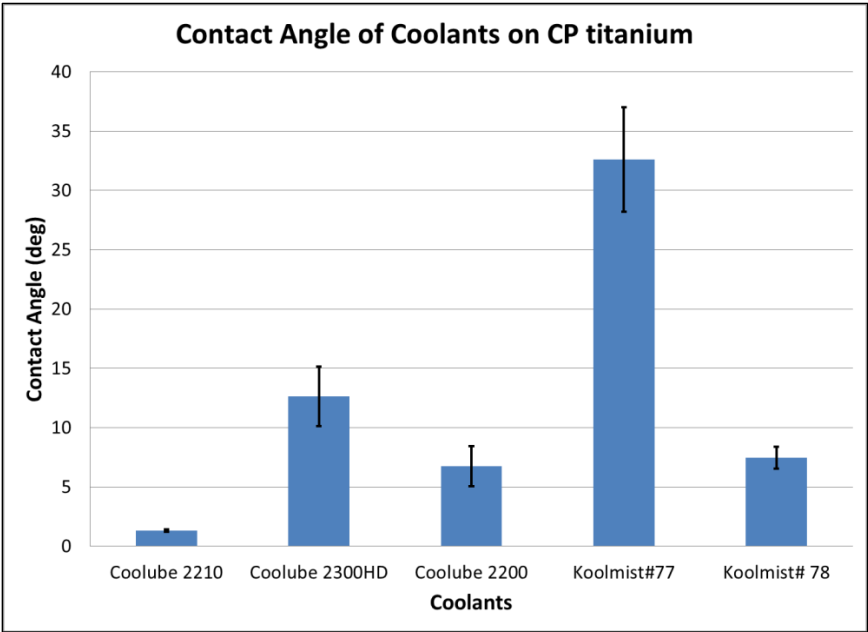


Figure 35: Average contact angle for coolant on CP titanium with 0.1 microliter droplet

4.2. Tool Runout

Tool runout was analyzed from previous data taken via a Keyence LK-G157 displacement laser system. Table 4 and Table 5 show the test setup that was used.

Table 4: Process parameters for measuring tool runout (Chittipulo 2009).

Micro-cutting tool	Gauge pin, dia: 3.175mm
Workpiece material	316L Stainless steel
Spindle speed	0 rpm(stationary), 6k rpm(19.15 m/min), 10k rpm (31.92 m/min)

Table 5: Process parameters for measuring tool deflection when machining (Chittipulo 2009).

Micro-cutting tool	Dia: 1.016mm, 2 flute
Workpiece material	316L Stainless Steel
Feed per tooth/ Chip load	10 micron/tooth
Axial depth of cut	0.35 mm
Radial depth of cut	0.56 mm
Spindle speed	6 k(19.15 m/min), 15k(47.88 m/min) and 25k rpm (79.80 m/min)
Coolant	UNIST mist spray

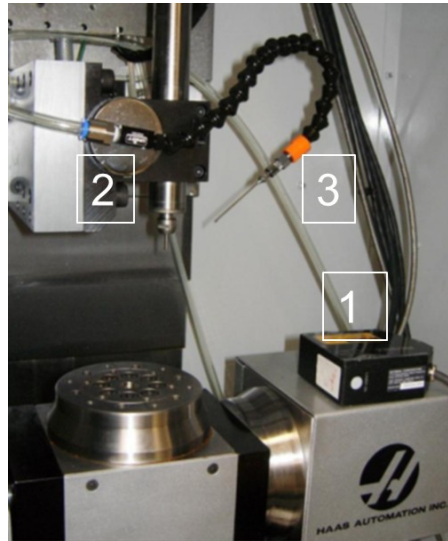


Figure 36: HAAS OM2 micromachining system used for runout measurement

1: Keyence laser, 2: Spindle of OM2 and 3: Mist coolant hose (Chittipulo, 2009).

This experiment was performed on a block of 316L stainless steel. End milling was performed on the HAAS OM2 micromachining system using MA Ford's carbide end mill tools ($\text{Ø}1.016 \text{ mm}$, 2 flute) in mist coolant. The tool was machined for a straight line cut with a constant axial and radial depth of cut. All tools were ultrasonically cleaned in alcohol before any machining and measurement. The mist coolant was applied at 135° relative to the feed direction and at a distance range of 25-30 mm from the tool through the coolant hose 76.2 mm of UNIST mist system. Coolube 2210EP coolant was used for the mist spray.

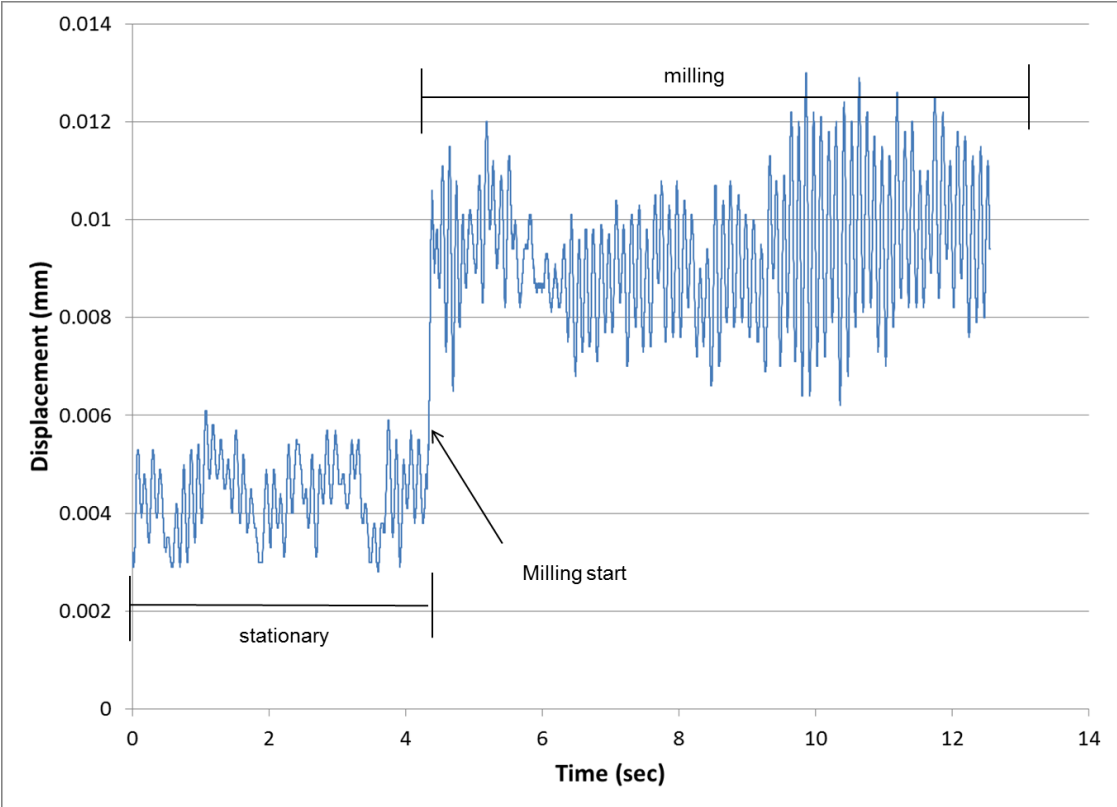


Figure 37: Keyence laser raw data from tool runout/displacement during machining at 6K RPM(19.15 m/min)

The Keyence displacement laser recorded deflections of the tool in different conditions. The tool was held stationary for a base reading, it was also powered at different rpm settings for tool runout readings, and it was used for machining to recorded runout while under machining conditions. Figure 37 shows the displacement data before and after micromilling. In this test, the spindle was held at 6K RPM (19.15 m/min) then it was used for milling. The difference locations of displacement between the stationary and milling zones shows the displacement of the tool during machining. Also, the difference in the oscillatory amplitudes between machining and stationary shows the effect of tool vibration. The sources of runout from these plots alone are difficult to analyze without further manipulation. Fast Fourier analysis was performed then placed in a power spectrum graph. This allowed the data to show where vibration peaks occurred with respect to different frequencies. By then splitting up the data from the original graphs to include data sets of nonrotating spindle, rotating spindle, and milling conditions, the graphs showed specifically what was causing the tool runout.

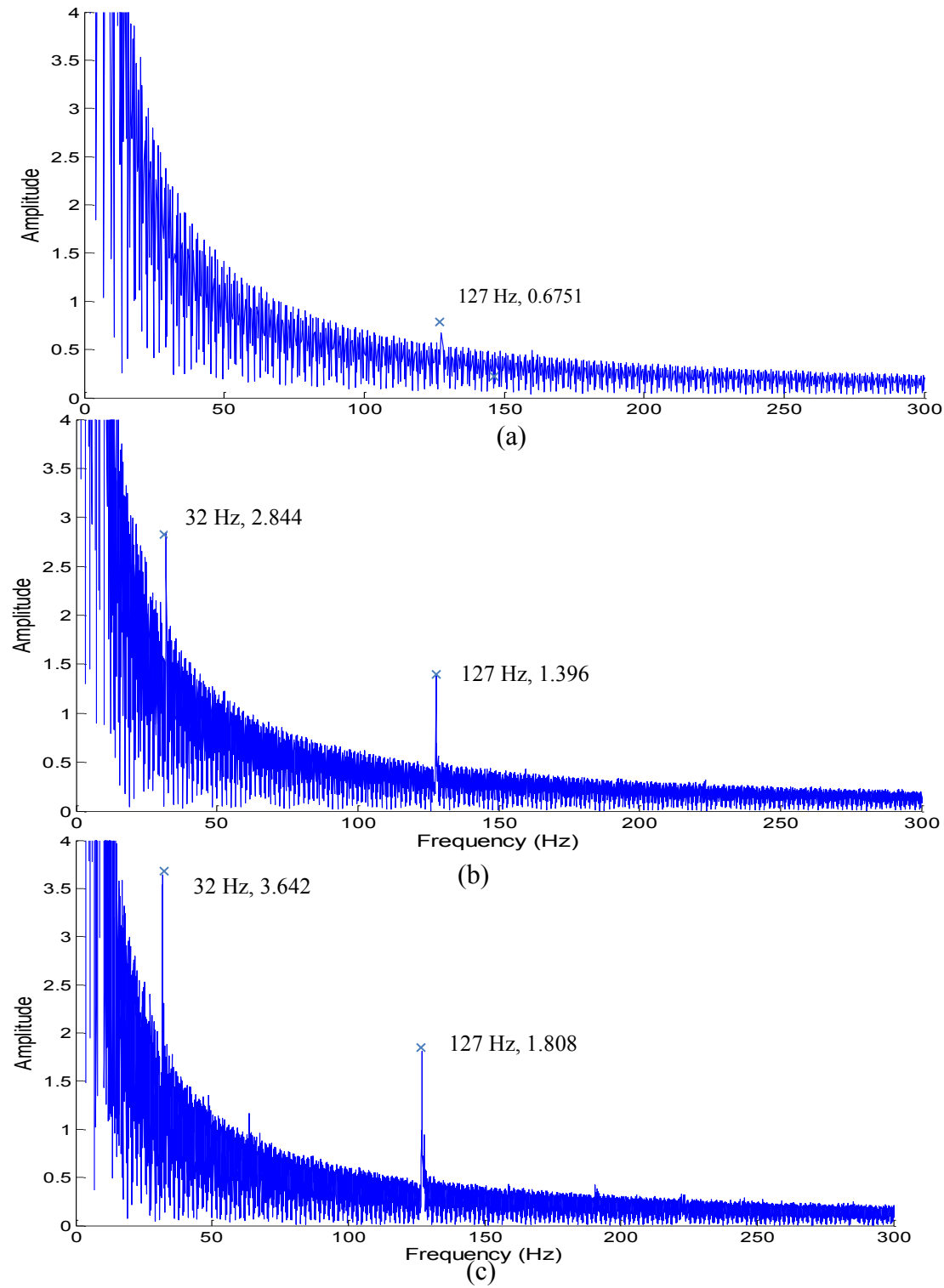


Figure 38: Frequency spectrum of tool runout: (a) laser noise; (b) spindle at 6k; (c) machining at 6k

Figure 38 shows the compared data between the three settings. By observation it is shown that the laser noise creates a low scatter of data, then when the spindle rotates at 6K RPM (19.15 m/min), amplitude spikes at 32 Hz and 127 Hz which are due to tool runout. Then at those locations there was an increase in the spikes for milling which represented the inaccuracy of the spindle under milling condition.

The results of this analysis showed important details in the experimental setup. The data showed that there was a consistent frequency due to rotation and milling. This also showed that runout was due to the spindle, not the tool and didn't significantly affect the tool life test.

4.3. Milling and Tool Wear

Two aspects of the tool were measured: flank wear and nose wear. The flank wear was expected simply due to the use of the tool. Although, nose wear occurred more significantly in titanium due to reasons that will be explained later, so it was also focused on. As seen in Figure 39, the flank wear was measured by translating the tool along the y- axis and reading the outputs from the measurement microscope. The flank wear was identified by the area on the tool where material has been removed from the tool. This area is not to be confused with the discoloration zone below the flank wear. The actual wear zone, as seen in Figure 39, is a rough textured zone.

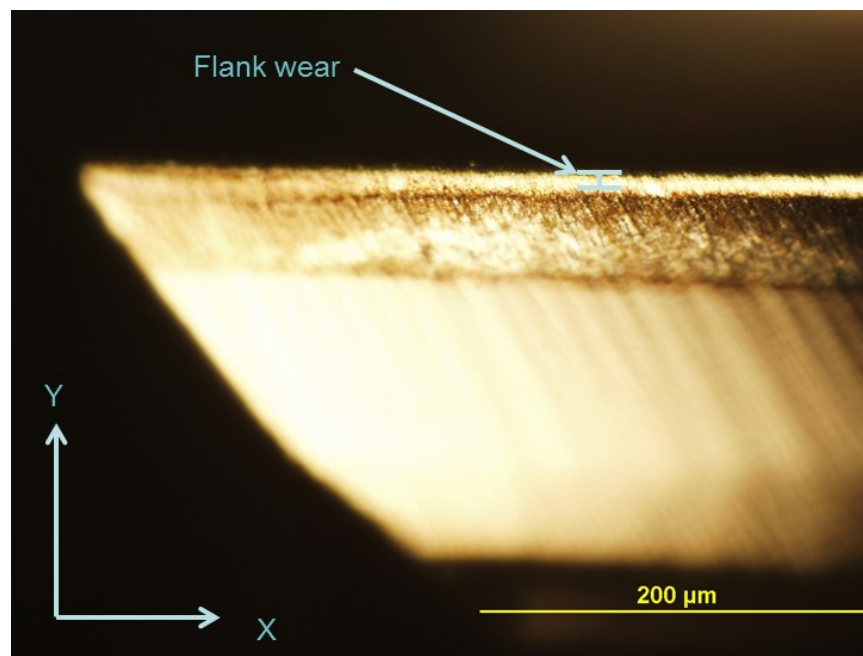


Figure 39: Flank wear identification and measurement

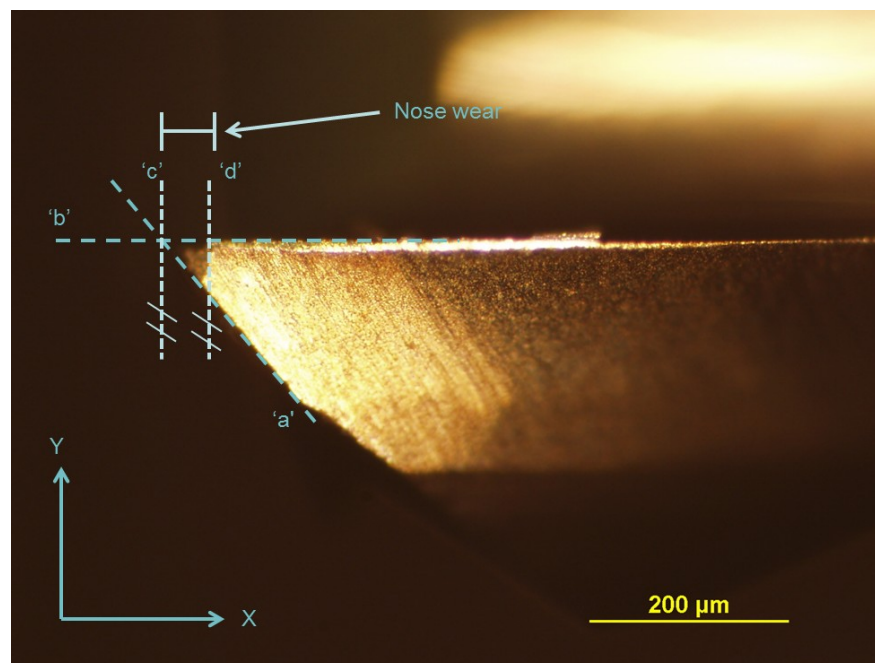


Figure 40: Nose wear identification and measurement

For the tools used on the titanium workpieces, significant nose wear was observed so it was measured. This was done using additional visualization software (ImagePro) where measurements could be performed on the image. Figure 40 shows how the nose wear was measured.

In Figure 40, 4 different lines were created to perform nose wear measurements on the tool. These lines were required because the location of the original tip needed to be extrapolated from the image due to the fact that it was worn away. This extrapolation was possible because certain areas of the tool remained intact and were able to help locate the original tip. The measurement of the nose wear was defined as the distance from the original tip of the tool to the new edge of the tool along the x-axis. Since the cutting edge of the tool remained intact beyond the cutting depth, a line was created to extend past the cutting tip; this line was marked as line 'b' in Figure 40. Then a second line was created which was of the tool edge that formed the tip of the tool, this line was marked as line 'a'. It remained intact because it did not come into contact with other material during experimentation. Now that these reference lines were created, the original tool tip was identified. The original tool tip was referenced as the intersection of lines 'a' and 'b'. The new edge of the nose was identified with another line, which was labeled 'd'. This line was created at the edge of the worn nose and the line was perpendicular to line 'b'. One last line was created to identify the nose wear, this line was line 'c' which was a line at the original tool tip and was parallel to line 'd'. The reason for perpendicularity was to make a simple measurement between two lines in the image software (ImagePro). Nose wear was the distance from line 'c' to line 'd'.

Figure 41 shows tool wear data after machining aluminum. It shows that for lower chip loads the wear rates are slightly smaller, meaning the tool will have a longer life. The sets of data represent 20k and 30k RPM (63.84 and 95.75 m/min cutting speed, respectively) along with 0.5 and 1.0 micron chip load on the micro-tool. The lower spindle RPM also shows a relatively lower wear rate than the 30k RPM. Tool nose wear on aluminum was not recorded because it was insignificant compared to flank wear.

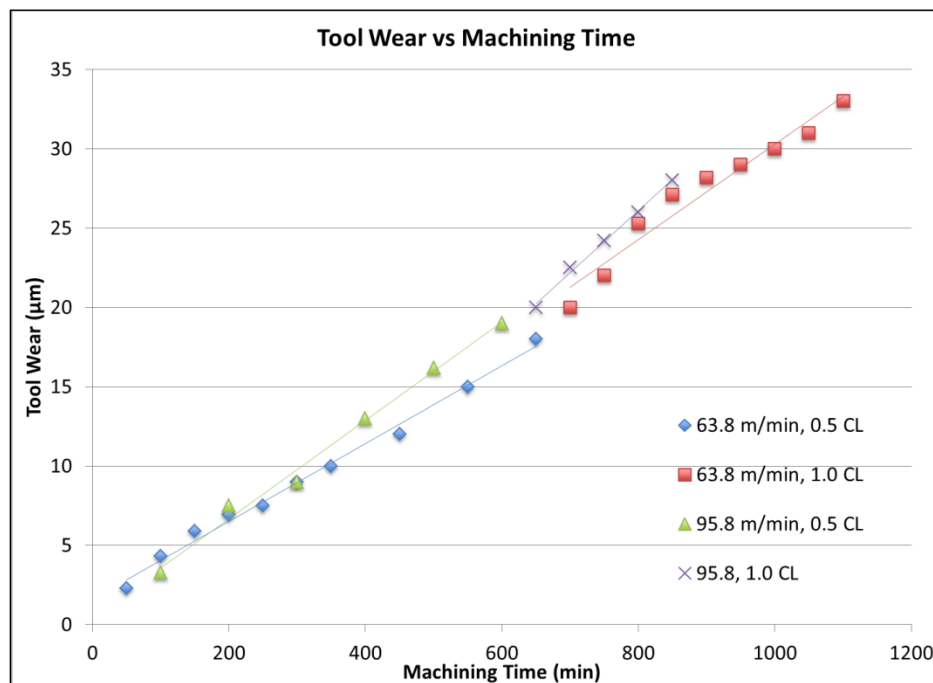


Figure 41: Tool life vs. work time in aluminum (CL:chip load, $\mu\text{m}/\text{flute}$)

Tool wear after machining titanium was not consistent. Nose wear was more significant than flank wear. Figure 42 shows a trend of high nose wear then slowly

decreased nose wear. This occurs due to the high stress concentrations at the tip or nose of the tool which chips the tool grains and pulls them out of the cobalt matrix.

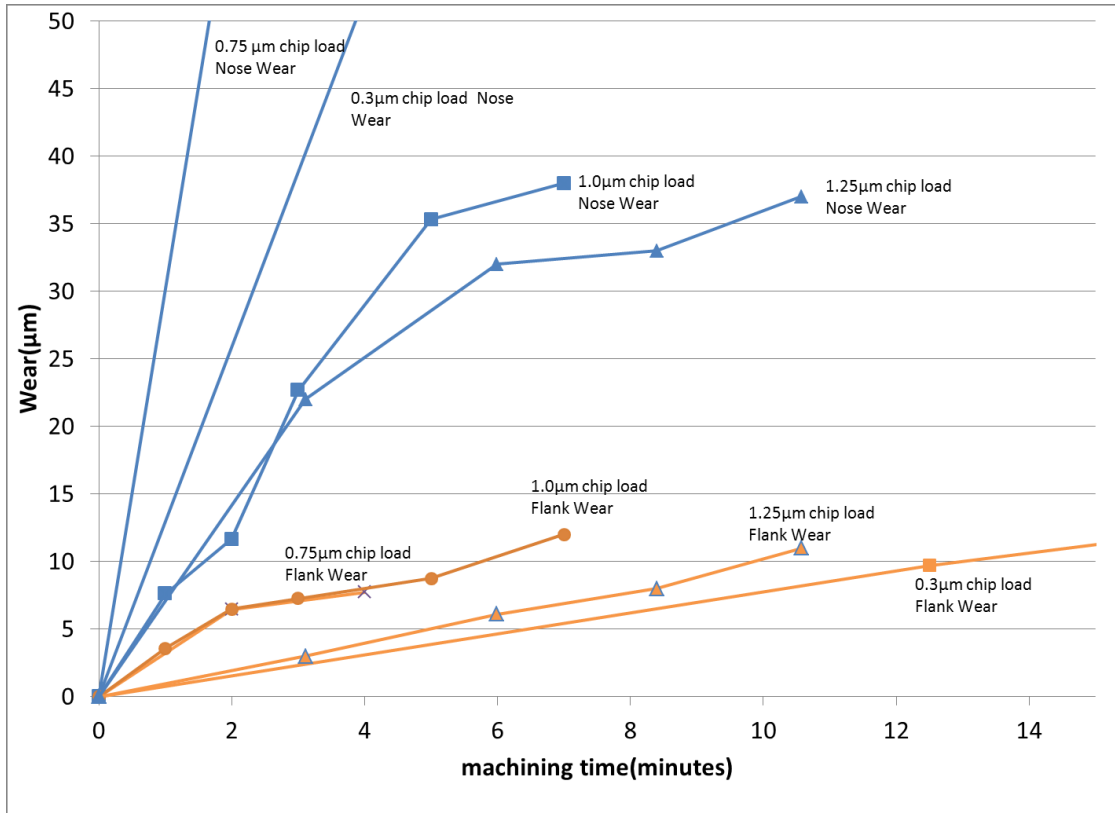


Figure 42: Nose and flank wear of machining on titanium at 79.80 m/min cutting speed

4.4. Tool Modeling

Tool modeling to predict tool life can be performed based on tool wear data. In order to model tools, the Taylor expanded tool life equation was used:

$$VT^n f^c d^g = h \quad (15)$$

The variables are cutting speed (V), tool life (T), feedrate (f), depth of cut (d) and constants (n , c , g , and h) for each tool. Since the cutting speed and depth of cut was kept constant for each tool in this study, equation (15) can be simplified as: (See Appendix F)

$$T^m f = k \quad (16)$$

Since cutting speed was held constant in tool model, a different tool model was created for each different cutting speed. By knowing the model for a tool, the equivalent feedrate can determine the approximate tool life. Alternatively, if there is a desired tool life, then a recommended feedrate can be determined.

The model was derived for aluminum when a tool performed satisfactory. On the following pages are the calculations performed to solve for constants in the wear model for machining on aluminum using cutting tools at 63.8 m/min and 95.8 m/min cutting speeds. The simplified Taylor tool life equation is used to solve for constants in equation (16). The tool lives were found by taking the linear slope of the tool wear and projecting them out to the 50 micron tool life expectancy and finding the equivalent tool life. The tool wear plots can be seen in Figure 43 and Figure 44.

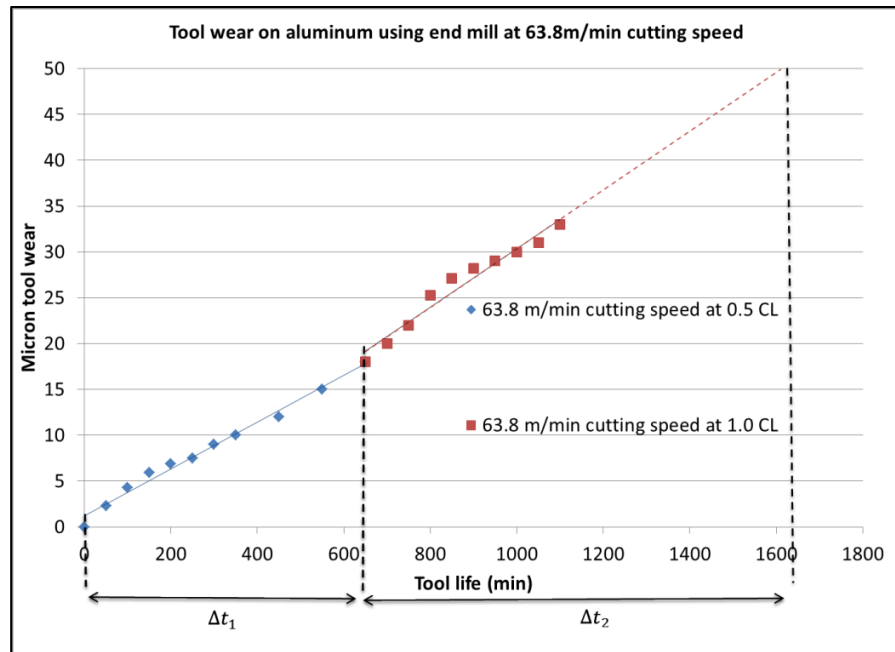


Figure 43: Tool wear on aluminum using end mill at 63.8 m/min cutting speed (CL: chip load, $\mu\text{m}/\text{flute}$)

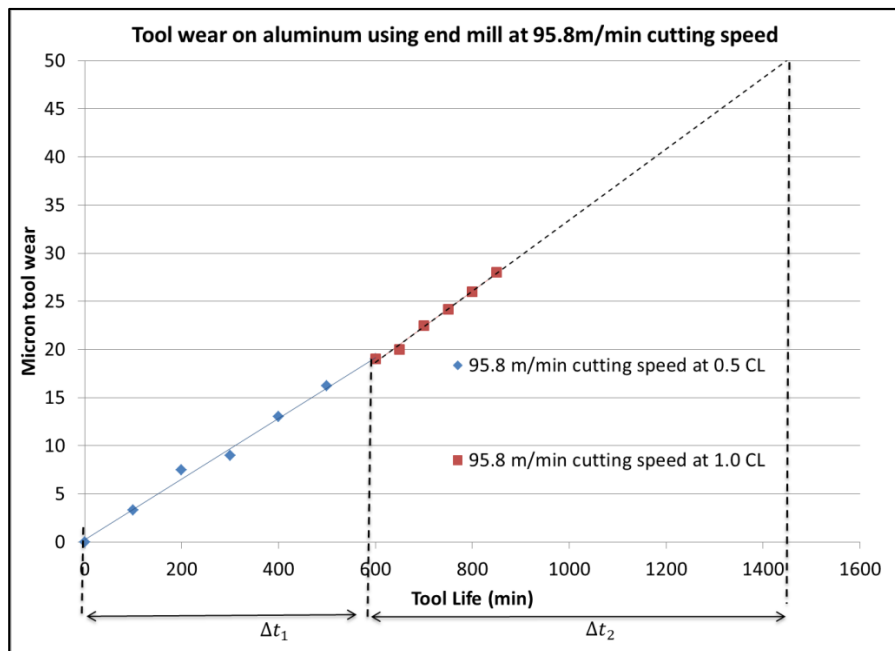


Figure 44: Tool life on aluminum using end mill at 95.8 m/min cutting speed (CL: chip load, $\mu\text{m}/\text{flute}$)

For example, the tool at 63.8 m/min cutting speed and 0.5 micron chip load had a wear rate of 0.0255 microns/min. So by giving the tool a life of 50 microns of wear the tool life was evaluated.

$$\text{Estimated life} = 50 \text{ microns} * \frac{\text{min}}{0.0255 \text{ microns}} = 1960.8 \text{ min} \quad (17)$$

The wear rate for the 63.8 m/min tool at 1.0 micron chip load was 0.032 microns/min and the tool at 95.8 m/min had wear rates of 0.0315 microns/min and 0.037 microns/min for 0.5 micron and 1.0 micron chip loads, respectively. The following table shows the estimated tool lives using the same method as in equation (17).

Table 6: Estimated tool life based on linear wear

<div> <div>Cutting Speed</div> <div>Chip Load</div> </div>	63.8 m/min	95.8 m/min
0.5 μm	1960.8 min	1587.3 min
1.0 μm	1562.5 min	1351.4 min

Tool federate can be calculated from:

$$\text{feedrate} = \text{RPM} * \text{\#of cutting flutes} * \text{chip load} \quad (18)$$

In equation (18), the chip load is written in mm per cutting flute so that the final feedrate can be represented in mm/min. A calculation for 20000 RPM and 0.5 micron chip load is shown below.

$$feedrate = 20000 \frac{rev}{min} * 2 \frac{flutes}{rev} * 0.0005 \frac{mm}{flute} = 20 \frac{mm}{min} \quad (19)$$

The other feedrates for the other parameters were solved for in the same manner and are shown in Table 7.

Table 7: Feedrate w.r.t RPM and chip load

<div style="text-align: center;">Cutting Speed Chip Load</div>	63.8 m/min (20,000 RPM)	95.8 m/min (30,000 RPM)
0.5 μm	20 mm/min	30 mm/min
1.0 μm	40 mm/min	60 mm/min

$$20 * 1960.78^m = k \quad (20)$$

$$40 * 1565.50^m = k \quad (21)$$

Equations (20) and (21) shows value inputs in equation (16) using the tool at 63.8 m/min cutting speed. With two equations the unknowns can be solved for by setting them equal to each other.

$$\ln 20 + m * \ln 1960.78 = \ln 40 + m * \ln 1565.50 \quad (22)$$

$$m = \frac{\ln 40 - \ln 20}{\ln 1960.78 - \ln 1565.50} = 3.053 \quad (23)$$

Once m is solved, it can be substituted back in to equations (20) or (21) and k can be solved for.

$$k = 20 * 1960.78^{3.053} = 2.259 \times 10^{11} \quad (24)$$

In the aluminum experiments with the tool using a 63.8 m/min cutting speed, m and k were solved to be 3.05 and 2.259×10^{11} , respectively. Using this same method, m and k were solved to be 4.31 and 1.831×10^{15} , respectively, for the tool at 95.8 m/min cutting speed.

Cumulative tool model can now be derived. First, the overall time must be found, which is the time each tool was used at a specific feedrate. This is shown in equation (25) as the summation of times and equation (26) shows the evaluated time for the 63.8 m/min tool.

$$T_e = \Delta t_1 + \Delta t_2 \quad (25)$$

$$T_e = 650 + 1000 = 1650 \text{ min} \quad (26)$$

Similarly, Figure 44 shows the tool at 95.8 m/min had an equivalent time, T_e , of 1450 min. The equivalent feedrate is shown in equation (27) and the full derivation can be found in Appendix F.

$$f_e^{1/m} = \frac{1}{QT_e} (\Delta t_1 f_1^{1/m} + \Delta t_2 f_2^{1/m}) \quad (27)$$

In the equations, Δt_i is for the tool life at the specific chip load and f_i is for the specific feedrate. Both of these can also be referenced in Figure 43 and Figure 44. Also, T_e is the time of the equivalent total usage time of the tool and f_e is the mathematical equivalent to the two different cutting speeds.

In the model we solve for Q , which is the sum of the fractions of each tool usage per estimated tool life. The theoretical value of Q is 1 since it is the total tool life.

$$\frac{\Delta t_1}{T_1} + \frac{\Delta t_2}{T_2} = Q \quad (28)$$

$$Q = \frac{650}{1960.8} + \frac{1000}{1562.5} = 0.97 \quad (29)$$

The solved equation above is for the first tool at 63.8 m/min and each Δt_i can be shown in Figure 43 and Figure 44. Q in the 95.8 m/min experiment was solved to be 1.01 by summing the partial times for the other cutting tool using equation (28) and the

same procedure as the other tool. Now the equivalent feedrate can be solved for by substituting back into equation (27).

$$f_e = \left(\frac{1}{0.97 * 1650} (650 * 20^{1/3.053} + 1000 * 40^{1/3.053}) \right)^{3.053} \quad (30)$$

$$= 31.01 \text{ mm/min}$$

For the tool at 95.8 m/min cutting speed, the equivalent feedrate was found to be 45.65 mm/min. In Figure 45 the model is verified by plotting the equivalent cumulative tool life and feedrate with the observed tool lives and feedrates in the experiment. Since we can make a linear relation in the data sets we can confirm that the model creates valid equivalent feedrate and tool life. This is because the equivalent feedrate and tool life refers back to the simplified Taylors equation (16) and agree with the experimental data points.

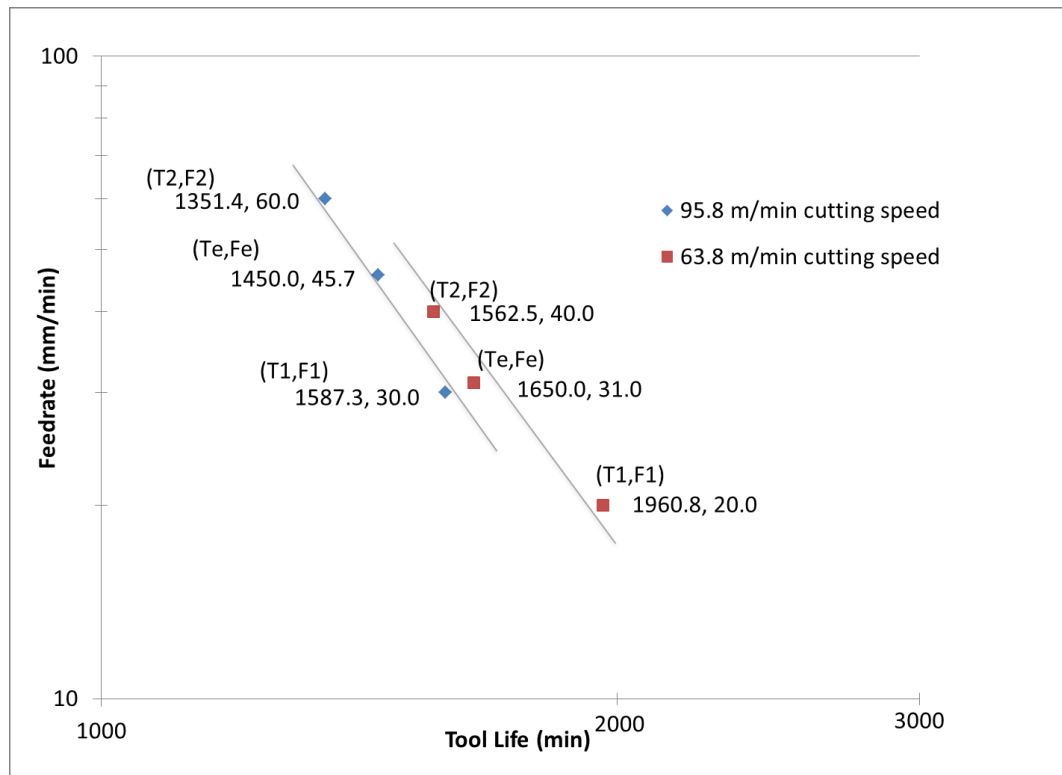


Figure 45: Feedrate vs tool life on log log plot for both cutting tools

The validity of the model allows us to make valid conclusions. First, a cumulative result of multiple settings in the micro-milling experiment can be evaluated to equal a single setting. Second, since a single setting can be found a single tool life can be estimated much simpler which will save on the time and cost of performing multiple machining studies. Also, by observing Figure 45, it can be shown that working at lower cutting speeds using the same feedrate, less wear will be observed, thus longer tool life.

4.5. Microstructure

When machining metal, material in front of a tool is sheared off and forms a chip. The grains below a tool are plastically deformed under a tool. When a tool moves to a different location, those grains recover elastically, but still shift with remaining plastic strains and are work hardened. Microstructure observations showed evidence of work hardening at the machined surface of the workpiece. The plastic deformation that was observed in the microstructure was twinning. The observation showed evidence of plastically induced twinning and was consistent with studies from Chae (2005) and Thepsonthi (2010) where material deformation was related to the minimum chip thickness which increases with the bluntness of the tool.

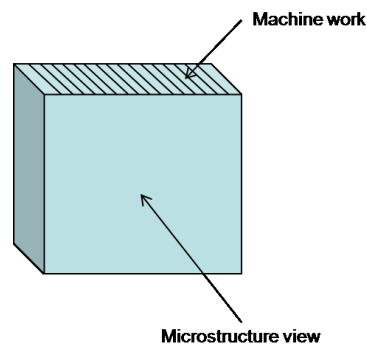


Figure 46. View of microstructure of machined sample

Figure 47a and Figure 47b show evidence of grain twinning near the machined surface. Figure 47c shows much less twinning and represent less work hardening at a 1.0 micron chip load. These deformations are linked back to the high accounts of nose

wear which blunt the tool. This causes the significant plastic deformation on the material below the cutting surface. To more accurately analyze the amount of work hardening on the samples with respect to the chip loads the microhardness of the samples must also be taken into account.

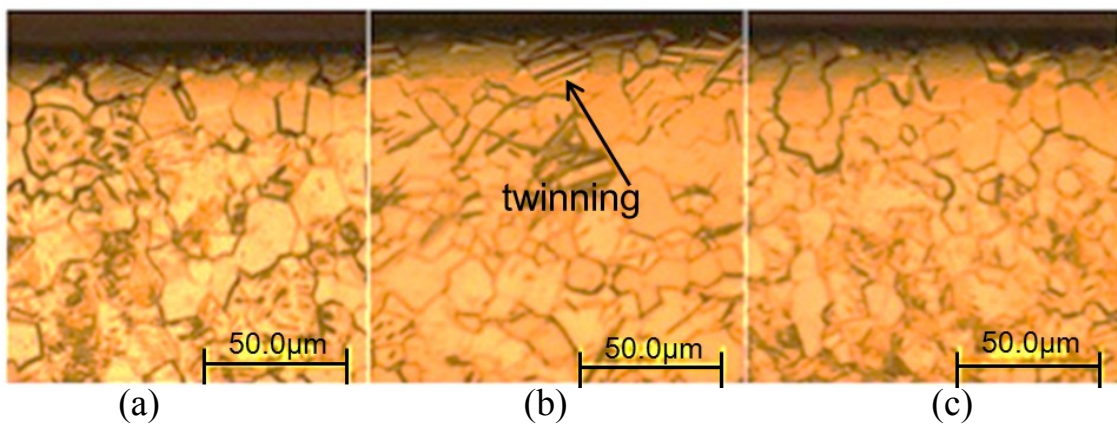


Figure 47: Grain deformation (twinning) near machined surface. Microstructure images of 0.3 (a), 0.75 (b), and 1.0 (c) micron chip loads on CP titanium. The top of the image is the cutting surface and the cutting was performed in a perpendicular direction to the image.

4.6. Microhardness

Microhardness is another technique to verify work hardening due to machining. The average hardness of the zone away from the machined surface was approximately 218 Vickers. Hardness tests showed that average hardness near the surface was greatest among the sample at 0.75 µm chip load and the least hardened material was at 1.0 µm chip load. This is consistent with the nose wear of the tool on titanium. The sample at 0.75 µm chip load had an 18% average increase in hardness near the machined surface.

Figure 42 shows the highest nose wear for tool at 0.75 μm chip load and lowest for tool at 1.0 micrometer chip load. High nose wear blunts the cutting tool and causes significant plastic deformation on material below the cutting surface. Tool quality is still an issue because chipping at nose. The highest work hardening should be for lowest chip load because at lower chip loads the tool should plow the more material and be below the minimum chip thickness.

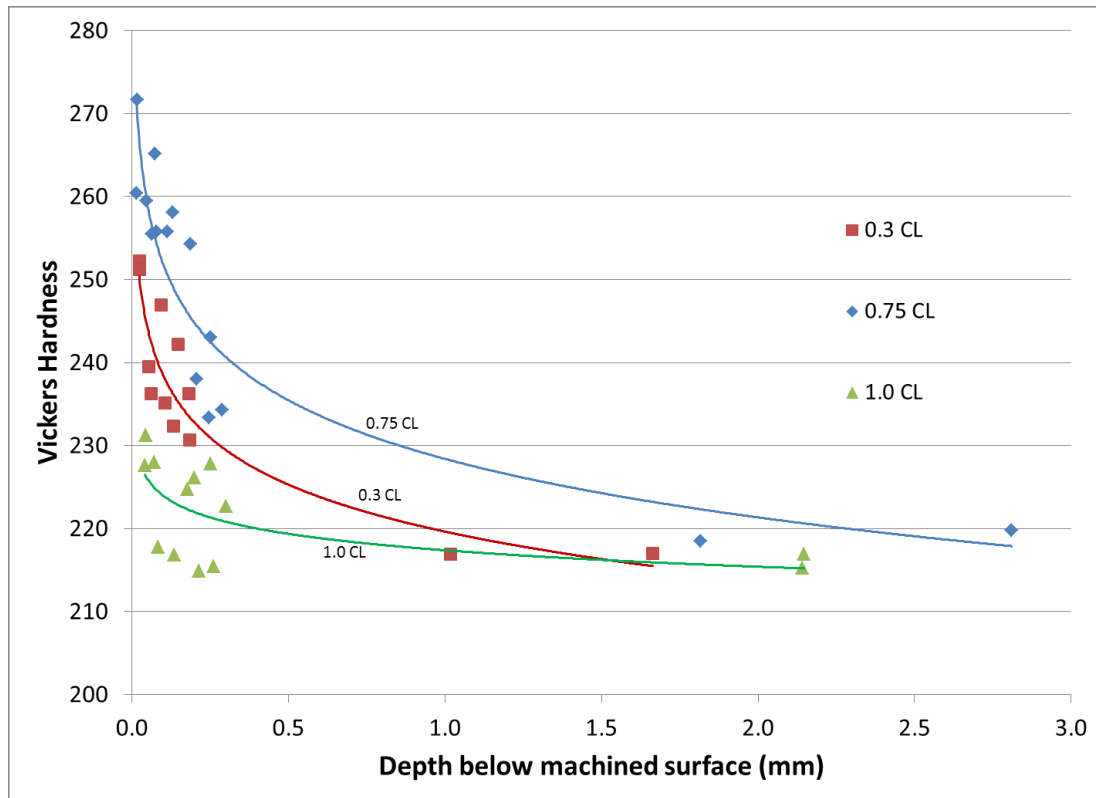


Figure 48: Microhardness below surface of machined titanium (CL: chip load, $\mu\text{m}/\text{flute}$)

4.7. Finite Element Analysis

Previous research measured a flexure stress of 4.7 GPa after 3-point bending of the micro-tools (Chittipulo, 2009). This gave us the ability to test the micro-tool for similar fracture parameters on different materials. Once the failure criterion was determined, the failure zone was related to its chip load and axial depth for which combinations of parameters would give these stress levels. Various axial depths of cut and chip loads were chosen and their equivalent forces were calculated. By changing the parameters to find equivalent combinations that would create these levels of stress (flexure strength) failure zones could be created. Figure 49 shows how forces were imposed on the model and stress limits were measured.

Figure 50 shows the zone in which tool tip chipping was observed in the finite element analysis of the tool. The tool tip chipping occurs when Von-Misses stress levels calculated by FEA exceeds the flexure strength of cutting tool. The data points of tool chipping were where the axial depth and chip load created a force that resulted in stress levels equivalent to the flexure strength at the tip of the tool. These data points were linearly related and a tool chipping 'zone' was created (see following figure) where any of the axial depth and chip load combinations in this area would result in above flexure stress levels at the tool tip.

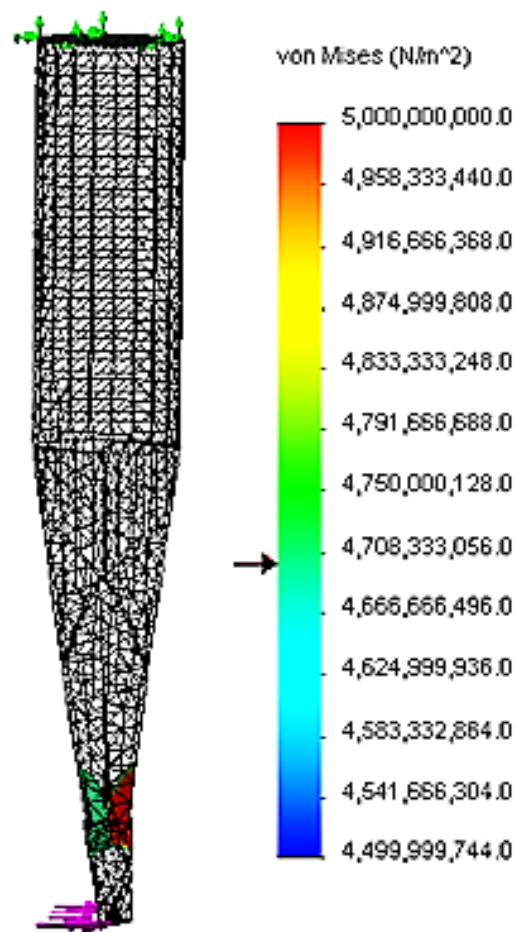


Figure 49: FEA von Mises results at failure criterion of 4.7 GPa flexure strength at tool diameter.

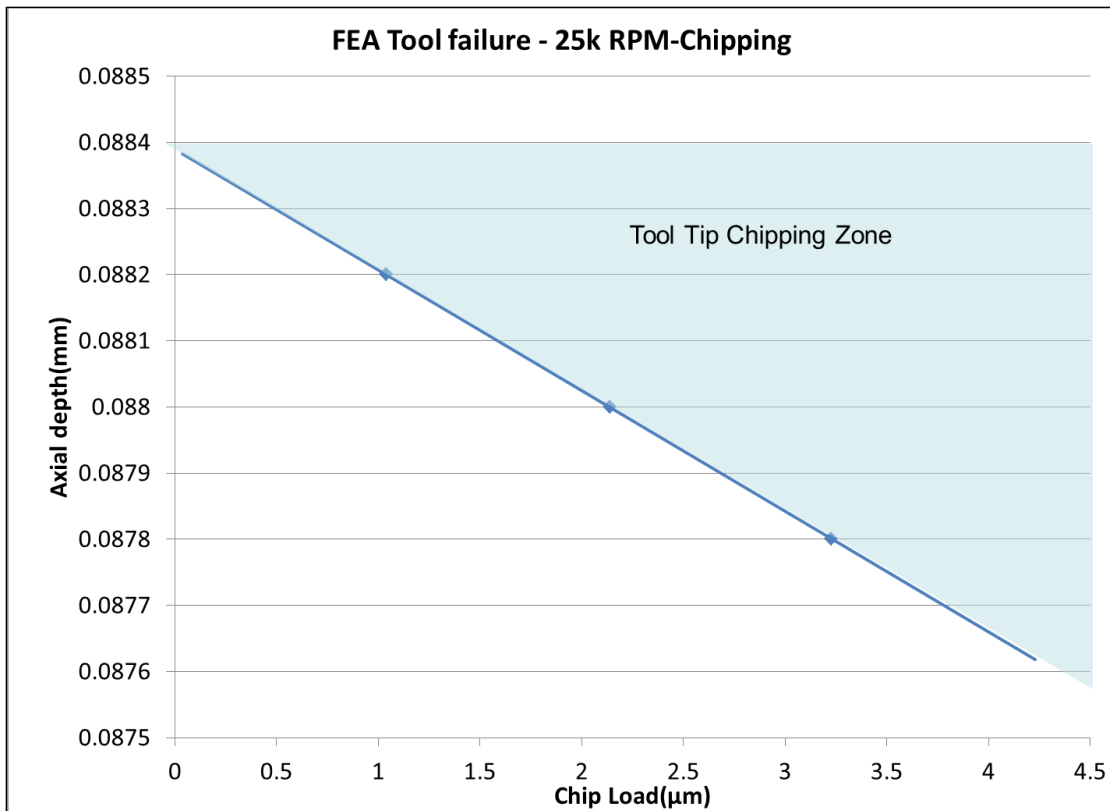


Figure 50: FEA-tool tip chipping zone at 25k RPM (79.80 m/min) on titanium

Figure 51 shows the tool fracture zone, settings below the data line represent settings that would not result in tool fracture. The area below the data line will still most likely result in tool chipping when cross referenced with the tool chipping zones as seen in Figure 50.

Figure 52 shows the tool fracture zone on aluminum workpiece. This can withstand a much higher axial depth of cut before fracture because the shear stress of aluminum is approximately 207 MPa as opposed to titanium which is double, at 440 MPa.

These two graphs Figure 51 and Figure 52 are validated by the cutting parameters used in the experiment. During the study the chip loads and axial depths were kept below these fracture levels and no tool fracture occurred. Also, in experiment and in FEA high chip loads were able to be used on the aluminum due to lower stress levels on the tool.

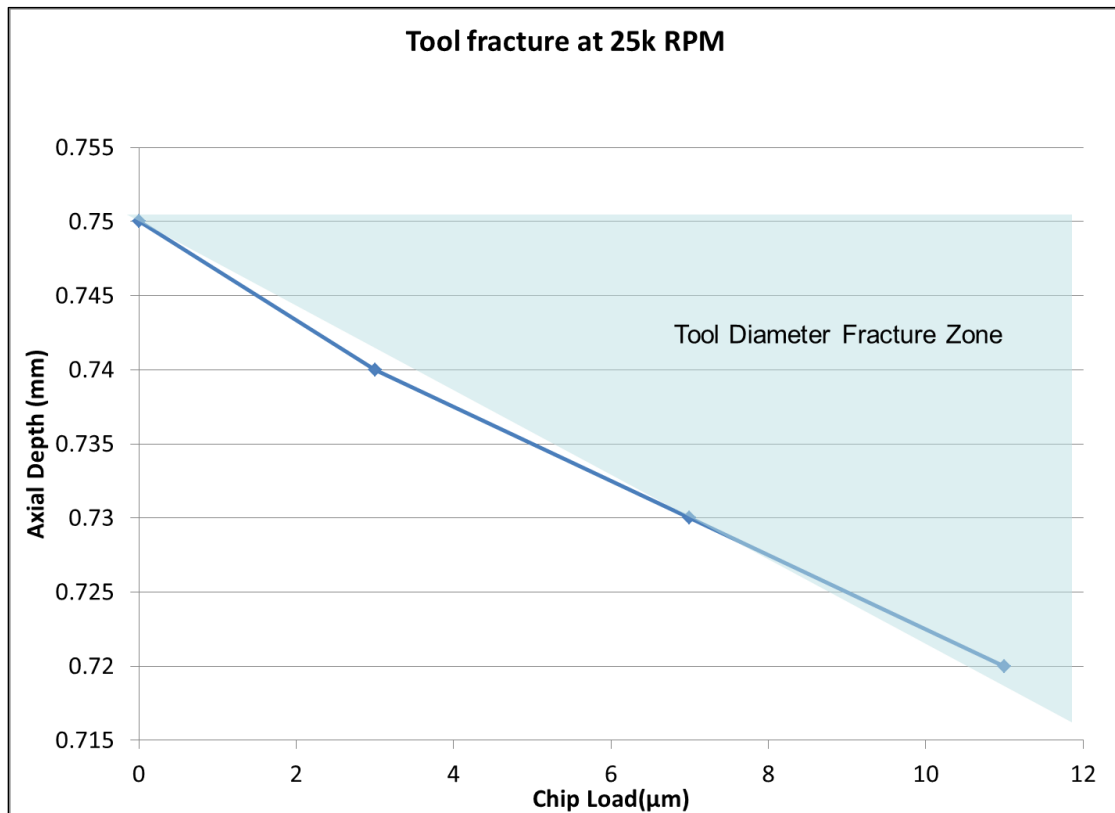


Figure 51: Tool fracture FEA with fracture zone, tool at 25k RPM (79.8 m/min) on CP titanium

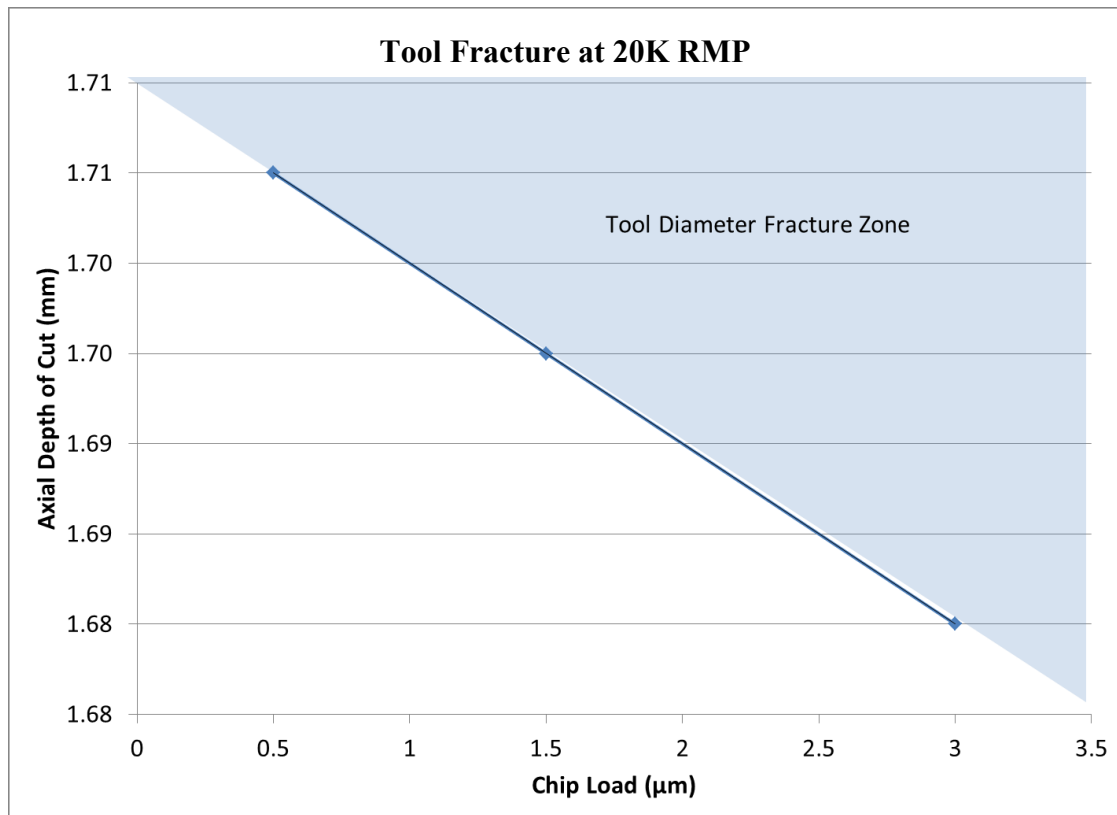


Figure 52: Tool fracture FEA with fracture zone, tool at 20k RPM (63.84 m/min) on aluminum 6061-T6

After considerations of the work hardening occurring on the titanium, more accurate approaches to this FEA should be made in the future. The analysis should be done using the interaction between the workpiece and the tool not just assumed static forces. Since the titanium is work hardened easily, the theoretical force required to shear a chip is much less than the amount of force actually imposed on the tool. Also, to accurately model plastic deformation, the analysis must account for nonlinearity of titanium's stress strain relationship (Machado & Wallbank, 1990).

By using the FEA, it was shown that the parameters used were sufficient to avoid tool fracture. The axial depths and chip load combination for titanium and aluminum did not create stress past the flexure strength at the tool diameters. It was shown that the titanium settings would chip the tool, which was shown from experiment. Future endmilling on titanium should be mindful of this zone to avoid tip chipping.

This automated method was verified against hand calculations. By assuming simple torsion and bending on a cantilever beam, the maximum shear, bending and torsion forces were calculated. The equivalent von Mises stress was 4% of the output value from the FEA. The differences between the hand calculations and FEA values were due to the more complex geometries calculated by the FEA. (Full calculations are shown in Appendix E).

5. CONCLUSIONS AND RECOMMENDATIONS

This research studied micromilling of aluminum 6061-T6 and CP titanium. It was found that:

1. Fast Fourier transformation of the time domain vibration data into frequency domain indicated that the main vibration, about 4 μm , was due to the spindle runout and tool deflection when machining.
2. Linear flank wear and negligible nose wear were measured on micromilling tools when machining aluminum. The tool wear rate increased with the tool feedrates. Significant nose wear of microtools was measured when machining titanium. This caused an increase of approximately 18% in microhardness of the subsurface and damaged the subsurface microstructure.
3. Bending and torsional loads were calculated for aluminum and titanium. Finite element analysis was used to estimate the appropriate thresholds for cutting parameters to avoid tool fracture. No tool breakage was experienced in this study.

For future works, it is recommended that:

1. Although successfully micromilling aluminum, the microtools in this study failed due to rapid nose wear. Microtools with better adhesion and smaller grains should be studied. Proper coating of microtools should be considered for future studies.
2. Tool life models should be adapted to consider edge milling with different radial depths.

REFERENCES

- Boyer, R.; Welsch, G.; Collings, E.W. (1994): *Materials Properties Handbook Titanium Alloys*. ASM International: Materials Park, Ohio; pp. 125-160.
- Chae, J.; Park, S.S.; Freiheit, T. (2005) Investigation of micro-cutting operations. *International Journal of Machine Tools and Manufacture*, 46: 313-332.
- Chittipolu, Sujeev. (2009) Failure prediction and stress analysis of micro-cutting tools. Masters Thesis, Texas A&M University, College Station, TX.
- Collins, E.W. (1984) *Physical Metallurgy of Titanium Alloys*. ASM International: Columbus, OH; 1:125-130
- Filiz, Sinan; Eckert, Udo; Pinteragel, Stefan; Schubert, Andreas; Ozdoganlar, Burak. (2010) An investigation of micro-machining parameters for fabricating ear-implants from titanium. *International Committee on Micro-Manufacturing*, 61: 369-372.
- Holt, John M.; Gibson, C; Ho, Y.H. (1999) *Structural Alloys Handbook*. CINDAS: Wabash, Indiana.
- Hung, N.P.; Zhong, C.H. (1996) Cumulative tool wear in machining metal matrix composites Part I: Modeling. *Journal of Materials Processing Technology*, 58: 109-113.
- Lai, Xinmin; Li, Hongtao; Li, Chengfeng; Lin, Zhongin; Ni, Jun. (2008) Modelling and analysis of micro scale milling considering size effect, micro cutter edge radius and minimum chip thickness. *International Journal of Machine Tools and Manufacture*, 48: 1-14.
- Liu, X.; DeVor, R.E.; Kapoor, S.G. (2004) An Analytical Model for the Prediction of Minimum Chip Thickness in Micromachining. *Journal of Manufacturing Science and Engineering*, 128: 474-481.
- Lutjering, G; Williams, J.C.; Gysler, A. (2000) Microstructure and Mechanical Properties of Titanium Alloys. *World Scientific Publishing* , 2: 1-74.
- Machado, A.R.; Wallbank, J. (1990) Machining of titanium and its alloys- a review. *Proceedings Institution of Mechanical Engineers*, 204: 53-60.
- McKeown, P.A. (1987) The Role of Precision Engineering in Manufacturing of the Future. *Annals of the CIRP*, 36: 495-501.
- Okazaki, Yuichi; Mishima, Nozomu; Ashida, Kiwamu. (2004) Microfactory—Concept, History, and Developments. *Journal of Manufacturing Science and Engineering*, 126: 837-844.

- Rahman, M.; Kumar, A Senthil; Salam, M.U. (2002) Experimental Evaluation on the effect of minimal quantities of lubricant in milling. *International Journal of Machine Tools and Manufacturing*, 42: 539-547.
- Schueler, G.M.; Engmann, J.; Marx, T.; Haberland, R.; Aurich, J.C. (2010) Burr formation and Surface Characteristic in micro-end milling of titanium alloys. *Burrs- Analysis, Control and Removal*, 10: 129-138.
- Thepsonthi, T.; Ozel, T. (2010) Sensor Assisted Monitoring and Optimization of Process Parameters in Micro-end Milling of Ti-6AL-4V Titanium Alloy. *International Committee on Micro-Manufacturing*, 40: 227-235.
- Wang, Jinsheng; Gong, Yadong; Abba, Gabriel; Cao, Jianfeng; Shi, Jiashun; Cai, Guangqi. (2007) Micro Milling Technologies for MEMS. *Memstech*, 1: 86-95.
- Womack, James; Jones, Daniel. (1996) *Lean Thinking*. Free Press: New York, New York; pp. 17-20.

Supplemental Sources Consulted

- Bao, W.Y.; Tansel, I.N. (2000) Micro end milling operations Part II: tool runout. *Journal of Machine Tools and Manufacturing*, 40: 2175-2195.
- Bojosievici, C. (1986) Analysis of surface finish in milling by power spectrum density measurement. *Precision Engineering*, 8: 24-26.
- Grum, J.; Kisin, M. (2003) Influence of microstructure on surface integrity in turning-part II: the influence of a microstructure of the workpiece material on cutting forces. *International Journal of Machine Tool and Manufacturing*. 43:1545-1551.
- Hung, N.P.; Loh, N.L.; Xu, Z.M. (1996) Cumulative tool wear in machining metal matrix composites Part II: Machinability. *Journal of Material Processing Technology*, 58: 114-120.
- Jawaid, A.; Sharif, S.; Koksai, S. (2000) Evaluation of wear mechanisms of coated carbide tools when face milling titanium alloy. *Journal of Materials Processing Technology*, 99: 266-274.
- Kumanchik, Lee M.; Schmitz, Tony L. (2007) Improved analytical chip thickness model for milling. *Precision Engineering*, 31: 317-324.
- Lee, Kiha; Essel, Ingo; Dornfeld, David A. (2001) Burr formation in micro-milling. *Machining Processes ASPE Proceedings 2001*, November 10-15 (2001). Crystal City, Virginia, USA.

- Niinomi, Mitsuo. (1998) Mechanical properties of biomedical titanium alloys. *Materials Science and Engineering*, A243: 231-236.
- Obikawa, T.; Usui, E. (1996) Computational Machining of Titanium Alloy- Finite Element Modeling and a Few Results. *Journal of Manufacturing Science and Engineering*, 118 208-215.
- Shivpuri, R.; Hua, J.; Mittai, P.; Srivastava, A.K. (2002) Microstructure-mechanics interactions of modeling chip segmentation during titanium machining. *CIRP Annals-Manufacturing Technology*, 51: 71-74.
- Tansel, I.N.; Arkan, T.T.; Bao, W.Y.; Mahendrakar, N.; Shisler, B.; Smith, D.; McCool, M. (2000) Tool wear estimation in micro-machining, Part I: tool usage-cutting force relationship. *International Journal of Machine Tools and Manufacturing*, 40: 599-608.
- Tansel, I; Rodriguez, O.; Trujillo, M.; Paz, E.; Li. W. (1998) Micro end milling- I Wear and breakage. *International Journal of Machine Tools and Manufacturing*, 38: 1419-1436.
- Weinert, Klaus; Surmann, Tobias; Enk, Dirk; Webber, Oliver. (2007) The effect of runout on the milling tool vibration and surface quality. *Academic Society for Production Engineering*, 1: 265-270.
- Zheng, Li; Chiou, Yun Shun; Liang, Steven. (1996) Three Dimensional Cutting force analysis in end milling. *International Journal of Mechanical Science*, 38: 259-269.

APPENDIX A**PROPERTIES AND SPECIFICATIONS OF MATERIALS AND EQUIPMENT**

A.1 HAAS OM2 Specifications

- The machine is equipped with a 50,000 rpm brushless electric micro-motor spindle with 270W power rate.
- The maximum values of feedrate and cutting speed obtained on this micro-milling machine are equal to 19.2m/min (757 ipm) and 12.7 m/min (500 ipm)
- The maximum travel distance along the X and Z axes are 12” or 305 mm and a travel distance of 10” or 254 mm along the Y axis
- Four-axis machining can be performed using a microrotary table or five axis machining by installing microtrunnion table (HAAS 2009)

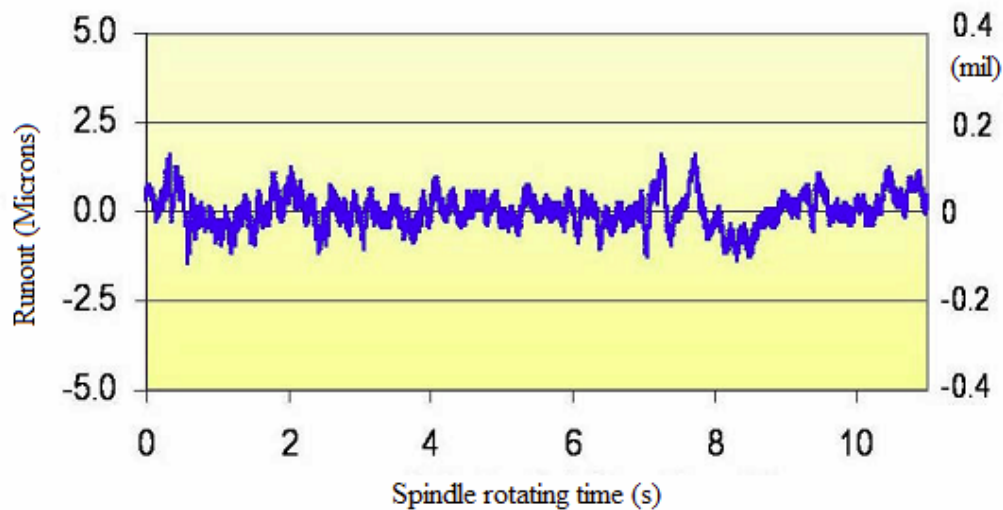


Figure A.1: Runout of HAAS OM2 air spindle at 10,000 RPM(31.92 m/min)



Figure A.2: HAAS OM2 office milling machine (HAAS 2009)

A.2. Keyence LK-G157 Laser Specifications

The main features of this measurement sensor are:

- Sampling speed of 50 KHz
- Measuring range of 150 ± 40 mm (5.91 ± 1.57 ")
- Capable of accurately measuring targets rotating or vibrating at high speed.
- Incorporates state of the art algorithms for measuring plastic, transparent or translucent, and metal targets effectively. The LK- Navigator helps to optimize the laser beam to use it effectively based on the measuring surface (Keyence 2009).

A.3. UNIST COOLUBRICATOR SYSTEM

- The system is equipped with a 5- 200 pulse/minute pulse generator and a 0.2 drops per cycle to 1.0 drop per cycle liquid metering pump (1 drop equals 0.033cc).
- A brass knurled air metering screw controls the flow of air atomizing out the nozzle which determines the density and distance of the spray.
- The spray output has an included angle of 15-20 degrees depending on the amount of air introduced (Unist 2007).

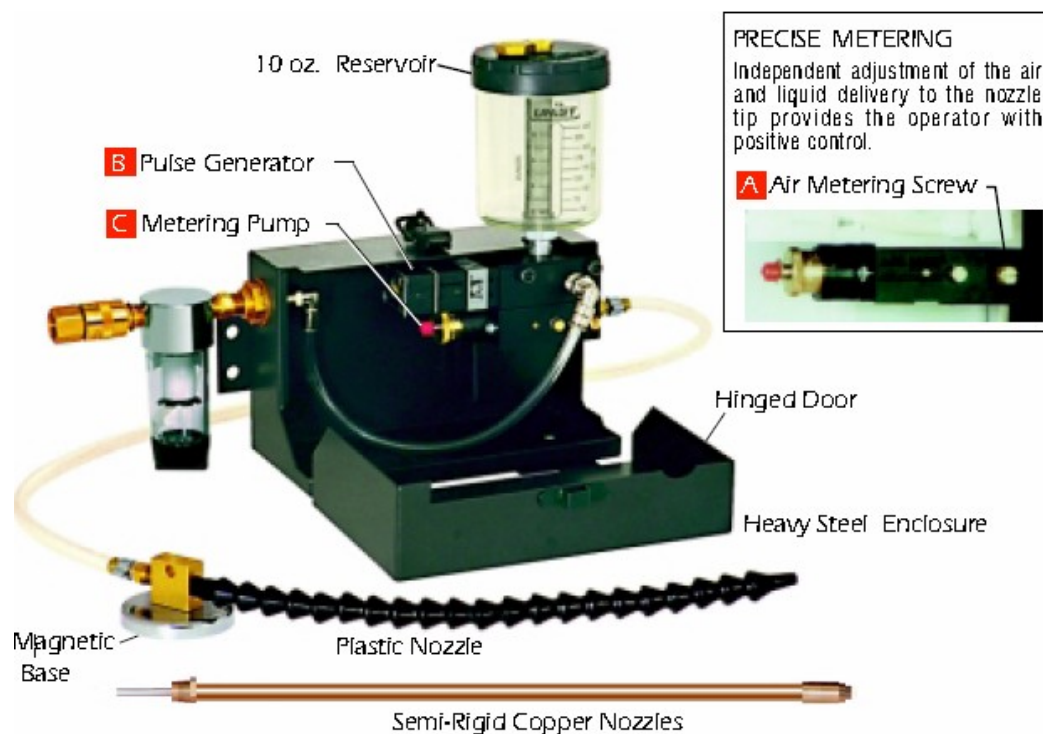


Figure A.3: Unist mist system showing different components (Unist, 2007)

The UNIST lubricants are biodegradable that are formulated to work with ferrous and non-ferrous materials. They are also vegetable based lubricants

There are many advantages to UNIST lubricants

- Non-polluting, non-toxic, non-hazardous
- Non-drying
- Help minimize exit burrs
- Performs well under pressure and heavy duty cutting cycles.

A.4 M.A. Forde Carbide End Mill

The micro-end mill used was a 1.016 mm micro end mill provided by M.A. Ford. The tool was a Tuff Cut 2-flute made of uncoated tungsten carbide. The diameter was 0.04 inches or 1.016 mm.

Table A.1 Micro end mill M.A. Ford #1640400 dimensions (M.A. Ford, 1998)

Tool #	EDP	Size(in.)	L.O.A.	Flute Length	Shank Diam.
<u>16404000</u>	16495	0.04	1/1/2002	0.08	1/8

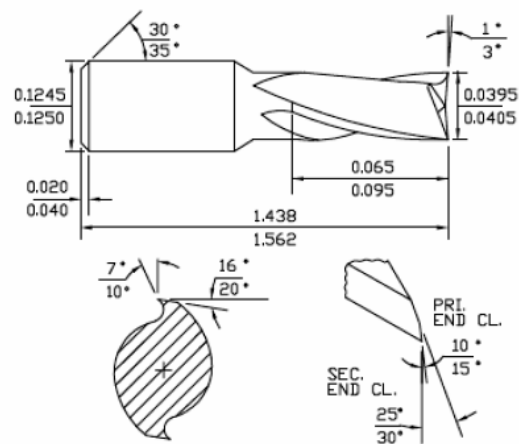


Figure A.4: Micro tool #1640400 dimensions and geometry (M.A. Ford 1998)

Table A.2: Tungsten carbide properties (M.A. Ford, 1998)

Density	Vickers Hardness (VH)	Knoop Hardness
$14500 \frac{kg}{m^3}$	1730	1870

A.5 Aluminum 6061-T6

Aluminum alloy 6061-T6 was used within the tool wear experimentation. The composition of the alloyed aluminum is shown in Table A.3 and the mechanical properties are listed Table A.4.

Table A.3: Aluminum 6061-T6 chemical composition (Holt et al., 1999)

Al	Cr	Cu	Fe	Mg	Si	Zn
			Max		Max	Max
Remainder	0.04-0.35	0.15-0.40	0.7	0.8-1.2	0.40-0.8	0.25

Table A. 4: Aluminum 6061-T6 mechanical properties (Holt et al., 1999)

Mechanical Properties		
Hardness, Knoop	120	120
Hardness, Vickers	107	107
Ultimate Tensile Strength	310 MPa	45000 psi
Tensile Yield Strength	276 MPa	40000 psi
Modulus of Elasticity	68.9 GPa	10000 ksi
Ultimate Bearing Strength	607 MPa	88000 psi
Bearing Yield Strength	386 MPa	56000 psi
Poisson's Ratio	0.33	0.33
Fatigue Strength	96.5 MPa	14000 psi
Shear Modulus	26 GPa	3770 ksi
Shear Strength	207 MPa	30000 psi

A.6 Titanium

Titanium, in an unalloyed state, is nearly as strong as some steels but about 45% lighter, so it has a very high strength to weight ratio. Also, the shear strength of titanium is approximately 440 MPa (Collins, 1984).

Table A.5: Titanium mechanical properties (Lutjerring, 2000)

	E	Sigma1	UTS	Elongation
Commercially Pure Alloy	(GPa)	(MPa)	(MPa)	(%)
Grade 1	105	170	240	24
Grade 2	105	275	345	20
Grade 3	105	380	445	18
Grade 4	105	480	550	15

Titanium in general is classified as a hard to machine material due to its increased hardness (approx. 220 on Vickers scale) and poor thermal properties (Boyer et al., 1994). Some other mechanical properties are shown in Table A.5.

A.7 AgieCharmilles Wire EDM

The machine itself has capabilities to cut small pieces like the work material or larger samples if needed. The table size is 350 x 250 x 250 mm and can taper at 25 degrees as well. It uses wires of 0.15 to 0.30 mm so it has a reasonable small amount of cutout path, but more importantly it can cut pieces at under 0.25 microns. The high

quality surface finish allows cutting of samples with minimal cutting tool residuals and is very efficient for the experiments that are needed in this research.



Figure A.5: AgieCharmilles wire EDM (Agie 2011)

APPENDIX B
MATLAB PROGRAMS

B.1 MATLAB code for contact angle plot

```

clear all;

k=-1;
i=1;

s=.8;%xaxis min(start)
e=1;%xaxis max(end)
for x=s:.001:e %0.001 plot resolution
    if(acosd(x)<=90)
        k=1;
    else
        k=0;
    end

    PV(i)=(24/pi*(1-k*x^2)^(3/2)/(2-3*x+x^3))^(1/3);
    i=i+1;
end
figure(2)
x=s:.001:e;
[haxes,hline1,hline2]=plotyy(x,PV,x,acosd(s:.001:e))

axes(haxes(1))
ylabel('P/V (1/3)')

axes(haxes(2))
ylabel('contact angle')
grid on

xlabel('cos()')

deg_pv

```

B.2. MATLAB code for contact angle table

```

s=-1;
e=-1;
deg_pv(:,1)=.005:.01:180;
for x=1:1:length(deg_pv(:,1)) %1 deg plot resolution
    if(cosd(deg_pv(x,1))<=90)
        k=1;
    else
        k=0;
    end

    deg_pv(x,2)=(24/pi*(1-k*cosd(deg_pv(x,1))^2)^(3/2)/(2-
3*cosd(deg_pv(x,1))+cosd(deg_pv(x,1))^3))^(1/3);
    i=i+1;
end

V=.1:.01:.3
P=1:.1:3
for i=1:1:length(P)
    for j=1:1:length(V)
        PV(i,j)=interp1(deg_pv(:,2),deg_pv(:,1),P(i)/(V(j)^(1/3)))
    end
end
end

```

B.3 MATLAB code for FEA force calculations

```

clear all;

clc;

rDOC=0.558; %depth into piece(profile)
aDOC=.72; %depth from surface (0.381 original)
RPM=25000; %rpm (rotations/min)
CL=10 %micron

Fr=CL*.001*2*RPM ; %Feedrate (mm/min)
deltaX=Fr/(2*RPM); %chip load

ti_strength=440;%MPa

syms y
circ1=sqrt((1-(y-0.058)^2));
circ2=sqrt((1-(y-0.058)^2))+deltaX;

areal=double(int(circ2-circ1,'y',0,rDOC));% square mm

forcel=ti_strength*areal %Newtons

syms y
area2=(sqrt(1+double(int(circ1,'y',0,rDOC))')+deltaX)*aDOC; % square mm
force2=ti_strength*area2 %Newtons

```

B.4 MATLAB code for power spectrum analysis on tool runout

```

clear all
clc
readlist=[2];
% Plot single-sided amplitude spectrum.

%d=xlsread('tool runout of om2 03_07');
%d=xlsread('new spindle plots');
%d=xlsread('spindle check om2');
%d=xlsread('spindle check om2 04_09');
d=xlsread('runout_tests');

for x=1:length(readlist)
clear temp
col=readlist(x);
n=length(d(:,col));

for i=1:n
if(isnan(d(i,col))==0)
    temp(i)=d(i,col);
end

end
end
x=temp;

% Sampling frequency
Fs=1/0.0002;

% Time vector of 1 second
t = 0:1/Fs:1;

% Create a sine wave of 200 Hz.
%x = sin(2*pi*t*200);

% Use next highest power of 2 greater than or equal to length(x) to
calculate FFT.
nfft= 2^(nextpow2(length(x)));

% Take fft, padding with zeros so that length(fftx) is equal to nfft
fftx = fft(x,nfft);

% Calculate the number of unique points
NumUniquePts = ceil((nfft+1)/2);

% FFT is symmetric, throw away second half
fftx = fftx(1:NumUniquePts);

```

```

% Take the magnitude of fft of x and scale the fft so that it is not a
function of the length of x
mx = abs(fftx);

% Take the square of the magnitude of fft of x.
%mx = mx.^2;

% Since we dropped half the FFT, we multiply mx by 2 to keep the same
energy.
% The DC component and Nyquist component, if it exists, are unique and
should not be multiplied by 2.

if rem(nfft, 2) % odd nfft excludes Nyquist point
    mx(2:end) = mx(2:end)*2;
else
    mx(2:end -1) = mx(2:end -1)*2;
end

% This is an evenly spaced frequency vector with NumUniquePts points.
f = (0:NumUniquePts-1)*Fs/nfft;
hold on
% Generate the plot, title and labels.
plot(f,mx,'g');
title('Frequency Spectrum of tool runout');
xlabel('Frequency (Hz)');
ylabel('Amplitude');

%The power P(f) at frequency f is  $P(f) = A(f)^2$ .

```

APPENDIX C

REPEATABILITY, TOOL WEAR, CONTACT ANGLE, AND HARDNESS

DATA

C.1. Tool material: Aluminum 6061-T6

Table C.1: Tool wear for Al 6061-T6 at 0.5 micron CL and 20K RPM (63.84 m/min)

Chip Load: 0.5 micron/tooth			RPM: 20,000 (63.84 m/min)		Tool: 1.016 mm, 2 flute		
Axial Depth: 0.348mm			Radial Depth: 0.581mm		Coolant: Coolube 2210		
Cutting Tool: tungsten carbide			Tool Number: 2a		Work Material: Al 6061-T6		
test #	Flank Wear (microns)	Nose Wear (microns)	Incremental Time(mins)	Total Time (mins)			
1	0		0	0			
2	2.3		50	50			
3	4.3		50	100			
4	5.9		50	150			
5	6.9		50	200			
6	7.5		50	250			
7	9		50	300			
8	10		50	350			
9	12		100	450			
10	15		100	550			
11	18		100	650			

Table C.2: Tool wear for Al 6061-T6 at 1.0 micron CL and 20k RPM (63.84 m/min)

Chip Load: 1.0 micron/tooth			RPM: 20,000(63.84 m/min)		Tool: 1.016 mm, 2 flute		
Axial Depth: 0.348mm			Radial Depth: 0.581mm		Coolant: Coolube 2210		
Cutting Tool: tungsten carbide			Tool Number: 2b		Work Material: Al 6061-T6		
test #	Flank Wear (microns)	Nose Wear (microns)	Incremental Time(mins)	Total Time (mins)			
(initial)							
1	18		0	650			
2	20		50	700			
3	22		50	750			
4	25.3		50	800			
5	27.1		50	850			
6	28.2		50	900			
7	29		50	950			
8	30		50	1000			
9	33		50	1050			
10	34		50	1100			

Table C.3: Tool wear data for Al 6061-T6 at 0.5 micron CL and 30k RPM (95.76 m/min)

Chip Load: 0.5 micron/tooth			RPM: 30,000 (95.76 m/min)			Tool: 1.016 mm, 2 flute	
Axial Depth: 0.348mm			Radial Depth: 0.581mm			Coolant: Coolube 2210	
Cutting Tool: tungsten carbide			Tool Number: 3a			Work Material: Al 6061-T6	
test #	Flank Wear (microns)	Nose Wear (microns)	Incremental Time(mins)	Total Time (mins)			
(initial)							
1	0		0	0			
2	3.3		100	100			
3	7.5		100	200			
4	9		100	300			
5	13		100	400			
6	16.2		100	500			
7	19		100	600			

Table C.4: Tool wear data for Al 6061-T6 at 1.0 micron CL and 30k RPM (95.76 m/min)

Chip Load: 1.0 micron/tooth			RPM: 30,000			Tool: 1.016 mm, 2 flute	
Axial Depth: 0.348mm			Radial Depth: 0.581mm			Coolant: Coolube 2210	
Cutting Tool: tungsten carbide			Tool Number: 3b			Work Material: Al 6061-T6	
test #	Flank Wear (microns)	Nose Wear (microns)	Incremental Time(mins)	Total Time (mins)			
(initial)							
1	19		0	600			
2	20		50	650			
3	22.5		50	700			
4	24.2		50	750			
5	26		50	800			
6	28		50	850			

C.2. Tool material: CP Titanium

Table C.5: Tool wear data for Ti at 0.3micron CL and 25K RPM(79.80 m/min)

Chip Load: 0.3 micron/tooth			RPM: 25,000 (79.80 m/min)		Tool: 1.016 mm,2 flute		
Axial Depth: 0.348mm			Radial Depth: 0.581mm		Coolant: Coolube 2210		
Cutting Tool:tungsten carbide			Tool Number: 6		Work Material: CP Titanium		
test #	Flank Wear (microns)	Nose Wear (microns)	Incremental Time(mins)	Total Time (mins)			
1	0.00	0.00	0.00	0.00			
2	9.71	161.81	12.50	12.50			
3	17.48	214.63	12.50	25.00			

Table C.6: Tool wear data for Ti at 0.75 micron CL and 25K RPM(79.80 m/min)

Chip Load: 0.75 micron/tooth			RPM: 25,000(79.80 m/min)		Tool: 1.016 mm,2 flute		
Axial Depth: 0.348mm			Radial Depth: 0.581mm		Coolant: Coolube 2210		
Cutting Tool:tungsten carbide			Tool Number: 7		Work Material: CP Titanium		
test #	Flank Wear (microns)	Nose Wear (microns)	Incremental Time(mins)	Total Time (mins)			
1	0.00	0.00	0.00	0.00			
2	6.45	60.15	2.00	2.00			
3	7.74	130.04	2.00	4.00			

Table C.7: Tool wear data for Ti at 1.0 micron CL and 25K RPM(79.80 m/min)

Chip Load: 1.0 micron/tooth			RPM: 25,000(79.80 m/min)		Tool: 1.016 mm,2 flute		
Axial Depth: 0.348mm			Radial Depth: 0.581mm		Coolant: Coolube 2210		
Cutting Tool:tungsten carbide			Tool Number: 8		Work Material: CP Titanium		
test #	Flank Wear (microns)	Nose Wear (microns)	Incremental Time(mins)	Total Time (mins)			
1	0.00	0.00	0.00	0.00			
2	3.57	7.62	1.00	1.00			
3	6.48	11.67	1.00	2.00			
4	7.26	22.69	1.00	3.00			
5	8.75	35.33	2.00	5.00			
6	12.00	38.00	2.00	7.00			

Table C.8: Tool wear data for Ti at 1.25 micron CL and 25K RPM(79.80 m/min)

Chip Load: 1.25 micron/tooth			RPM: 25,000(79.80 m/min)			Tool: 1.016 mm,2 flute	
Axial Depth: 0.348mm			Radial Depth: 0.581mm			Coolant: Coolube 2210	
Cutting Tool:tungsten carbide			Tool Number: 9a			Work Material: CP Titanium	
test #	Flank Wear (microns)	Nose Wear (microns)	Incremental Time(mins)	Total Time (mins)			
1	0.00	0.00	0.00	0.00			
2	3.00	22.00	3.11	3.11			
3	6.10	32.00	2.88	5.99			
4	8.00	33.00	2.41	8.40			
5	11.00	37.00	2.18	10.57			

Table C.9: Tool wear data for Ti at 1.25 micron CL and 35K RPM (111.71 m/min)

Chip Load: 1.25 micron/tooth			RPM: 35,000 (111.71 m/min)			Tool: 1.016 mm,2 flute	
Axial Depth: 0.348mm			Radial Depth: 0.581mm			Coolant: Coolube 2210	
Cutting Tool:tungsten carbide			Tool Number: 9b			Work Material: CP Titanium	
test #	Flank Wear (microns)	Nose Wear (microns)	Incremental Time(mins)	Total Time (mins)			
1	0	0.00	0.00	0			
2	1.5	1.00	3.00	3			
3	3	3.00	2.77	5.77			
4	4	8.00	2.55	8.32			

C.3. Contact angle data

Table C.10: Coolant contact angle- droplet measurements on titanium

Coolube 2210											
volume(μ L)	drop#	diameter(mm)				Avg	stdev	P/V	Angle		
0.1	1	3.491	3.598	3.486	3.480	3.500	3.511	0.049	7.564	1.3484	
0.1	2	3.749	3.626	3.606	3.691	3.660	3.666	0.056	7.899	1.1841	
0.1	3	3.506	3.484	3.382	3.496	3.497	3.473	0.051	7.482	1.3933	
0.1	4	3.460	3.485	3.542	3.531	3.458	3.495	0.039	7.530	1.3668	
0.1	5	3.664	3.651	3.702	3.621	3.640	3.656	0.030	7.876	1.1945	stdev angle
0.1						Avg	3.560		7.670	1.2933	0.1000
Coolube 2300HD											
drop#		diameter				Avg	stdev	P/V	Angle		
0.1	1	1.875	1.833	1.788	1.841	1.837	1.835	0.031	3.953	9.4056	
0.1	2	1.615	1.587	1.591	1.579	1.621	1.599	0.018	3.444	14.1416	
0.1	3	1.663	1.651	1.647	1.660	1.639	1.652	0.010	3.559	12.8377	
0.1	4	1.710	1.715	1.681	1.690	1.676	1.694	0.017	3.650	11.9152	
0.1	5	1.557	1.498	1.524	1.528	1.535	1.528	0.021	3.293	16.1276	stdev angle
0.1						Avg	1.662		3.580	12.6168	2.5071
Coolube 2200											
drop#		diameter				Avg	stdev	P/V	Angle		
0.1	1	2.444	2.313	2.388	2.370	2.385	2.380	0.047	5.128	4.3238	
0.1	2	2.114	2.001	1.983	1.995	2.051	2.029	0.054	4.371	7.2008	
0.1	3	2.056	1.987	1.990	2.101	2.070	2.041	0.050	4.397	6.8489	
0.1	4	1.956	1.858	1.866	1.915	1.910	1.901	0.040	4.096	8.4618	
0.1	5	1.941	1.876	1.880	1.879	1.973	1.910	0.045	4.115	8.3459	stdev angle
0.1						Avg	2.052		4.421	6.7384	1.6708
Koolmist 77											
drop#		diameter				Avg	stdev	P/V	Angle		
0.1	1	1.081	1.101	1.170	1.121	1.115	1.118	0.033	2.408	38.6222	
0.1	2	1.218	1.201	1.205	1.210	1.207	1.208	0.006	2.603	31.4272	
0.1	3	1.300	1.251	1.282	1.271	1.275	1.276	0.018	2.749	27.0478	
0.1	4	1.208	1.209	1.188	1.211	1.200	1.203	0.009	2.592	31.7899	
0.1	5	1.151	1.168	1.159	1.149	1.145	1.154	0.009	2.487	35.5049	stdev angle
0.1						Avg	1.192		2.568	32.5981	4.3925
Koolmist# 78											
drop#		diameter				Avg	stdev	P/V	Angle		
0.1	1	2.110	2.151	2.005	2.109	2.111	2.097	0.055	4.518	6.3154	
0.1	2	2.001	2.008	1.946	1.990	1.986	1.986	0.024	4.279	7.4281	
0.1	3	1.897	1.852	1.846	1.905	1.875	1.875	0.026	4.040	8.8158	
0.1	4	1.945	1.986	1.971	1.912	1.943	1.951	0.028	4.204	7.8303	
0.1	5	2.046	2.089	2.009	1.976	1.943	2.013	0.057	4.336	7.1405	stdev angle
0.1						Avg	1.984		4.275	7.4488	0.9190

Table C.11 Contact angle on aluminum

coolube 2210-Al											
volume(μ L)	drop#	diameter					avg	stdev	p/v	deg	
0.1	1	3.522	3.701	3.710	3.747	3.661	3.668	0.087	7.903	1.1823	
0.1	2	4.070	3.943	4.027	3.921	3.895	3.971	0.074	8.556	0.9317	
0.1	3	3.656	3.830	3.878	3.721	3.770	3.771	0.088	8.124	1.0884	
0.1	4	3.921	3.876	3.880	3.951	3.899	3.905	0.031	8.414	0.9797	
0.1	5	3.701	3.690	3.751	3.732	3.745	3.724	0.027	8.023	1.13	stdev_angle
0.1						Avg	3.808		8.204	1.0569	0.1043
Coolube 2300HD											
	drop#	diameter					avg	stdev	p/v	deg	
0.1	1	1.722	1.553	1.713	1.659	1.681	1.666	0.068	3.588	12.5339	
0.1	2	1.743	1.591	1.702	1.661	1.652	1.670	0.057	3.597	12.4415	
0.1	3	1.428	1.431	1.550	1.381	1.396	1.437	0.067	3.096	19.2942	
0.1	4	1.543	1.500	1.498	1.527	1.538	1.521	0.021	3.277	16.3587	
0.1	5	1.660	1.670	1.689	1.664	1.673	1.671	0.011	3.600	12.4109	stdev_angle
0.1						Avg	1.593		3.432	14.2874	3.1164
Coolube 2200											
	drop#	diameter					avg	stdev	p/v	deg	
0.1	1	2.276	2.000	2.176	2.201	2.070	2.145	0.109	4.620	5.9078	
0.1	2	2.100	2.251	2.155	2.213	2.109	2.166	0.065	4.666	5.7354	
0.1	3	2.347	2.354	2.295	2.310	2.289	2.319	0.030	4.996	4.6749	
0.1	4	1.892	1.987	2.002	2.101	2.078	2.012	0.083	4.335	7.1454	
0.1	5	1.990	2.042	2.111	2.071	1.891	2.021	0.085	4.354	7.0528	stdev_angle
0.1						Avg	2.132		4.594	6.0083	1.0249
Koolmist 78											
	drop#	diameter					avg	stdev	p/v	deg	
0.1	1	1.661	1.570	1.631	1.648	1.598	1.622	0.037	3.494	13.5545	
0.1	2	1.677	1.740	1.706	1.689	1.688	1.700	0.025	3.663	11.7906	
0.1	3	1.612	1.670	1.648	1.658	1.637	1.645	0.022	3.544	12.9987	
0.1	4	1.687	1.593	1.590	1.608	1.651	1.626	0.042	3.503	13.4522	
0.1	5	1.650	1.680	1.718	1.682	1.664	1.679	0.025	3.617	12.2394	stdev_angle
0.1						Avg	1.654		3.564	12.7847	0.7693
Koolmist# 77											
	drop#	diameter					avg	stdev	p/v	deg	
0.1	1	0.976	0.884	1.056	1.098	1.106	1.024	0.094	2.206	47.981	
0.1	2	1.382	1.251	1.226	1.156	1.248	1.253	0.082	2.699	28.4604	
0.1	3	1.372	1.233	1.268	1.364	1.516	1.351	0.110	2.910	23.0441	
0.1	4	1.452	1.231	1.426	1.431	1.376	1.383	0.090	2.980	21.5336	
0.1	5	1.327	1.191	1.284	1.264	1.189	1.251	0.060	2.695	28.5772	stdev_angle
0.1						Avg	1.252		2.698	28.4896	10.5800

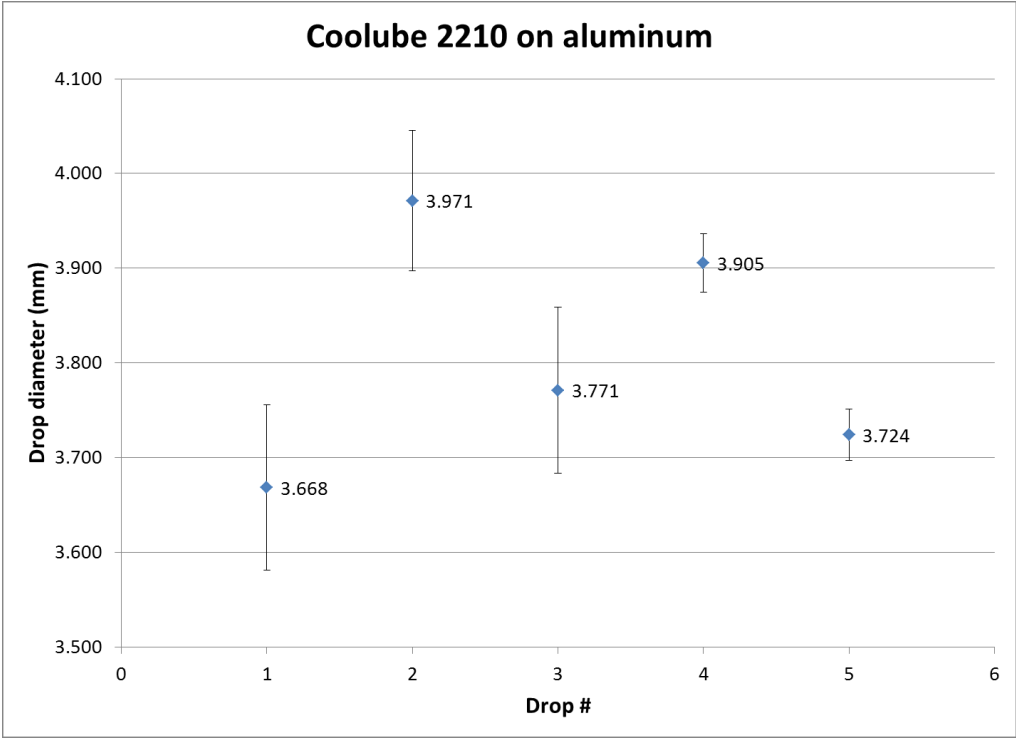


Figure C.1: Average and deviation droplet size of 0.1 microliter

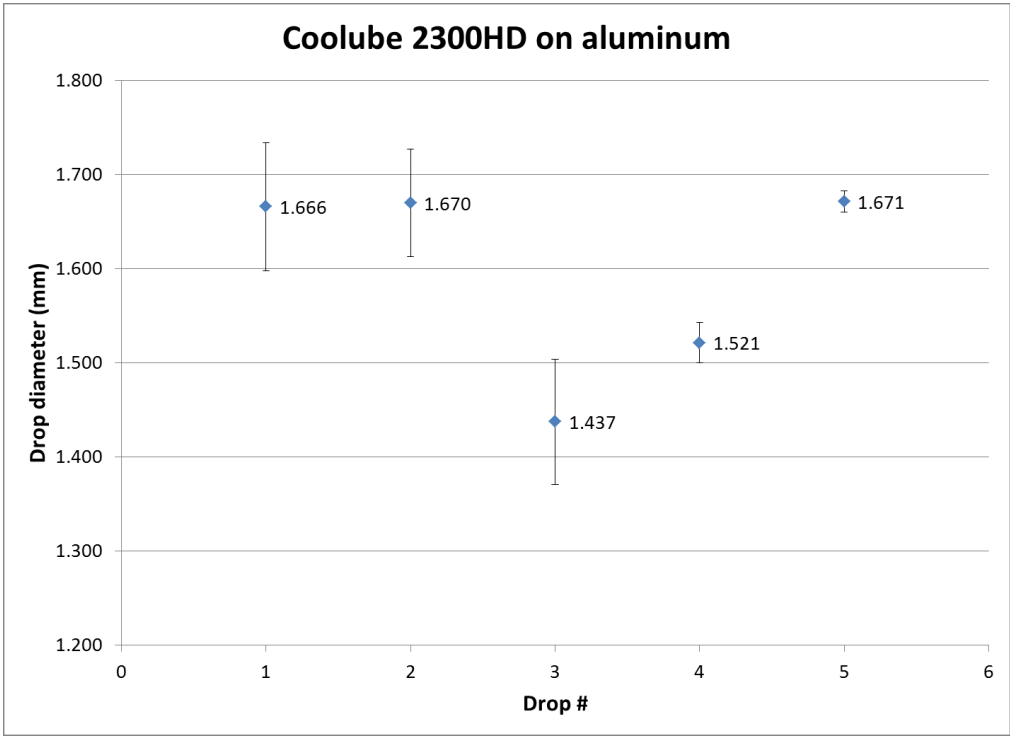


Figure C.2: Average and deviation droplet size of 0.1 microliter

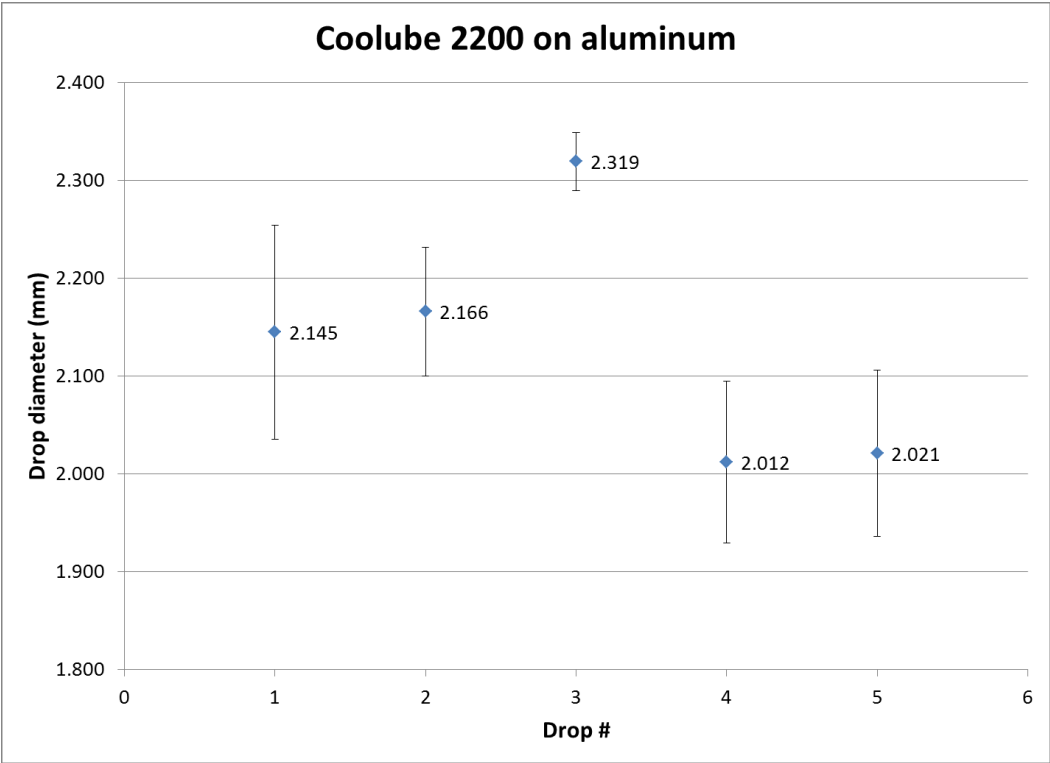


Figure C.3: Average and deviation droplet size of 0.1 microliter

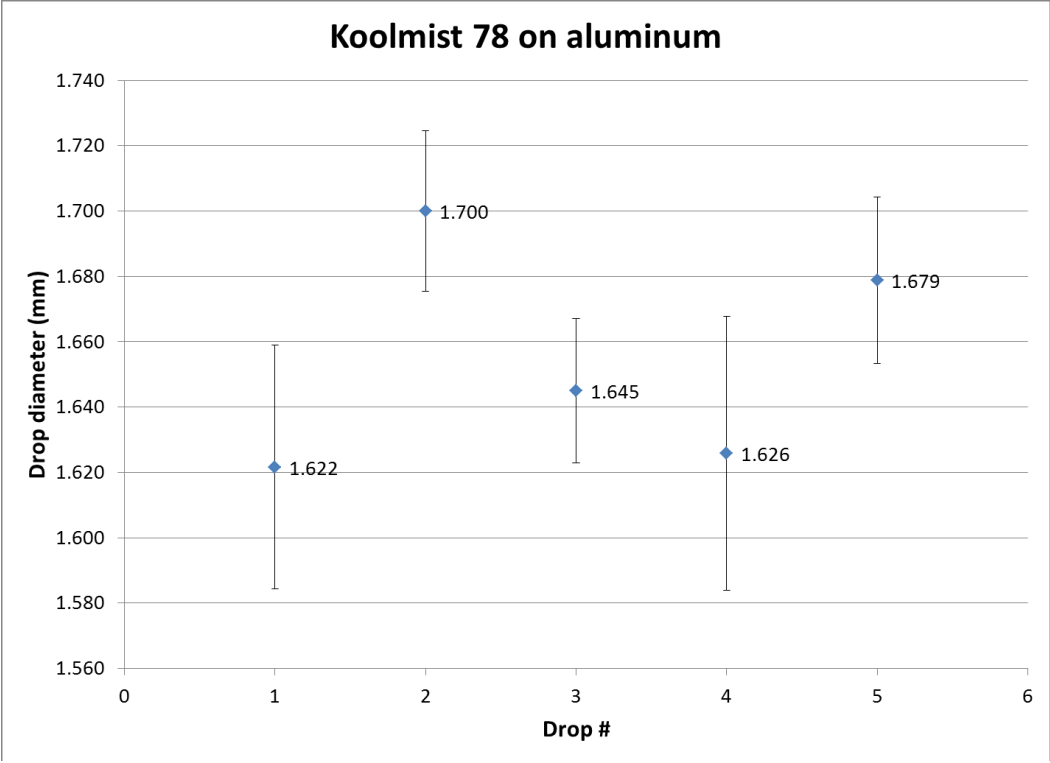


Figure C.4: Average and deviation droplet size of 0.1 microliter

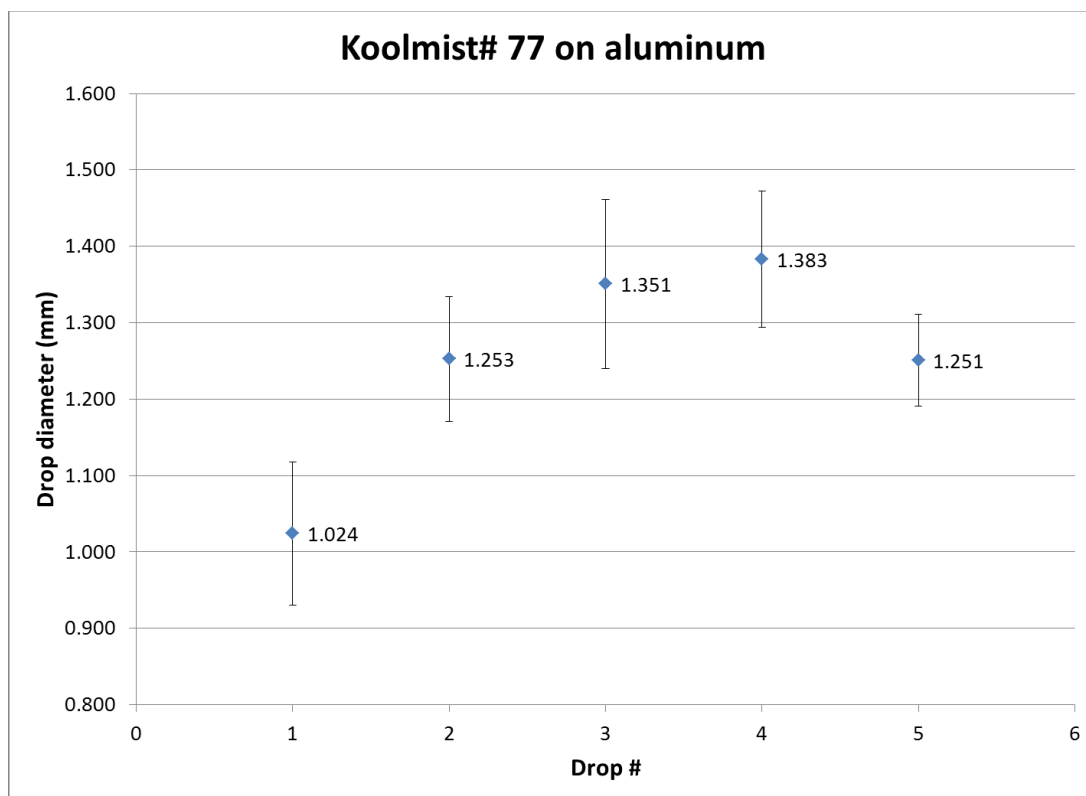


Figure C.5: Average and deviation droplet size of 0.1 microliter

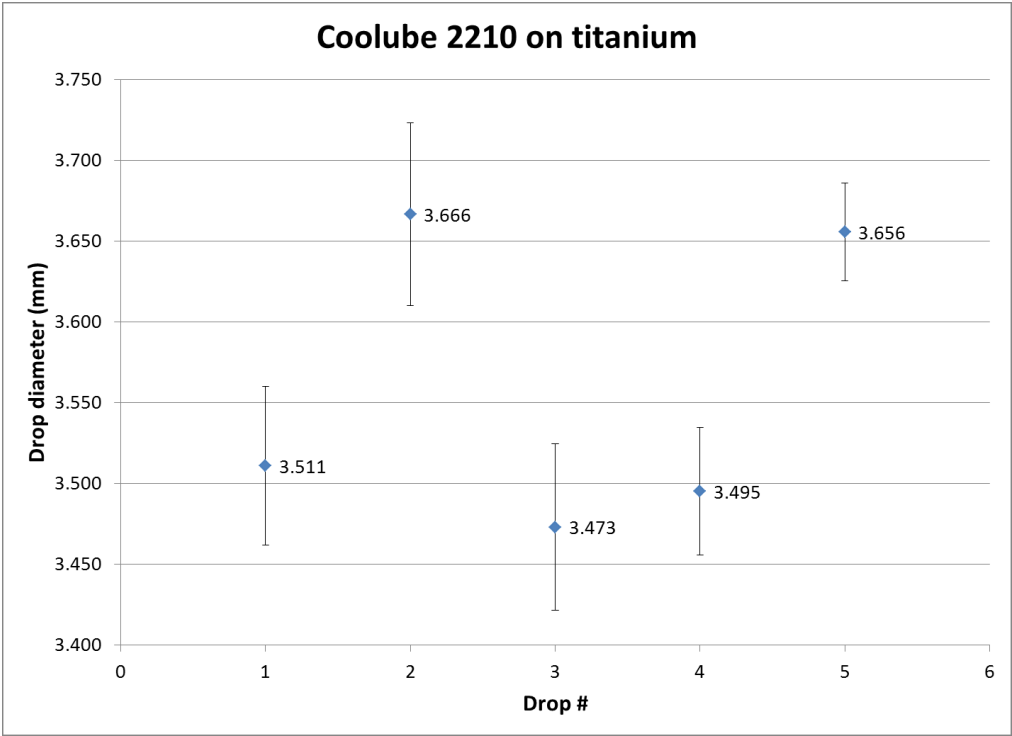


Figure C.6: Average and deviation droplet size of 0.1 microliter

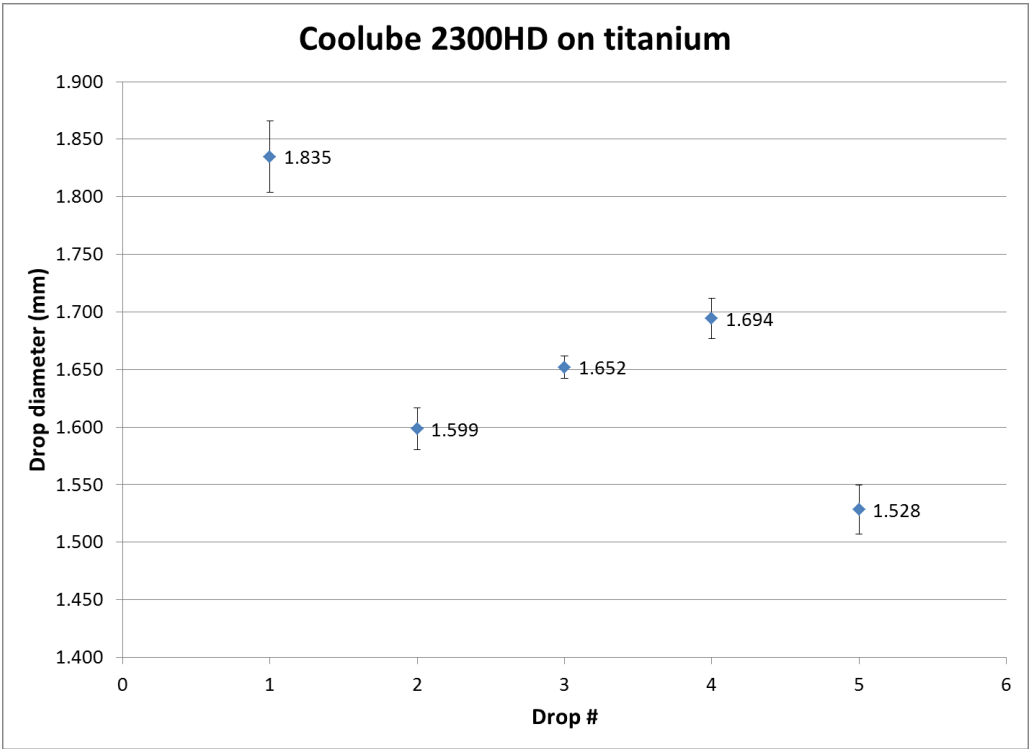


Figure C.7: Average and deviation droplet size of 0.1 microliter

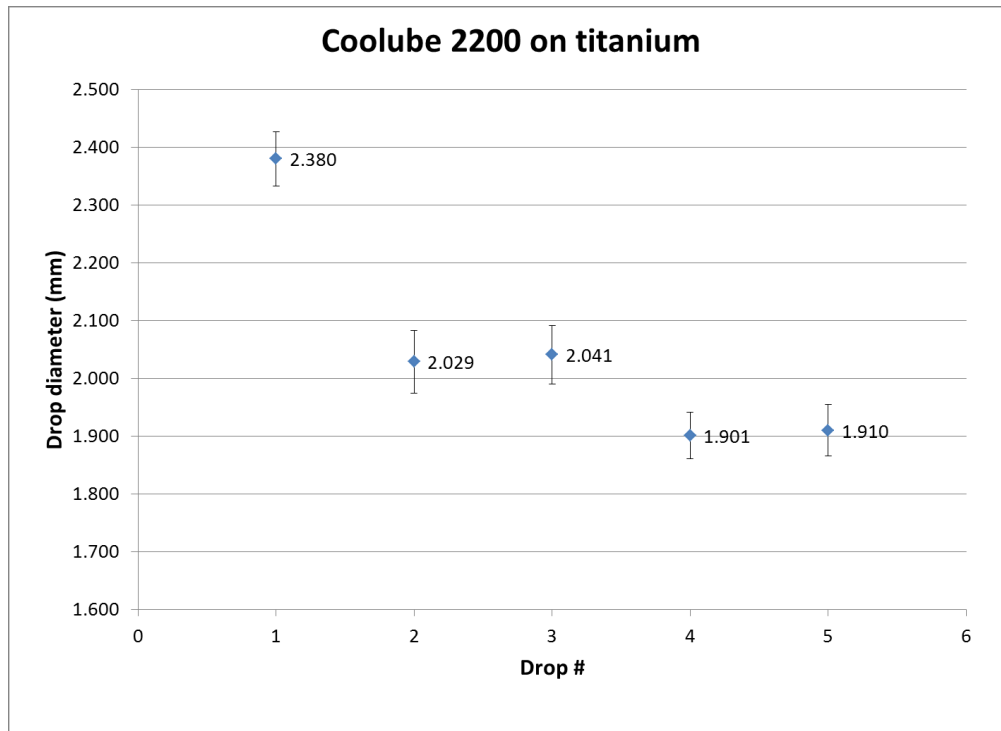


Figure C.8: Average and deviation droplet size of 0.1 microliter

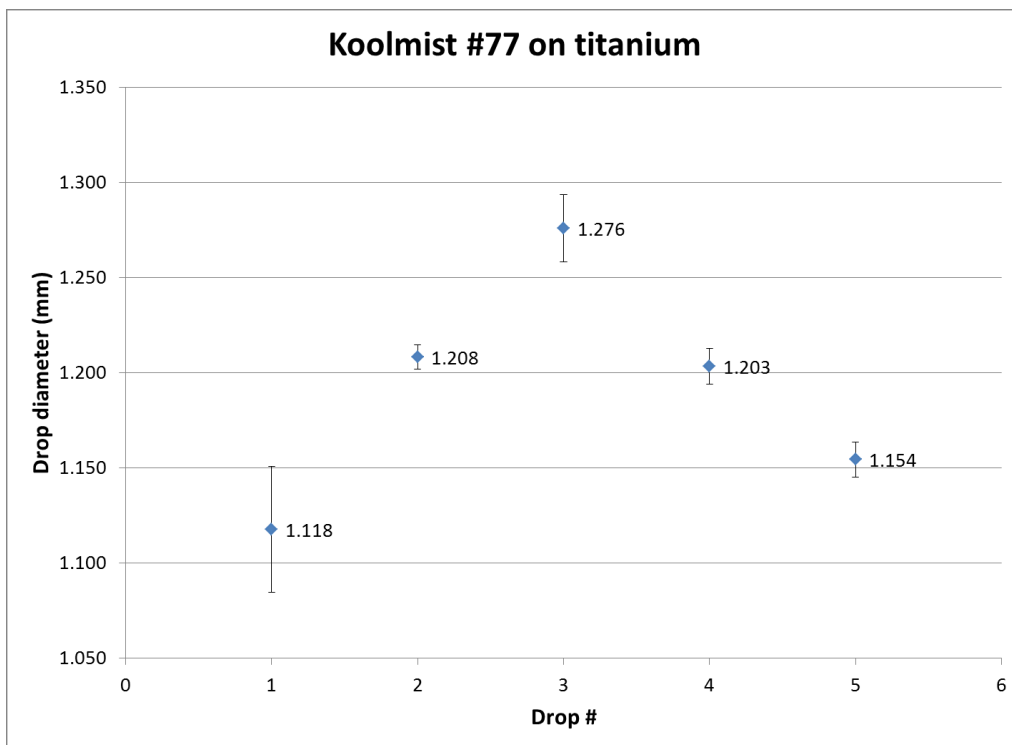


Figure C.9: Average and deviation droplet size of 0.1 microliter

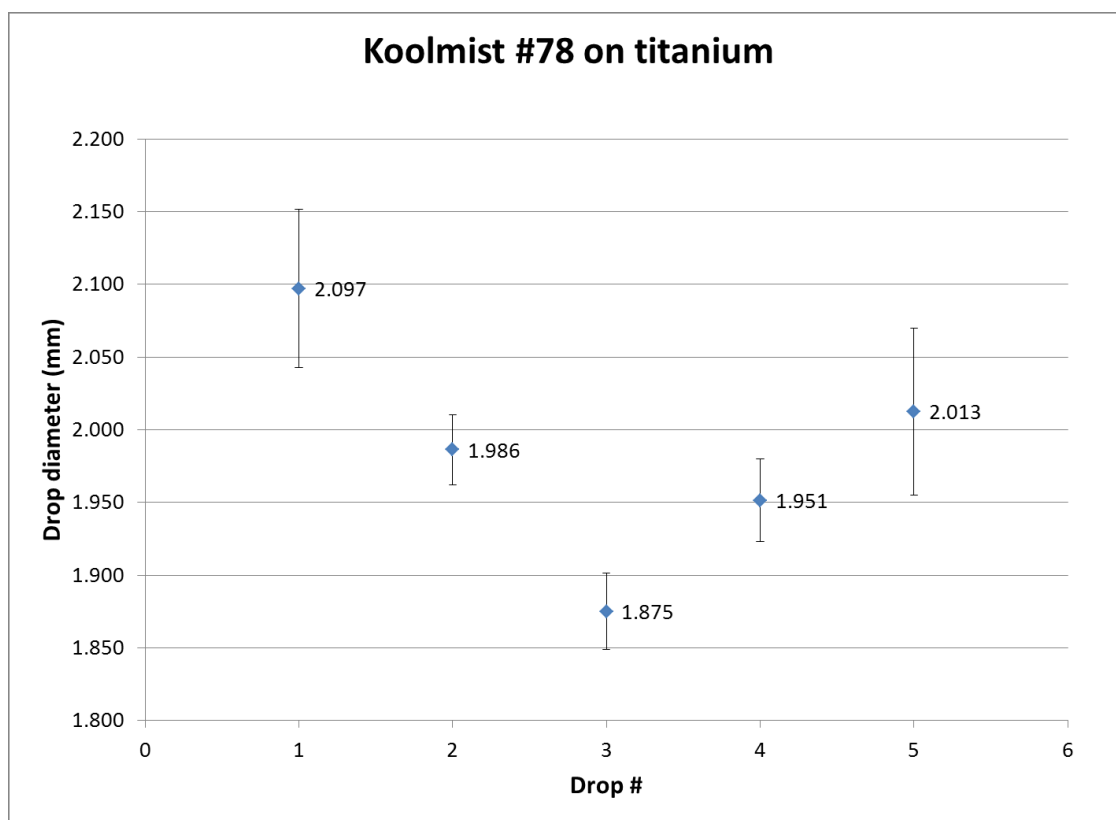


Figure C.10: Average and deviation droplet size of 0.1 microliter

Table C.12: Vickers hardness at 0.75 micron CL on titanium with 0.1 N force for 13 sec

0.75 μm chip load, 0.381 axial depth, 0.558 radial depth		
diagonal (mm)	vickers hardness	surface depth(mm)
0.02606	271.7	0.0173
0.02638	265.1	0.0725
0.02667	259.5	0.0470
0.02686	255.8	0.0774
0.02686	255.8	0.1136
0.02785	238.0	0.2059
0.02812	233.3	0.2460
0.02806	234.3	0.2882
0.02756	243.0	0.2516
0.02694	254.3	0.1858
0.02674	258.1	0.1302
0.02687	255.5	0.0635
0.02662	260.4	0.0140
0.02898	219.8	2.8102
0.02906	218.5	1.8157

Table C.13: Vickers hardness at 0.3 micron CL on titanium with 0.1 N force for 13 sec

0.3 μm chip load, 0.381 axial depth, 0.558 radial depth		
diagonal (mm)	vickers hardness	surface depth(mm)
0.02705	252.3	0.0233
0.02776	239.5	0.0532
0.02734	247.0	0.0930
0.02819	232.3	0.1314
0.02795	236.2	0.1812
0.02829	230.7	0.1854
0.02760	242.2	0.1468
0.02801	235.2	0.1057
0.02795	236.2	0.0610
0.02711	251.2	0.0250
0.02917	216.9	1.0184
0.02916	217.0	1.6621

Table C.14: Vickers hardness at 1.0 micron CL on titanium with 0.1 N force for 13 sec

1.0 μm chip load, 0.381 axial depth, 0.558 radial depth		
diagonal (mm)	vickers hardness	surface depth(mm)
0.02825	231.2	0.0433
0.04117	217.8	0.0832
0.02857	226.1	0.1999
0.02846	227.8	0.2520
0.02879	222.6	0.3008
0.02927	215.4	0.2598
0.02931	214.9	0.2147
0.02866	224.7	0.1777
0.02918	216.8	0.1361
0.02845	228.0	0.0711
0.02848	227.6	0.0417
0.02917	216.9	2.1466
0.02928	215.2	2.1417

Table C.15: machine repeatability test of toughing plug gage to rubber washer

coordindinate zeroing	
	x machine coordinate(mm)
	-9.4425
	-9.4436
	-9.4432
	-9.4422
	-9.443
	-9.4428
	-9.4431
	-9.4428
	-9.442
	-9.4422
average	-9.44274
repeatability	0.000510338

APPENDIX D**G-CODE CNC PROGRAM FOR MILLING EXPERIMENT**

D.1 NC code for CNC OM2

The Code file below was used specifically for tool 9 at 1.25 micron CL and 25000 RPM. This was based off of a generic code where the RPM, feedrate, and number of passes are variable. So this code is easily adapted to other settings and parameters for milling.

```
%
O00111
(DOM 9)
(created 1/30/11)
(ASSUMING 9.72 mm WIDE PART 25000RPM 62.5mm/min at 1.25CL)
N35 G00 G17 G40 G90 G21
(STANDARD START-UP SETTINGS)
N45 T1
(IDENTIFIES TOOLING)
N50 G54 G00 X0. Y0. Z25.4 A0. B0.
(MOVES MACHINE TO STARTING COORDINATES)
(COORDINATES SET IN LINE G54 IN OFFSETS)
(MUST SET ZEROES ON UPPER LEFT CORNER OF PART)
N55 G43 H01
(CALLS OUT TOOL LENGTH COMPENSATION)
N60 S25000 M03
(SETS SPINDLE SPEED AND TURNS ON CLOCK-WISE)
N65 G01 X-1.27 Y0.635 Z6.35 F508.
(MOVES TOOL TO XYZ AT 20.0 INCH/MINUTE)
```


N70 M97 P77777 L20

(M97 CALLS FOR SUB-ROUTINE)

(P77777 --> SUBROUTINE AT LINE N55555)

(L5 --> NUMBER OF TIMES TO REPEAT SUBROUTINE)

N75 G90 G01 G54 X0. Y0. Z25.4 F508.

(RETURNS TOOL TO START POSITION)

N80 M30

(ENDS PROGRAM)

(SUBROUTINE)

N77777 G90 G01 Z-0.381 F254.

(LOWERS TOOL TO Z AT MM/MINUTE)

N77782 G91 X12. F62.5

(MOVES INCREMENTAL DISTANCE IN X DIRECTION)

(NOT DEPENDENT UPON COORDINATES)

N77787 G90 Z6.35 F254.

(RETURNS TOOL TO Z BASED ON COORDINATES)

N77792 G91 X-12. Y-0.558 F508.

(MOVES INCREMENTAL DISTANCE IN X Y DIRECTION)

(NOT DEPENDENT UPON COORDINATES)

(x number should be negative of line N77782)

N77797 M99

(RETURNS TO MAIN PROGRAM)

%

APPENDIX E
FEA VERIFICATION CALCULATIONS

E.1 Hand Calculation Verifications for FEA

The end milling tool was modeled as cantilever beam subjected to cutting force F and fixed on the left side as shown in Figure E.1. The force used was 50N and a length of 2.083 mm, which was the length of the endmill before the taper. This is where the tool is most prone to fracture. The purpose of these calculations was to verify that hand calculations could be close the FEA values, so the 50N force was arbitrarily chosen.

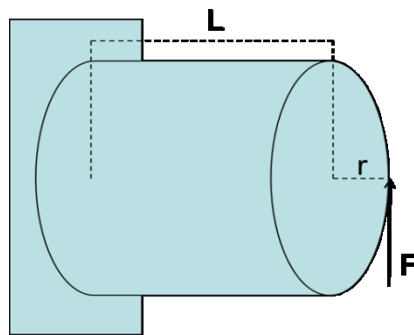


Figure E.1: Force imposed on model with bending component and torsion component

This cutting force results in a resultant stress which is separated into three types of stresses: bending, torsion, and shear. Also, to make the overall calculations more accurate we use SolidWorks to calculate the cross sectional properties of the actual cutting tool. This is shown in Figure E.2

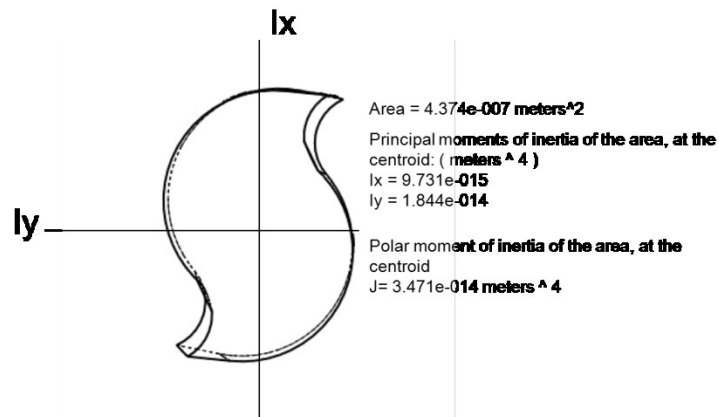


Figure E.2: Cross section of microtool in SolidWorks is shown, this calculates more accurate values of moments of inertia. Coordinate axis are with reference to SolidWorks model. I_y is used in calculation due to rotation from bending about the respective axis.

E.1.1 Bending Stress

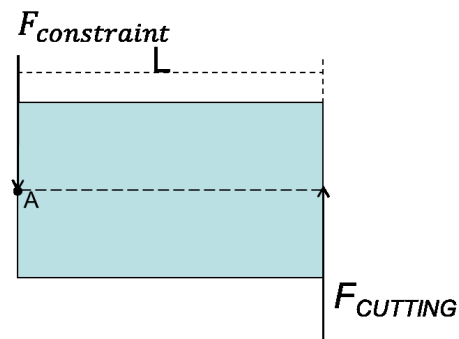


Figure E.3: Bending stress

To find the max bending stress on the beam, the bending moment M_A at the fixed location must first be calculated. We multiply the cutting force and the beam length

$$M_A = F_{cutting} * L \quad (E1)$$

$$F_{cutting} = 50N \quad (E2)$$

$$L = 0.00208m \quad (E3)$$

$$M_A = 50 * .00208 = 0.104 Nm \quad (E4)$$

Finally, the bending stress at the diameter of the tool is computed by the following equation

$$\sigma_{bending} = \frac{M_A c}{I_y} \quad (E5)$$

$$\sigma_{bending} = \frac{0.104 Nm * 0.000508 m}{1.844 * 10^{-14} m^4} \quad (E6)$$

Here, M_A is the bending moment, c is the radius of the tool, and I_y is the moment of inertia that was solved for using SolidWorks.

$$\sigma_{bending} = 2.865 GPa \quad (E7)$$

E.1.2 Torsion

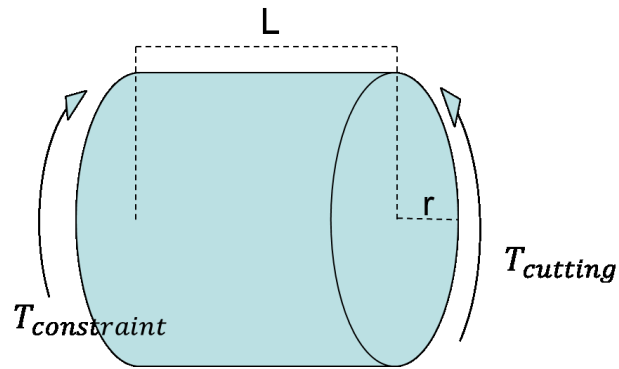


Figure E.4: Torsion

In order to calculate stress created from torsion the torque on the beam from the cutting force must be calculated. Equation (E8) shows the calculation of the torque on the outside of the circular beam.

$$T_{cutting} = F_{cutting} * r \quad (E8)$$

$$\begin{aligned} T_{cutting} &= 50 \text{ N} * 0.000508 \text{ m} \\ &= 0.0254 \text{ Nm} \end{aligned} \quad (E9)$$

Now, using the SolidWorks calculation of the polar moment J and the radius r , the stress can be found in equation (E10).

$$\tau_{torsion} = \frac{T_{cutting} r}{J} \quad (E10)$$

$$\tau_{torsion} = \frac{0.0254 \text{ Nm} * 0.000508 \text{ m}}{3.471 * 10^{-14} \text{ m}^4} = 0.372 \text{ GPa} \quad (E11)$$

E 1.3 Shear Stress

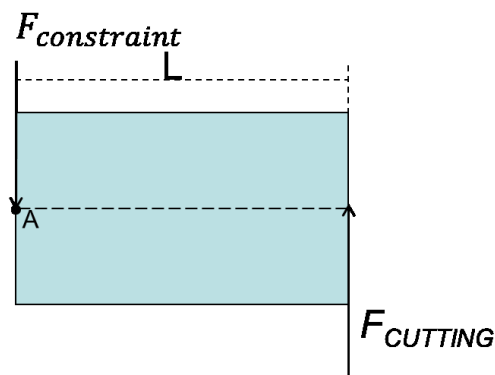


Figure E.5: Shear Stress

Equation (E12) shows the shear stress that is at the constrained end of the part which is in reaction to the cutting force at the end of the shaft. The area is the calculation from SolidWorks.

$$\tau_{shear} = \frac{F_{cutting}}{A} \quad (E12)$$

$$\tau_{shear} = \frac{50 \text{ N}}{4.374 * 10^{-7} \text{ m}^2} = 0.114 \text{ GPa} \quad (E13)$$

E.2 Comparison and error of FEA

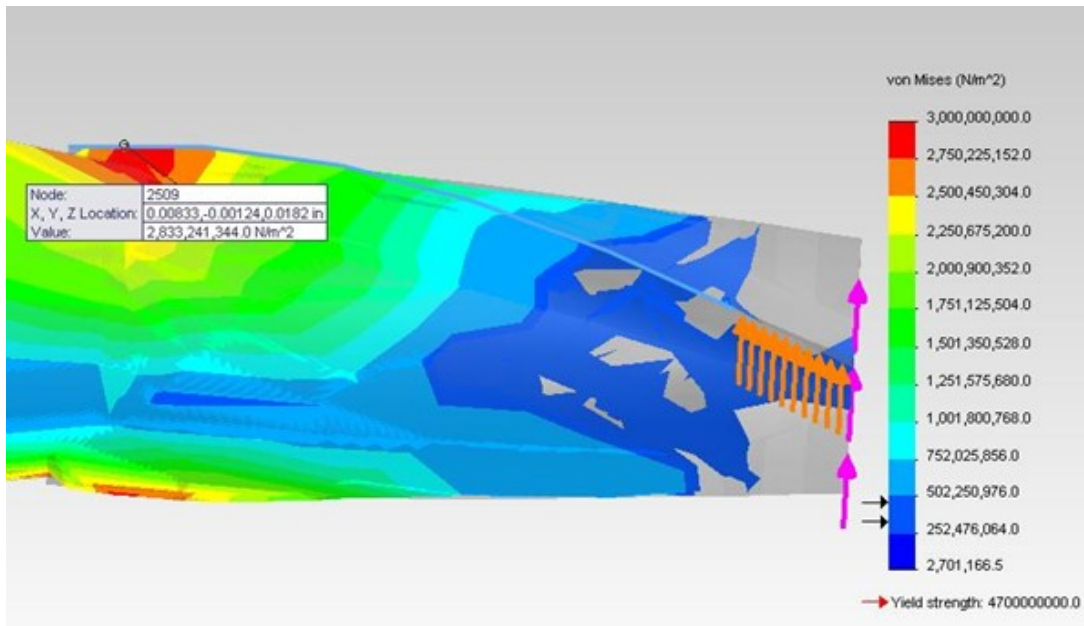


Figure E.6: wireframe FEA model of stress concentration on endmill showing a stress at the tool diameter of 2.833 GPa

Once the bending, torsion, and shear calculations were found, they were compared to the SolidWorks model. The FEA found that a max stress of 2.833 GPa was found at the tool diameter under the 50N of force. The hand calculations then needed to be converted into von Mises equivalent stress. So with equation (E14) the bending (σ_x or $\sigma_{bending}$), torsion (τ_{xy} or $\tau_{torsion}$), and shear (τ_{zx} or τ_{shear}) stresses were converted to von Mises equivalent stress. Multiple stresses seen in (E14) were eliminated because there wasn't a stress present in that direction.

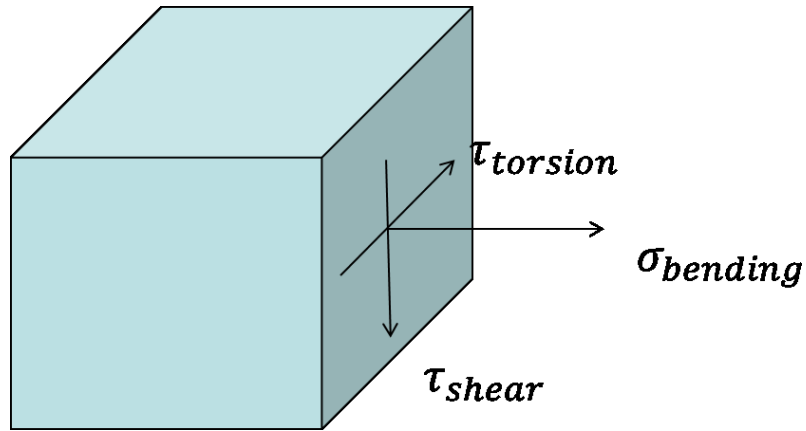


Figure E.7: Torsion, shear, and bending stresses on beam element resulting from cutting force

$$\sigma_{vM} = \frac{1}{\sqrt{2}} \sqrt{(\sigma_x - \sigma_y)^2 + (\sigma_y - \sigma_z)^2 + (\sigma_z - \sigma_x)^2 + 6\tau_{xy}^2 + 6\tau_{yz}^2 + 6\tau_{zx}^2} \quad (E14)$$

$$\sigma_{vM} = \frac{1}{\sqrt{2}} \sqrt{(\sigma_{bending})^2 + (\sigma_{bending})^2 + 6\tau_{shear}^2 + 6\tau_{torsion}^2} \quad (E15)$$

$$\sigma_{vM} = \frac{1}{\sqrt{2}} \sqrt{2(\sigma_{bending})^2 + 6\tau_{shear}^2 + 6\tau_{torsion}^2} \quad (E16)$$

$$\sigma_{vM} = \frac{1}{\sqrt{2}} \sqrt{2(2.865)^2 + 6 * 0.372^2 + 6 * 0.114^2} = 2.943 \text{ GPa} \quad (E17)$$

After the equivalent von Mises stress was found, a total error was calculated

$$\text{Error}\% = \frac{\sigma - \sigma_{vM}}{\sigma} = \frac{2.833 - 2.943}{2.833} = 3.88\% \text{ error} \quad (E18)$$

APPENDIX F

TOOL MODEL DERIVATIONS

F.1 Simplified Taylor equation derivation

Starting with Taylor full equation,

$$VT^n f^c d^g = h \quad (\text{F1})$$

Where V is cutting speed, T is tool life, f is feed rate, and d is depth of cut. n , c , g , and h are constants. Since V and d are held constant in the experiments, they are combined with the constant h leaving,

$$T^n f^c = \left(\frac{h}{Vd^g}\right) \quad (\text{F2})$$

Now the right side of the equations holds all constants, so they can be combined into a new constant h' .

$$T^n f^c = h' \quad (\text{F3})$$

Then the entire equation is raised to the $\frac{1}{c}$

$$T^{n/c} f^1 = h'^{1/c} \quad (\text{F4})$$

This can be simplified with new constants,

$$T^m f = k \quad (\text{F5})$$

F.2 Tool model derivation

Since the $\frac{\Delta t_i}{T_i}$ is the partial tool life at a certain feedrate, then the total partial tool life due to both feedrates can be summed. The subscripts used (1 and 2) refer to the parameter set during the experiment.

$$\frac{\Delta t_1}{T_1} + \frac{\Delta t_2}{T_2} = Q \quad (\text{F6})$$

Then the Taylor equation (F5) becomes

$$f_1 T_1^m = k \quad (\text{F7})$$

$$T_1 = \left(\frac{k}{f_1}\right)^{1/m} \quad (\text{F8})$$

$$\frac{1}{T_1} = \left(\frac{f_1}{k}\right)^{1/m} \quad (\text{F9})$$

Then this final algebraic equivalent can be substituted back into equation (F6)

$$\Delta t_1 \left(\frac{f_1}{k}\right)^{1/m} + \Delta t_2 \left(\frac{f_2}{k}\right)^{1/m} = Q \quad (\text{F10})$$

$$\Delta t_1 f_1^{1/m} + \Delta t_2 f_2^{1/m} = Q k^{1/m} \quad (\text{F11})$$

Now solving for k ,

$$\frac{1}{Q}(\Delta t_1 f_1^{1/m} + \Delta t_2 f_2^{1/m}) = k^{1/m} = T_e f_e^{1/m} \quad (\text{F12})$$

T_e is the equivalent tool life and f_e is equivalent federate. By taking the two right-hand terms and raising them to the power of m , it can be shown that the equivalent time/feedrate equation is representative of the simplified Taylor equation.

$$(k^{1/m} = T_e f_e^{1/m})^m \quad (\text{F13})$$

$$f_e T_e^m = k \quad (\text{F14})$$

So by now going back to equation (F12) and solving for f_e , the equivalent feedrate can be found.

$$f_e^{1/m} = \frac{1}{Q T_e} (\Delta t_1 f_1^{1/m} + \Delta t_2 f_2^{1/m}) \quad (\text{F15})$$

VITA

Name: Dominic Shiosaki

Address: C/O Department of Mechanical Engineering,
3123 Texas A&M University
College Station, TX 77843.

Email Address: dshiosak@gmail.com

Education: B.S. Mechanical Engineering, University of California, San Diego, 2009
M.S. Mechanical Engineering, Texas A&M University, 2011